Optimization of ITO TCO for thin-film silicon and HIT solar cells

Benjamin F.A. Bolman

TU Delft
Delft University of Technology
Challenge the future

Optimization of ITO TCO for thin-film silicon and HIT solar cells

MSc. Thesis

by

Benjamin F.A. Bolman
Born on the 12th of February 1982 in Harlingen

Supervisors

prof. dr. M. Zeman

O. Isabella, MSc.

Photovoltaic Materials and Devices

Delft University of Technology

October 17, 2010

Preface

Ten years ago I started studying economics in Amsterdam and now, after starting 3 studies, sailing more than 25,000 nautical miles and hopefully a bit wiser, this thesis concludes the Sustainable Energy Technology master at Delft University of Technology. For the past 10 months this MSc. project was carried out in the Photovoltaic Material and Devices (PVMD) group, part of the Electrical Sustainable Energy department at the faculty of Electrical Engineering, Mathematics and Computer Sciences. The aim of the project is the optimization of a deposition process by varying the process parameters. A quantitative method is used to evaluate optical and electrical data. The background of this project is thin-film silicon and HIT solar cell research, therefore only materials used in these solar cells are characterized.

The thesis comprises 9 chapters. In the first chapter an introduction into the project is given. A methodical introduction into the theoretical background of the different types of thin-film solar cells, transparent conductive oxides and deposition methods is given in chapter 2. The measurement equipment used for characterization is described in chapter 3. In the next chapter, chapter 4, the results of the different series of depositions are described in detail, followed by three chapters describing the application of optimized ITO TCOs in the different types of thin-film solar cells made within the PVMD group. Conclusions (chapter 8) and recommendations (chapter 9) round off the thesis.

When I was given the opportunity to perform the master graduation project within the PVMD group I could not have thought that time would pass so quickly. It was a very interesting experience and I would like to thank prof. dr. Miro Zeman very much for giving me the opportunity to be part of his team. I also like to thank dr. R.A.C.M.M. van Swaaij and dr. ir. R. van de Krol for being part of my graduation committee.

From the moment I started Olindo Isabella, MSc. has been my daily supervisor. Olindo assisted me in virtually everything, ranging from the first introduction to the deposition and measurement equipment up to reviewing this thesis, for which I'm very grateful. I have great respect for his dedication and the way he pursues his PhD. I wish him all the best for the remaining part of his PhD.

A large portion of the work in this thesis could not have been done

without the support of the members of the PVMD group. Special thanks goes out to Joke Westra, MSc., Dong Zhang, MSc., dr. Sergiy Dobrovolsky, dr. Tristan Temple, Solomon Agbo, MSc. and Klaus Jaeger, MSc. for all their support, ranging from the deposition of solar cells with ITO TCO to helping me with XRD data analysis. Martijn Tijsen and Stefaan Heirman, the technical staff of the PVMD group, are greatly appreciated for keeping the deposition equipment up and running and for helping me with etching ITO.

I like to thank all my roommates, Chare, Gerald, Ashkan, Helen and Marinda for the much-needed distraction. Special thanks goes out to Jeroen Sap, MSc. for being a great roommate as well and providing his Scout model which saved me at least 2 weeks of Dektak measurements.

There's a number of persons who could possibly be even happier with my graduation than I am. First of all my parents, it must be hard to have not 1 or 2 but 3 non-nominal studying children. I'm very grateful for their unconditional support all along the road. And finally, Christa. Six years ago I was about to graduate, now I really am (almost) finished!

Benjamin Bolman,
October 2010

Abstract

Alternative energy source are needed to satisfy the world's immense annual energy demand and, at the same time, reduce the vast amounts of greenhouse gasses being emitted into the atmosphere. Apart from resources such as wind, biomass, hydropower and geothermal, solar energy is a promising alternative considering the absence of moving parts and the emission free electricity production. Although photovoltaic systems are now widely available, the price of electricity generated with these systems is still not competitive with electricity from fossil fuels. Therefore a lot of research is aimed at minimizing both material use and production costs of solar cells, resulting in the development of thin-film solar cells. The PhotoVoltaic Materials and Devices group at Delft University of Technology concentrates on thin-film silicon and HIT solar cells in particular.

Within thin-film silicon solar cells, the so-called Transparent Conductive Oxide (TCO) plays an important role. The optimization of TCOs is a very meticulous process since these thin layers not only need to be both highly transparent and conductive, but are also used for light management; that is manipulating the path of the light through the active layer by means of a textured TCO surface which scatters the light. Besides, the TCOs are also used as back reflector in combination with metallic films. By using these methods both the short circuit current and the overall conversion efficiency of the thin-film silicon solar cells is improved.

This report focuses on the actual optimization of the RF magnetron sputtering deposition process of tin-doped indium (ITO) TCOs for application in thin-film silicon and HIT solar cells. By varying deposition parameters such as power, pressure and temperature an optimal recipe for each specific type of thin-film solar cell could be established. The optimized ITO TCO recipes are utilized as both front and back TCO in a-Si:H, μc-Si:H and HIT thin-film solar cells. Thanks to these optimizations we were able to achieve efficiencies which were comparable, and in some cases even better, to similar devices made with the already optimized aluminum-doped zinc oxide (AZO) TCOs. A highest initial efficiency of 10.7% was achieved for a $p-i-n$ solar cell with front Asahi U-type TCO and back ITO TCO.

Besides the actual optimization process the consistency and repeatability of the ITO depositions with time was investigated. Since the optimization

process is so elaborate, repeatability of depositions is very important. Regularly scheduled depositions were made to check the variations of thin-film quality with time. The results show that the quality of the ITO thin-films is quite variable. The ITO quality is known to drop significantly after a deposition chamber ventilation. The number of hours of sputtering needed to return to original and acceptable quality was investigated by means of a post-ventilation recovery series.

Contents

Preface i

Abstract iii

1 Introduction 1
1.1 Background and motivation . . . 1
1.2 Solar cells . . . 2
1.3 Thin-film silicon solar cells . . . 3
1.3.1 Amorphous silicon solar cells . . . 4
1.3.2 Microcrystalline silicon solar cells . . . 6
1.3.3 Tandem solar cells . . . 7
1.3.4 HIT solar cells . . . 7
1.3.5 Air Mass and spectral range . . . 8
1.4 Outline of the thesis . . . 8

2 Theoretical background 10
2.1 Transparent Coductive Oxides . . . 10
2.2 Tin-doped indium oxide (ITO) . . . 12
2.2.1 Physical structure . . . 12
2.2.2 Electrical properties . . . 13
2.2.3 Optical properties . . . 16
2.2.4 Availability . . . 19
2.3 Deposition techniques . . . 19
2.3.1 Thermal evaporation . . . 20
2.3.2 Chemical vapor deposition . . . 20
2.3.3 Spray pyrolysis . . . 21
2.3.4 Screen printing technology . . . 21
2.3.5 Sputtering . . . 21

3 Deposition and measurement equipment 33
3.1 RF magnetron sputtering system . . . 33
3.1.1 General layout of the deposition system . . . 33
3.1.2 Deposition sequence . . . 34
3.2 Material characterization . . . 36

3.2.1 Hall effect measurement 36
3.2.2 Four point probe 37
3.2.3 MiniRT setup 38
3.2.4 Dektak surface profiler 38
3.2.5 XRD 39
3.3 Optical and morphological characterization 39
3.3.1 Spectrophotometer 39
3.3.2 Scanning Electron Microscopy (SEM) 42
3.3.3 Atomic Force Microscopy (AFM) 42
3.4 Figure of Merit 43
3.5 Solar cell characterization 45

4 RF magnetron sputtered ITO 47
4.1 Introduction 47
4.2 Experimental 47
4.3 Results and discussion 48
4.3.1 Temperature series 48
4.3.2 Power series 51
4.3.3 Pressure series 54
4.3.4 Oxygen partial pressure series 57
4.3.5 Target-to-substrate series 59
4.3.6 Deposition time series 62
4.3.7 Standard recipe 67
4.3.8 Repeatability and recovery series 67
4.3.9 Effect of annealing 73
4.3.10 Effect of etching 75
4.3.11 Tilted angle sputtering 78
4.4 Conclusions 81

5 a-Si:H optimization 83
5.1 Introduction 83
5.2 Experimental 83
5.2.1 p-i-n devices 83
5.2.2 n-i-p devices 87
5.3 Conclusions 88

6 ucSi:H optimization 90
6.1 Introduction 90
6.2 Experimental 90
6.3 Results and discussion 90
6.4 Conclusions 91

7 HIT optimization **92**
7.1 Introduction . . . 92
7.2 Experimental . . . 92
7.3 Results and discussion . . . 93
7.4 Conclusions . . . 94

8 Conclusions **95**

9 Recommendations **96**

A Deposition parameters **97**

B ITO standard recipe **100**

Bibliography **111**

List of figures **113**

List of tables **114**

Nomenclature **115**

Chapter 1

Introduction

1.1 Background and motivation

Global warming and the fast depletion of fossil fuel reserves are the two main concerns involved with the extensive use of fossil fuels around the world. Since the start of the industrial revolution the use of fossil fuels to power the growing economies has increased steadily. For this year, 2010, the world's primary energy consumption is estimated to be 0,15 $\times$ 10^{15} kWh, from which 85% has a fossil fuel origin [1]. The latest estimations show that the world's coal, gas and oil reserves will be exhausted in respectively 2112, 2042 and 2040 [2]. Besides, despite the recent criticism, it is quite clear the immense amounts of carbon dioxide (CO_2) emissions resulting from the burning of fossil fuels contribute to the global warming [3]. Based on the rapidly approaching depletion of fossil fuels and the ever rising energy demands it's absolutely clear that alternative energy sources are needed.

Amongst alternative energy sources such as wind, geothermal, tidal and biomass, solar energy or photovoltaic (PV) is one of the sources of alternative energy which can play an important role in realizing long-term sustainability of energy consumption. The photovoltaic effect is the effect of direct conversion of solar energy into electricity; without moving parts, noise or any form of emissions electricity is produced. Since the introduction of the first bulk crystalline solar cells in the late 1950ties the price of the modules and thereby the price per kWh produced has dropped significantly. Solar electricity is however, for the largest part of the world, not economically feasible yet [4]. To become more competing, alternatives for the bulk crystalline type solar cells have to be developed.

Thin-film silicon solar cells are amongst the most promising candidates for future PV modules. This type of solar cell combines the advantages of lower material use, lower process temperatures and is suitable for continuous roll-to-roll production on flexible and cheap substrates. The current efficiencies of thin-film solar cells are however still limited when compared

with bulk crystalline solar cells, besides these cells are also known to suffer from light-induced degradation. The main focus of todays research is therefore aimed at improving these main issues [5].

Within the Photovoltaic Materials and Devices (PVMD) group at Delft University of Technology the research on thin-film solar cells is focused at improving the efficiency by means of material improvement, light management / trapping and novel absorber materials such as nanoparticles and photonic crystals. The technique of light trapping is aimed at capturing as much incident photons in the active layers of the solar cell as possible, which can be achieved by scattering the light at rough interfaces. This roughness can be introduced into the solar cell by increasing the surface roughness of the so-called Transparent Conductive Oxide (TCO) at the front of the solar cell and the back reflector (see section 1.3).

The TCO forms the top electrode of the solar cell and its main function is therefore the effective conduction of charge carriers (electrons) to the external circuit whilst offering high transparency over a wide spectrum. The TCO replaces the current collection grids used in bulk crystalline solar cells (c-Si), thereby reducing losses due to shading. Sub cells of thin-film solar cells, deposited on a single substrate, are connected in series by means of laser scribing. By using this monolithically integration of a-Si:H solar cells the desired voltage from a single substrate can be easily achieved.

Indium tin oxide (ITO) is one of the most widely used TCOs, offering excellent transparency and very low resistivity. Application of ITO in the PVMDs solar cells should reduce ohmic losses and hence increase the overall efficiency. This thesis focuses on the meticulous process of ITO TCO optimization by varying the interrelated deposition parameters and thereby assisting in the research on thin-film silicon and HIT solar cell technology.

1.2 Solar cells

The first observation of the photovoltaic effect was done by the French physicist Alexandre-Edmond Becquerel in 1839. Almost 50 years later, in 1883, Charles Fritts coated a selenium semiconductor with a very thin film of gold and thereby created the first working solar cell with an efficiency of 1% [6]. The current bulk crystalline silicon solar cells were first developed in the 1950ties by Chapin et al. at Bell Laboratories who found that silicon doped with impurities is particlurarly sensitive to light [7]. This type of solar cells is now known as the ‘first generation’ solar cells and have reached laboratory efficiency of over 25.0% whilst actual module efficiencies have reached 23.9% [8].

To improve the cost-effectiveness of the c-Si solar cells research around the world has focused on decreasing the material costs and using less energy intense production processes, resulting in the development of low cost

thin-film solar cells also known as the ‘second generation’ solar cells. Several semiconducting materials, such as copper indium gallium diselenide (CIGS), cadmium telluride (CdTe) and hydrogenated amorphous silicon (a-Si:H) have found application in these thin-film solar cells. Whereas CIGS and CdTe solar cells use rare earth materials, leading to increased costs, amorphous silicon is produced from abundant materials. Thin-film amorphous silicon solar cells are therefore one of the most promising candidates to replace current c-Si solar cells. The thin-film silicon solar cells are described in more detail in the next section (section 1.3).

The upper limit of solar cell conversion efficiency, based on thermodynamic calculations, is demonstrated to be 93%. In an effort to reach these 2 to 3 times higher than current conversion efficiencies advanced concepts, such as tandem or triple junction solar cells as well as quantum dots, are being researched. These concepts are known as the ‘third generation’ solar cells [9, 10].

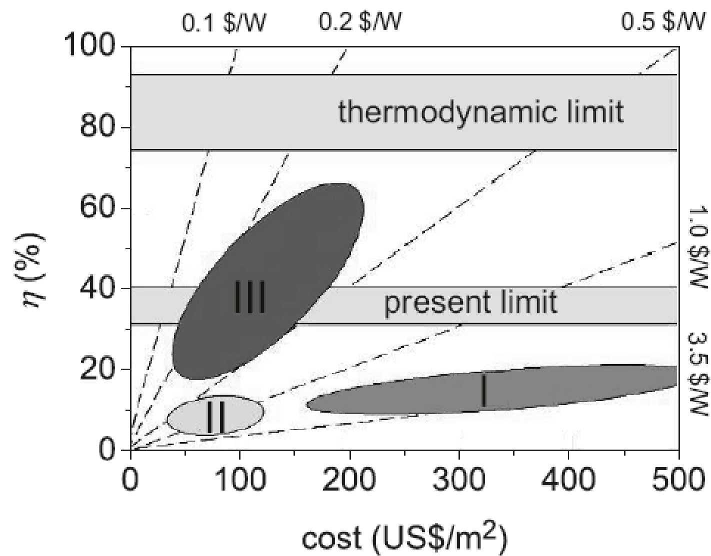

Figure 1.1: Three generations of solar cells [11]

1.3 Thin-film silicon solar cells

In this section the thin-film silicon and HIT solar cells which are being researched by the PVMD group are described.

1.3.1 Amorphous silicon solar cells

In 1976 Carlson and Wronski reported the first working a-Si:H solar cell with an efficiency of 2.4% [12]. Since then the low material use and beneficial production circumstances have atracted interest from around the world and a-Si:H efficiency has reached a maximum of 10.09% [13].

In contrast to the long range ordered structure of crystalline silicon, amorphous silicon only offers the same structural order over a very short range and lacks the long range order. Figure 1.2 visualizes the difference in atomic structure between single crystal silicon and a-Si:H. It clearly shows that in the single crystal crystal silicon structure each Si atom is bonded to it's four neighboring Si atoms through regular bonds with same length and angle. The a-Si:H structure shows that small deviations in bonding angles and lengths between neighboring Si atoms result in a complete loss of ordered structure [10].

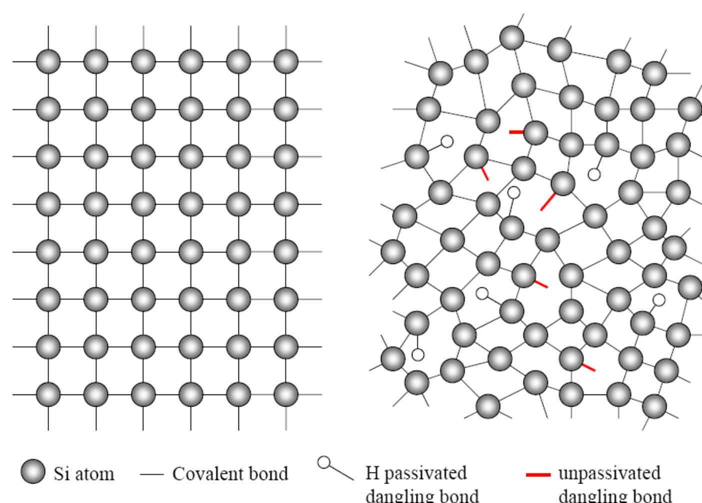

Figure 1.2: Schematic representation of atomic structure of single crystal silicon (left) and hydrogenated amorphous silicon (right) [10]

Due to the variations in both bonding angles and lengths between the neighboring atoms weak bonds are formed. These weak bonds can easily break thereby forming a so-called defect. Si atoms that are only bound to three of its neighbors have one unpaired electron which is known as a dangling bond. The dangling bonds act however as a trap for free charge carriers. By passivating the dangling bonds with hydrogen the number of dangling bonds can be reduced drastically, thereby increasing the diffusion length of the carriers.

Single crystal silicon shows a distinct separation between the conduction band and valance band, called the band gap. Due to the disorder in a-Si:H there is no well defined band gap between the valance band and conduction

band (see Figure 1.3 on page 5). In fact, the energy states of both valence and conduction band spread into the band gap thereby forming so-called band tail states, which represent the energy states of electrons that form the strained bonds in a-Si:H.

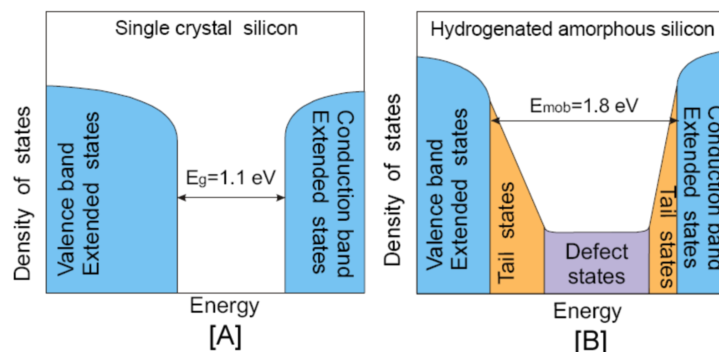

Figure 1.3: Distribution of density of allowed energy states for single crystal silicon [A] and a-Si:H [B] [10]

One major beneficial effect of the disorder in a-Si:H is that it absorbs almost 100 times more light from the visible part of the solar spectrum than c-Si. This allows much thinner absorption layers thereby significantly reducing the amount of material needed and thus reducing the production costs.

Although the absorption in a-Si:H is high and the passivation with hydrogen is able to significantly increase the diffusion length of the free charge carriers, the mobility of the free charge carriers is still too small to enable them to travel to the external circuit without recombining. To overcome this problem p-type and n-type layers are added to the intrinsic absorber layer. These two layers set up an electric field across the active intrinsic a-Si:H which should be high enough to ensure collection of the photo-generated charge carriers. Besides it allows low-loss ohmic transport and collection of the free charge carriers to the external contacts.

The p-type and n-type layers are effective in generating an electric field, though their resistivity is still too high to be of effective use as top or bottom electrode for the a-Si:H device. Application of a so-called Transparent Conductive Oxide (TCO) on the top side of the solar cell and a back contact made of silver or aluminum on the back side further reduce the ohmic losses (see Figure 1.4). The function of the TCO is twofold: it needs to be as conductive as possible whilst also being as transparent as possible since the light has to pass true this layer before reaching the actual active layer of the a-Si:H solar cell. The TCO is described in more detail in section 2.1.

Depending on the substrate, a-Si:H solar cells can be deposited in so-called p-i-n superstrate or n-i-p substrate configuration which reflects the

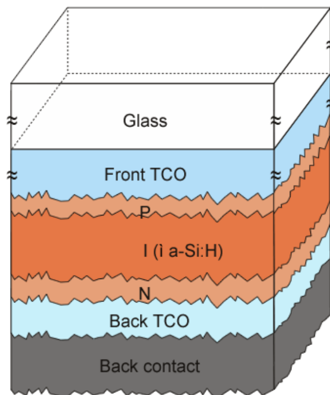

Figure 1.4: General structure of a-Si:H solar cell

deposition sequence used. For superstrate p-i-n devices the p-type layers is deposited on top of a transparent substrate first, followed by the intrinsic layer and the n-type layer is deposited as the last one. Substrate n-i-p devices are deposited in the reverse order. However, the substrate for n-i-p devices is a non-transparent material such as stainless steel.

1.3.2 Microcrystalline silicon solar cells

The first microcrystalline silicon layers were deposited by Veprek and Marecek in 1986 [14], it took however until the early 1990ties until the first actual microcrystalline solar cell was produced by Meier et al. at IMT Neuchâtel, Switzerland [15].

Microcrystalline silicon is a mixed phase of amorphous and crystalline silicon and grain boundaries; small crystals of highly ordered material are embedded in the amorphous structure. The growth of a μc-Si:H layer always starts in an amorphous phase, in the continuing depositions clusters of crystallites grow until a saturated crystalline fraction is achieved. Microcrystalline silicon is generally produced using a higher hydrogen dilution ratio than a-Si:H; the development and growth of the crystallites is enhanced by the presence of atomic hydrogen due to the chemical interaction with the growing surface. The incubation and crystallization phase as a function of the source gas dilution with hydrogen is visualized in Figure 1.5.

Compared to a-Si:H, microcrystalline silicon with a sufficiently high crystalline volume fraction suffers less from light induced degradation (Staebler-Wronski effect [16]). In relation to bulk crystalline solar cells μc-Si:H solar cells require, as a-Si:H solar cells do, less material due to the higher absorption. Low temperature deposition, the possibility of roll-to-roll production on flexible substrates and increased deposition rates offer reductions in production costs.

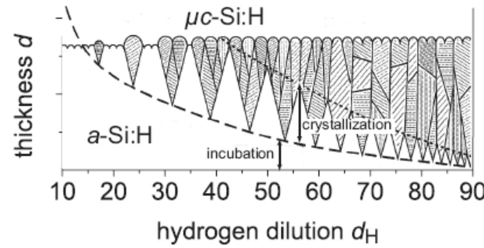

Figure 1.5: Schematic representation of microcrystalline growth mechanism [11]

1.3.3 Tandem solar cells

Solar cells with different optical bandgaps can be stacked together to form so-called tandem or triple junction structures. These stacks of solar cells combine materials with different bandgaps thereby using the incident light more efficiently, are able to obtain a higher open circuit voltage whilst at the same time the current density is reduced and can reduce the light induced degradation by using a thin amorphous top cell [5].

The microcrystalline / amorphous silicon tandem solar cell is also known as the 'micromorph' tandem or 'hybrid' cell. The challenge of these micromorph solar cells is to match the top and bottom cells' photogenerated current. In practice this results in a relatively thick microcrystalline bottom cell combined with a relatively thin amorphous absorber layer (Figure 1.6).

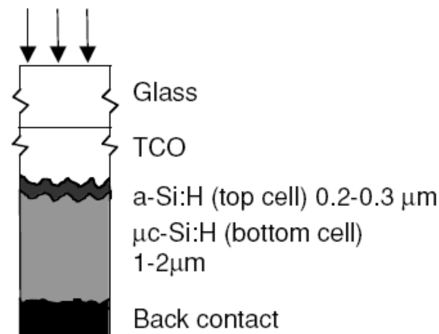

Figure 1.6: Schematic structure of superstrate micromorph solar cell [5]

Laboratory scale stabilized efficiencies of 11 - 12% have been acheived whilst commercial modules are available with an efficieny of over 8% [5].

1.3.4 HIT solar cells

The final type of solar cell which is being researched by the PVMD group is the Heterojunction with Intrinsic Thin Layer (HIT) solar cell. Sanyo

company from Japan was and is the pioneer with this approach, reporting a poly-Si HIT solar as early as 1990 [17]. The structure of a typical HIT cell is shown in Figure 1.7. A p-n junction is created by depositing non-doped a-Si and p-type a-Si thin layers on top of an n-type crystalline silicon substrate. On the back side a back-surface field (BSF) structure with non-doped a-Si and n-type a-Si layers is used. On both doped layers a TCO, due to the low lateral conductance, and metal contacts are applied. During processing the temperature does not exceed 200°C. At the moment the record efficiency for a HIT solar cell is 23.0 ± 0.6%, whilst commercial modules with an efficieny of 19.5% are now widely available [18].

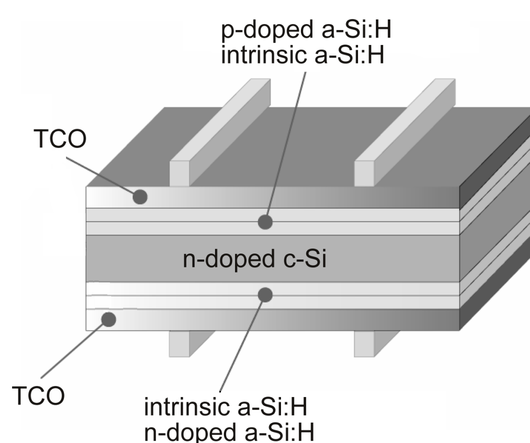

Figure 1.7: Structure of HIT solar cell [18]

1.3.5 Air Mass and spectral range

The extraterrestrial spectrum of solar radiation outside the earth's atmosphere, also known as air mass 0 (AM0), as well as the terrestial solar radiation standard which is used for solar cell performance tests (AM1.5) are presented in the figure below (Figure 1.8). In this figure the green shaded area indicates the wavelength range in which a-Si:H solar cells operate (400 - 750 nm), the gray shaded area visualizes the wavelength range in which μc-Si:H solar cells operate (600 - 1100 nm). These two shaded areas combined indicate the wavelength range in which the HIT solar cells operate (400 - 1100 nm).

1.4 Outline of the thesis

A crucial part of thin-film silicon and HIT solar cells is the transparent conductive oxide since it needs to simultaneously offer high transmittance in the wavelength range of interest and high electrical conductivity. In

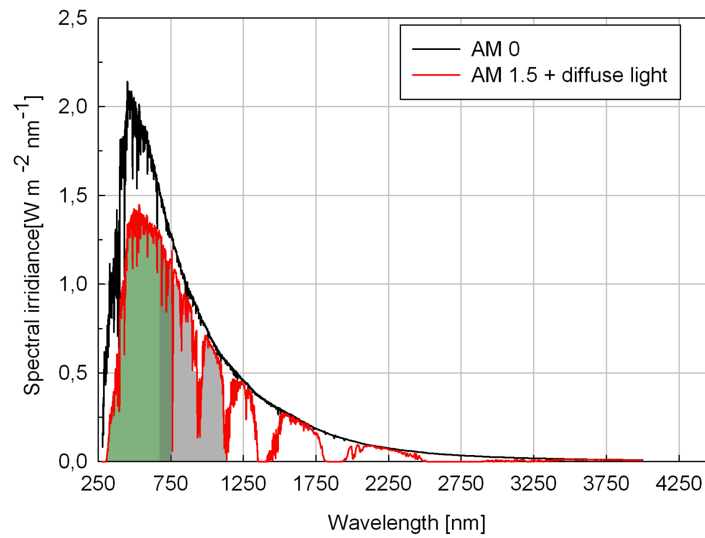

Figure 1.8: Spectral power density of sunlight. The different spectra refer to the extraterrestrial AM0 radiation and the AM1.5 radiation

this thesis the meticulous optimization process of tin-doped indium oxide TCO for application in a-Si:H, μc-Si:H and HIT solar cells is described. The quality of the ITO depositions is a direct consequence of a variation of interrelated process parameters such as power density, temperature and pressure. A Figure of Merit is used to determine the optimal recipes for the different types of thin-film solar cells. Optimized recipes are subsequently applied to TCOs of actual a-SI:, μc-Si:H and HIT solar cells.

Chapter 2

Theoretical background

In this chapter transparent conductive oxides (TCOs) for solar cell application are described (section 2.1), followed by a detailed description of the main subject of this thesis: tin-doped indium oxide (ITO) TCO (section 2.2). The chapter is concluded by an overview of TCO deposition techniques, with a strong emphasis on radio frequent (RF) magnetron sputtering (section 2.3).

2.1 Transparent Coductive Oxides

The first transparent conductive oxide (TCO) was reported by Baedeker, describing the optical and electrical characteristics of primitively vapor deposited cadmium oxide (CdO) [19]. TCOs are currently found in a wide range of optoelectronic applications, varying from energy saving windows to gasochromic devices, liquid crystal displays (LCD) and thin-film solar cells [20, 21, 22, 23, 24].

The TCO is a fundamental component of thin-film solar cells and has a decisive role on currently achieved efficiencies. It forms the top electrode of the solar cell and its main function is therefore the effective conduction of charge carriers to the external circuit whilst offering high transparency over a wide spectrum. The TCO replaces the current collection grids used in bulk crystalline solar cells (c-Si), thereby reducing losses due to shading, although, if not well optimized, TCOs may suffer of undesired absorption. Sub cells of thin-film solar cells, deposited on a single substrate, are connected in series by means of laser scribing. By using this monolithically integration of a-Si:H solar cells the desired voltage from a single substrate can be easily achieved.

Besides high optical transmittance over a wide spectrum combined with a reasonably high conductivity, the choice of TCOs for thin-film (silicon) solar cells is based on additional considerations, including work function, band alignment, ability to scatter incoming light, favorable physical and chemical properties to allow the growth of silicon, materials composition, processing

and cost. The ability to scatter incoming light is particularly important for thin-film solar cells since it can significantly enhance the conversion efficiency. Scattering is achieved by texturing the TCO surface. The path of the incident photons is changed due to the rough surface thereby increasing the chance of the generation of an electron-hole pair. Several methods are used to increase the surface roughness of a TCO such as wet-chemical etching, plasma etching and varying deposition parameters. The principle of light scattering at rough surfaces is shown in Figure 2.1.

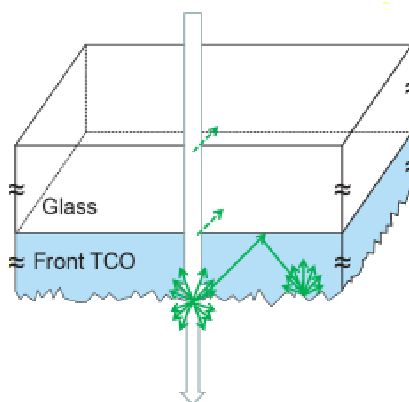

Figure 2.1: Principle of light scattering due to TCO surface roughness

Amorphous silicon solar cells typically use fluorine doped SnO2 or ITO as front TCO since these can be deposited at low temperatures (<200C) and are able to withstand the relatively high post-deposition temperatures (>350C) for short times (<10 min) in a mildly reducing ambient without losing performance. Typical requirements for for TCOs to be used in a-Si:H based solar cells are chemical and structural stability, low cost and ability to be textured easily. With the increasing importance of light management, zinc oxide (ZnO) combined with various dopants such as Ga and Al have increasingly attracted interest. Because high quality (crystalline) ITO is difficult to pattern due to its slow and highly crystallographic anisotropic etch rate, researchers are looking for alternative materials. Doped zinc oxide (ZnO) is an interesting candidate since it allows low temperature deposition. Strong texture-dependent surface morphologies can be achieved by doping with Ga (ZnO:Ga or GZO) whereas aluminum doped zinc oxide (ZnO:Al or AZO) can be texture-etched in diluted 0.5% HCl. Both AZO and GZO have been applied in a-Si:H solar cells [25, 5].

Besides high transparency over the spectral range and a high conductivity, TCOs for microcrystalline silicon (μc-Si:H) solar cells require excellent light scattering capability through their surface texture and chemical stability with respect to deposition of silicon layers by means of plasma enhanced chemical vapor deposition (PECVD). ITO is excluded as TCO for μc-Si:H

solar cells since it is not stable when exposed to a silane plasma; deposition of silicon based layers on top of ITO leads to serious problems with indium diffusion and lifetime reduction in the silicon layers. Fluorine doped tin oxide (SnO_2:F or FTO) offers good light scattering and is regularly used as TCO for a-Si:H solar cells. However, FTO cannot be used directly as front TCO for superstrate μc-Si:H solar cells since the subsequent deposition of the μc-Si:H requires a hydrogen rich plasma, which reduces the SnO_2 layer and thereby affects its transparency. Thin layers of ZnO or TiO_2 have been deposited on top of the SnO_2:F or ITO in order to make it resistant to the hydrogen-rich plasma [5].

HIT solar cells require highly conductive TCOs deposited at low temperatures and which are able to form good contacts with the n+ amorphous silicon (a-Si:H) layer. Usually ITO is used, but it should be noted that, considering the limitation in deposition temperature, the highest possible quality cannot be achieved. There is an increasing interest in the use of amorphous indium zinc oxide (IZO), which allows room temperature deposition but also implies a reduced conductivity [25].

2.2 Tin-doped indium oxide (ITO)

Amongst TCOs tin-doped indium oxide is the most widely used due to its unique combination of electrical and optical properties, offering both high transmittance (>90%) and conductivity ($1 \times 10^4 \Omega^{-1}\text{cm}^{-1}$). In this section the physical structure 2.2.1, electrical properties 2.2.2 and optical properties 2.2.3 of ITO will be described in detail, followed by a more commercial point of view on the current and future availability of ITO

2.2.1 Physical structure

ITO is a highly degenerate *n*-type wide bandgap semiconductor which is essentially formed by substitutional doping of In_2O_3 with Sn. The Sn replaces the In^{3+} atoms from the cubic bixbyite structure of the indium oxide, thereby forming interstitional bonds with oxygen through which Sn exists either as SnO or SnO_2^-, accordingly it has a valency of +2 or +4 [26].

Nadaud et al. [27] studied the structural changes of indium oxide due to tin doping. They showed that the cubic bixbyite structure[1] shows a fluorite-related superstructure where onefourth of the anions are missing. The indium cations are located in two different six-folded-coordinated sites, Figure 2.2.

Resulting from the lower valence state, the carrier concentration is reduced due to the creation of a hole acting as an electron trap and thereby reducing the electrical conductivity. Alternatively, prevalence of the SnO_2

[1] C-type, rare-earth sesquioxide structure: $Ia3$ space group, No. 206

state results in Sn^{4+} actings as a n-type donor releasing electrons to the conduction band. Yet both substitutional Sn and oxygen vacancies were found to contribute to a high conductivity and the material could be represented as $In_{2-x}Sn_xO_{3-2x}$ [28]. The lattice constant was found to increase 0.05% due to Sn doping (up to 5 - 6% Sn) albeit the Sn^{4+} radius is smaller than that of In^{3+} (0.71 versus 0.81 Å) [27].

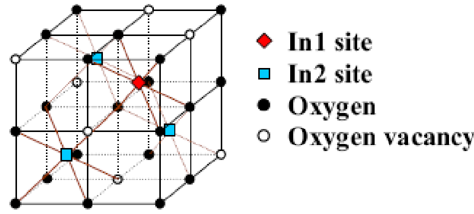

Figure 2.2: Cationic sites in the cubic In_2O_3 structure [27]

2.2.2 Electrical properties

The main electrical properties of ITO are characterized by the free carrier density N, carrier mobility μ and conductivity σ, which share the following relation:

$$\sigma = N\mu e \tag{2.1}$$

where e is the elementary charge. Conductivity is inversely related to the resistivity ρ:

$$\sigma = \frac{1}{\rho} \tag{2.2}$$

The above relation illustrates that for obtaining high conductivity both free carrier density (2.3) and mobility (2.2.2) should be maximized.

Free carrier density

Frank and Köstlin described two different mechanisms from which free carriers arise in ITO: substitutional tetravalent tin atom and divalent oxygen vacancies. They found that the free carrier density depends on defects being introduced into the bixbyite structure. In their work they described five governing lattice defect [29] which will be described below.

Impurity ions -substitutional tin (Sn^*) Since indium has a valence of 3, using tin as a cationic dopant substituting indium results in n-type doping

of the lattice by providing an electron to the conduction band, thereby keeping charge neutrality preserved:

$$Sn_{in} \rightarrow Sn^{*} + e^{-} \quad (2.3)$$

where superscript * represents the positive charge.

Neutral defect ($Sn_2^*O_i^{''}$) Two Sn^{4+} ions which are on their nearest neighbor positions can loosely bound to an interstitial oxygen anion, forming the neutral compound $Sn_2^*O_i^{''}$. This interstitial defect can however dissociated when annealed under reducting conditions; O_i can drift out ($Sn_2^*O_i^{''} \Leftrightarrow 2Sn^*$ + $2e^-$ + $0.5O_2^{(g)}$). This effect is therefore indicated as not being 'harmful'.

$$O_i^x + 2e^- \Leftrightarrow O_i^{''} \quad (2.4)$$

Where O_i^x is the interstitial oxygen and the superscript $''$ stands for the two negative charges.

Neutral defect ($Sn_2^*O_4$)^x Formation of Sn_2O_4, with a Ca_2F_4 like structure, is possible when two nearest-neighbour Sn^{4+} ions bound to their three nearest neighbours on regular anion sites and an additional interstitial oxygen ion bounds on its nearest quasianion site. This situation occurs at high doping levels and is, because of the strong Sn-O bond which can not be reduced by means of heat treatment, indicated as a "harmful" effect.

Defect ($Sn_2^*O_i^{''}$)($Sn_2^*O_4$)^x Very high doped system are known to bring forward associate neutral defects composed of the two above mentioned defects, excisting of both loosely and strongly bound surplus oxygen.

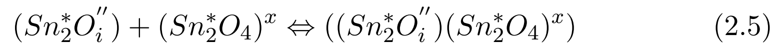

$$(Sn_2^*O_i^{''}) + (Sn_2^*O_4)^x \Leftrightarrow ((Sn_2^*O_i^{''})(Sn_2^*O_4)^x) \quad (2.5)$$

Oxygen vacancy V_0^{**} Oxygen vacancies act as double ionized electron donors contributing a maximum of 2 electrons as illustrated by the following equation [30]:

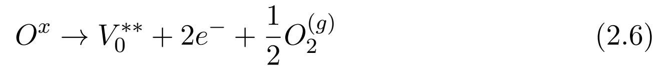

$$O^x \rightarrow V_0^{**} + 2e^- + \frac{1}{2}O_2^{(g)} \quad (2.6)$$

Oxygen rich deposition will will result in a oxygen saturated thin film.

Increasing the deposition temperature shifts equilibrium Eq. (2.3 and 2.4) to the left, creating free electrons and dissolving the interstitional oxygen and substitutional Sn. Interstitional oxygen (O_i) can diffuse through the lattice and reach the grain boundaries, at these grain boundaries absorbed oxygen (O−2(a)) can be formed and desorbed [31].

Limitations of free carrier density Köstli et al. [32] studied the optical and electrical properties of ITO prepared by a pyrolytic method and found that there is a theoretical maximum carrier density N of:

$$N = N_{in} \times c \tag{2.7}$$

where $N_{in} = 3.0 \times 10^{22}$ cm^{-3} is the concentration of indium atoms and c is the concentration of tin atoms. In practice however, the carrier concentration does not increase as expected. However, in practice a portion of the tin atoms are deactivated at higher doping levels. This is caused by the fact that the higher the tin content, the more probable the tin ions will occupy the nearest-neighboring anion site thereby forming neutral defects (Sn_2O_4) as described above. This emphasizes that optimization of free carrier density through doping is a meticulous process.

Free carrier mobility

Increasing the conductivity by means of the carrier concentration results in a significant loss of transmission; hence increasing the conductivity by increasing the free carrier mobility is of great importance for achieving high quality TCOs.

Scattering mechanisms The free carrier mobility can be defined as:

$$\mu = e\tau m_{eff} \tag{2.8}$$

where τ is the average collision time of electrons ans m$_{eff}$ is the effective electron mass in the conduction band.

Many sources of scattering which may influence the free carrier mobility can be defined: ionized impurity scattering, neutral impurity scattering, grain boundary and external surface scattering, acoustical phonon scattering, defect lattice scattering, etc [33]. Scattering due to grain boundaries and acoustic phonons was found to play a minor role since the mean free path of the electrons is, in the vast majority of the cases, smaller than the crystallite size and there was no temperature dependence observed between 100 and 500 °C. At the same time grain boundary scattering is in some cases reported as an important factor contributing to a decrease in carrier mobility [34]. A wide range of grain sizes combined with a high electron mean free path are essential for the scattering effect of grain boundaries.

The motion of free electrons might be obstructed by domain boundaries actings as barrier height in the conduction band [35]. For ITO films with larger domains it may therefore be expected to have an increased Hall mobility. ITO films with good crystallinity are expected to suffer little from electron scattering by dislocations and precipitation. In addition, surface scattering does not affect the mobility of the free carriers except when the

mean free path is comparable to the film thickness. However, for degenerate type semiconductors with high carrier concentrations Scattering by neutral and ionized impurities as well as the interaction (for closed pair of impurities) cannot be neglected.

Ionized donor impurities are essential in order to keep the charge of the doped film neutral. The Coulomb forces between the impurities and the free electrons provide a source of scattering that is intrinsic to the doped materials. As a result the ionized impurity scattering implies a lower limit for the carrier mobility, independent of the other scattering mechanisms which are more dependent on the deposition process [36].

Bel Hadja Tahar et al. [33] mentioned the relation below to describe the effect of neutral and charged scattering centers on the mobility of degenerate semiconductors:

$$\mu_i = \frac{\left[24\pi^3 \left(\epsilon_0 \epsilon_r\right)^2 h^3 n\right]}{\left[e^3 m^{*2} g\left(x\right) Z^2 N_i\right]} \tag{2.9}$$

where n is the carrier concentration, Z is the charge of the ionized centers, ϵ_0 is the permittivity of free space, m^* is the effective mass of the free electrons, ϵ_r is the low-frequency relative permittivity and $g(x)$ is the screening function. For ITO where $Z = 1$ and $N_i = n$, and m^* and ϵ_r are taken 0.3 m_0 and 9 [32], a limit of 90 $\mathrm{cm^2/Vs}$ was obtained by Bellingham et al. [36].

2.2.3 Optical properties

The optical properties of ITO are governed by three types of electronic excitation: band gap transitions, interband transitions from the bulk of the valence band into the bulk of the conduction band and intraband transitions of free electrons in the conduction band. From these excitations three different regions can be distinguished in the ITO transmission curve, illustrated in figure 2.3. The ultraviolet region (short wavelength, high energy) shows a strong absorption edge, known as the band edge which is governed by the ITOs band gap transition. In the visible wavelength range quite high transmittance is present and interference fringes causing minimum and maximum extremes are clearly visible. Leaving the visible wavelength range and going into the infrared region a strong increase in reflection is visible. Both increase in reflection and absorption take place at the so-called plasma edge which is associated with the excitation of free electrons in the conduction band.

Snell's law

Upon encountering an interface separating two different media, light will either be reflected or transmitted. The refractive index of a material, n, not only determines the transmittance and consequent reflectance of incoming

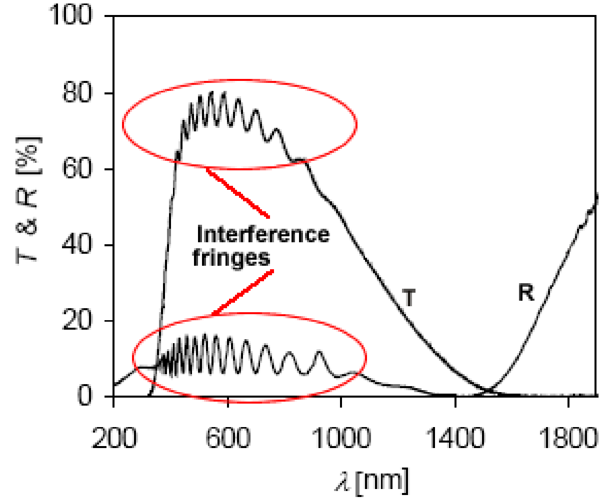

Figure 2.3: Transmittance and reflection

light, but also the angle at which light is being transmitted. The relation between the angle of incident light θ_i and the angle of the transmitted light θ_t is given by Snell's law [37]:

$$n_1 \cdot \sin(\theta_i) = n_2 \cdot \sin(\theta_t) \tag{2.10}$$

where n_1 and n_2 denote the refractive indices of the two media. The refractive index for ITO is, for example, 1.96 at 500 nm [38].

When considering absorbing films, the refractive index is a complex quantity with a real part n and an imaginary part k (extinction coefficient). The complex refractive index $\tilde{n}$ is related to the complex permittivity or dielectric function ($\epsilon = \epsilon_1 + i\epsilon_2$) through:

$$\tilde{n} = n + ik \left(= \sqrt{\epsilon_1 + i\epsilon_2}\right) \tag{2.11}$$

$$\epsilon_1 = n^2 + k^2, \epsilon_2 = 2nk \tag{2.12}$$

Band structure

The high optical transmittance of ITO originates from its wide bandgap; for ITO a direct bandgap of around 3.75 eV is reported and an indirect bandgap of around 2.6 eV [39], although the work from Fan and Goodenough [26] and Balasubramanian [40] reported a bandgap which is generally greater than 3.75 eV with a range varying from 3.5 to 4.06 eV.

Undoped In_2O_3 is assumed to have a parabolic shaped band structure where the conduction band is empty and curved upwards, the valence band is curved downwards and the Fermi energy level (E_f) is located at the middle of

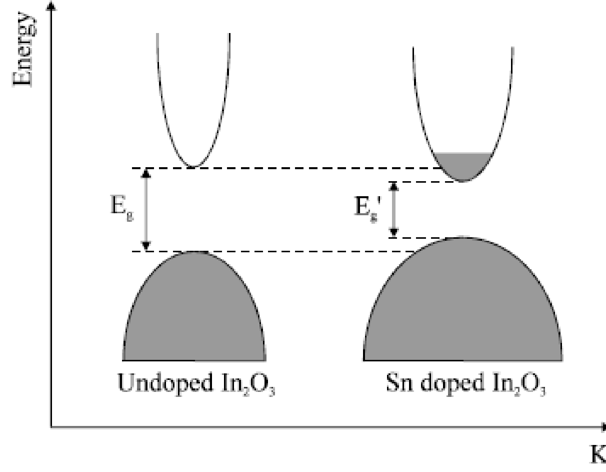

Figure 2.4: Assumed parabolic band structure of undoped indium oxide and the effect of tin doping [41]

the bandgap (Figure 2.4). Introduction of a low density of Sn atoms results in the formation of donor states just below the conduction band whilst the Fermi level is situated between the donor level and the conduction-band minimum. Increasing the doping level will eventually lead to the conduction band merging with the donor states at a certain critical density, n_c, which was calculated to be 2.3 x 10^{19} cm^{-3} [41]. When the density of free electrons from the donor atoms exceed this critical value, free electron properties are experienced by the material.

Burstein-Moss shift

With increasing carrier concentration the fundamental absorption edge will shift towards higher energy levels (lower wavelength). This bandgap widening is known as the Burstein-Moss shift (BM) [42, 43]; which is described by the relation below for parabolic band edges:

$$\Delta_g^{BM} = \left(\frac{\eta^2}{2m_{vc}^*}\right)\left(3\pi^2 n_e\right)^{2/3} \tag{2.13}$$

where n_e is the density of electrons in the conduction band and m_{vc}^* is the reduced effective mass as defined by:

$$\frac{1}{2m_{vc}^*} = \frac{1}{m_v^{eff}} + \frac{1}{m_c^{eff}} \tag{2.14}$$

where m_v^{eff} and m_c^{eff} are the effective mass of the conduction band and valence band.

In general the bandgap exhibits an $N^{2/3}$ dependence due to the BM [41], although the widening of the band gap is partially compensated by mutual exchange and coulombic interactions which shift the conduction band downwards and the valence band upwards.

2.2.4 Availability

The last decade has shown a steep increase in ITO demand resulting in a sharp rise in price. Indium is a rare earth material with concentrations in the earth's crust which are comparable to silver (around 0.1 part per million).

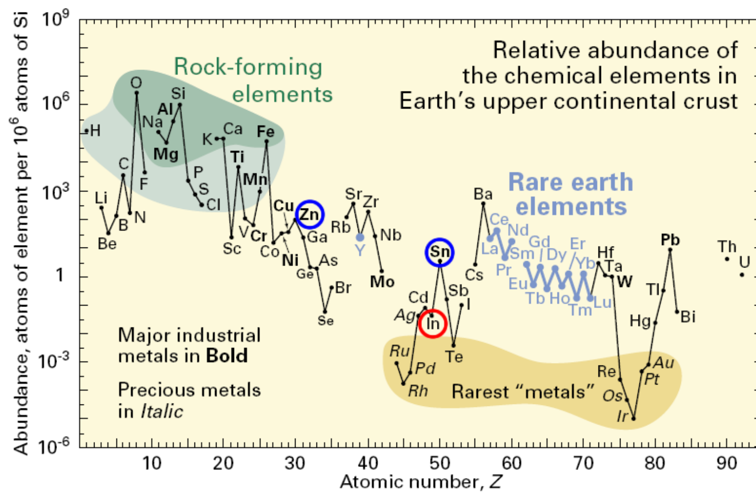

Figure 2.5: Abundance (atom fraction) of the chemical elements in Earths upper continental crust as a function of atomic number. Indium is indicated by the red circle, zinc and tin by the blue circles [44].

There are no specific indium mines, although indium is associated with tin, lead, copper and iron ores it is most commonly found in association with zinc-bearing materials [45]. In 2009 597 metric tons of indium were refined; with an estimated global economically recoverable indium reserve of 16,000 metric tons (based on concentration in zinc ores) it is quite obvious that there will be a shortage of indium within the coming 30 to 40 years.

2.3 Deposition techniques

Amongst the deposition methods available for ITO thin films, thermal evaporation (section 2.3.1), chemical vapor deposition (CVD) (section 2.3.2), spray pyrolysis (SP) (section 2.3.3), screen printing technology (section 2.3.4) and (reactive) sputtering (section 2.3.5) are the most frequent used techniques. Within the scope of this report RF magnetron sputtering was

used to deposit ITO, the governing process parameters are therefore described in sub-sections 2.3.5 to 2.3.5.

2.3.1 Thermal evaporation

The thermal evaporation process involves the evaporation and subsequent condensation of evaporated particles on a substrate under vacuum conditions (pressure below 1×10^{-6} Pa) [46]. The process is initiated by resistively heating or by firing an electron or ion beam at the so-called boat which carries the material to be evaporated. Hamberg and Granquist [47] described the benefits of thermal evaporation as: being able to yield thin films without considerable amounts of uncontrollable contaminations, easy to operate and, most important, low probability of substrate damages due to the absence of high velocity particles.

High quality and repeatable ITO depositions can be achieved by reactive thermal evaporation, where oxygen is introduced into the vacuum chamber during deposition [48]. Introduction of oxygen is needed since In_2O_3:Sn decomposes to some extent into sub oxides and free oxygen. The release of oxygen causes a non stoichiometry in the thin film [31].

2.3.2 Chemical vapor deposition

The process of chemical vapor deposition (CVD) involves the vaporization and thermal decomposition of a volatile compound into atoms or molecules at the surface of a substrate. These gasses, with or without reacting with other gasses, vapors or liquids generate nonvolatile reaction products on that same substrate surface thereby creating a thin film. Plasma enhanced chemical vapor deposition (PECVD) uses electric power to generate a plasma. The plasma, mostly consisting of neutrals, raises the energy of ions and electrons traveling through it. The average electron energy is 2 to 8 eV, corresponding to electron temperatures of 23,000 to 92,800 K. Due to their inertia, the ions in the plasma are not able to get enough coupling energy from the electric field. Therefore the ions in the plasma have only slightly higher energy levels than the neutral molecules at room temperature. The electrons, with their high energy and consequently high temperature, enhance the rate of chemical reactions of the precursors [46, 49].

The governing deposition parameters are the substrate temperature, substrate material, composition of the reaction gas mixture, gas flow, total pressure and the geometry of the deposition system [31]. Bel Hadja Tahar et al. [33] showed in their work that the gas flow and deposition system's geometry determine the uniformity of the deposition, whilst the substrate temperature and gas flow control determine the deposition rate.

ITO CVD deposition is known to be problematic because of a lack of volatile and thermally stable source materials. Other problems facing the

use of CVD are involved with the limitations of the process with respect to the small areas of uniform deposition and the costs of the starting reagents [31].

2.3.3 Spray pyrolysis

Spray pyrolysis (SP) deposition of thin films is a process in which a solution is sprayed on a heated surface, where subsequent thermal decomposition and reaction of the gaseous species results in the formation of a chemical compound. The chemical reactants and deposition temperature need to be selected such that only the desired compound material condenses on the substrate whilst the unwanted products remain volatile. The SP process is above all useful for the deposition of oxides and has been used for long for the production of ITO and other TCO's because of the relatively high deposition rate, there is no need for a vacuum and due to the fact that it is a quite cheap and simple process [50].

ITO can be deposited by means of spray pyrolysis using an alcoholic solution of anhydrous indium chloride ($InCl_3$) and tin chloride ($SnCl_4.5H_2O$) with nitrogen as carrier gas and a process temperature of 400 °C. Thin films with high transmittance (90%) and resistivity of $1 \times 10^{-3}\Omega \cdot cm$ have been reported as well as films with low resistivity ($3 \times 10^{-4}\Omega \cdot cm$) with resulting lower transmittance (85%) [51, 52].

2.3.4 Screen printing technology

Mbarek et al. [21] reported the screen printing of ITO for NO_x gas sensing using a viscous organometallic paste of a dissolved combination of metallic indium and tin onto glass substrates. Based on their work and on the findings of others, [53], it can be concluded that screen printing of ITO is suitable best for quite thick ITO depositions for application in liquid crystal displays (LCD), gas sensors and possibly anti-reflection coatings for solar cells. Although the resistivity of the screen printed ITO was reported to be quite low ($< 1 \times 10^{-3}\Omega \cdot cm$), the transmittance was substantially lower with an average value lower than 80%.

2.3.5 Sputtering

The first observation of the sputter process was done by Grove in 1852 [54]; in a dc gas discharge tube the cathode surface of the tube was sputtered by energetic ions in a gas discharge, and the cathode material was deposited on the inner wall of the discharge tube. Although back in those day the supper effect was mostly seen as an unwanted effect, it was also to coat mirrors as early as 1887.

Until 1908 is was believed that the deposition of material from the cathode was the result of evaporation of material at hot spots. Between 1908

and 1960 it became clear that thermal evaporation was not the driving force; experiments with obliquely incident ions and sputtering of single crystals by means of ion beams led to the development of a momentum transfer mechanism theory.

Substantial improvements on the deposition process came in the form of RF sputtering and magnetron sputtering. The latter allows sputtering at much higher rates whilst causing less substrate damage. RF sputtering offers the possibility of sputtering of non conducting materials (insulators) [55].

Sputter principles

The sputter process is described as “the release of atoms from a solid upon a bombardment and subsequent impact of ions or highly energetic neutrals” [56]. The image below from visualizes the phenomena which may occur as a result of an incident ion:

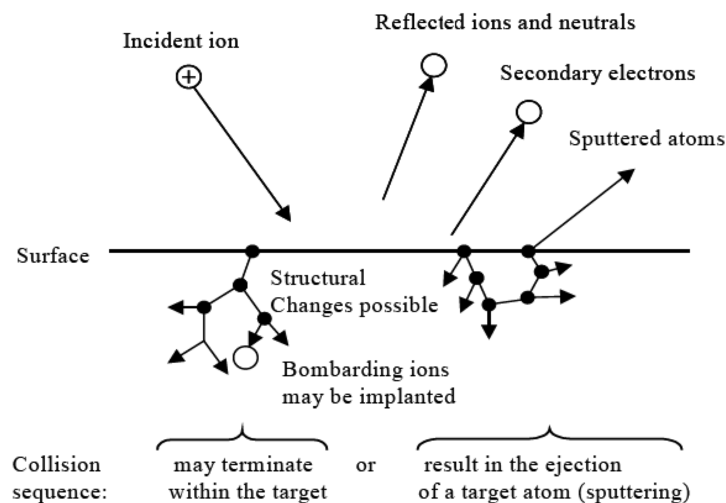

Figure 2.6: Possible phenomena arising from incident ion [57]

Chapman [57] identified 5 different scenarios resulting from an incident ion:

1. Reflection of the ion, most probably due to neutralization
2. Ejection of an electron from the target, usually referred to as a secondary electron
3. The ion can get encapsulated in the target, called ion implantation
4. The ion impact can cause some form of structural rearrangement in the target material

5. The ion can initiate a cascade of collisions between atoms of the target, which may eventually lead to the ejection of one of these atoms from the target material. The process in which an incident ion causes the release of an atom from the target material is known as *sputtering*

A surface atom is only released from the target if it receives enough energy to overcome its binding energy, which is approximately equal to the sublimation energy. Behrisch and Wittmaack [58] showed in their work that ions need to have an energy of more than around 30 eV in order to cause a cascade of collisions and the subsequent ejection of a surface atom. The sputter atoms leaving the target have a relative high energy (10 eV) when compared with evaporation atoms (0.1 eV). The necessary ions are usually provided by a plasma generated by electron impact in a noble gas at subatomic pressure. The ions are accelerated in an electric field obtained by applying a negative potential with respect to the plasma potential to an electrode immersed in that plasma. Figure 2.7 visualizes the basic principles of sputter deposition.

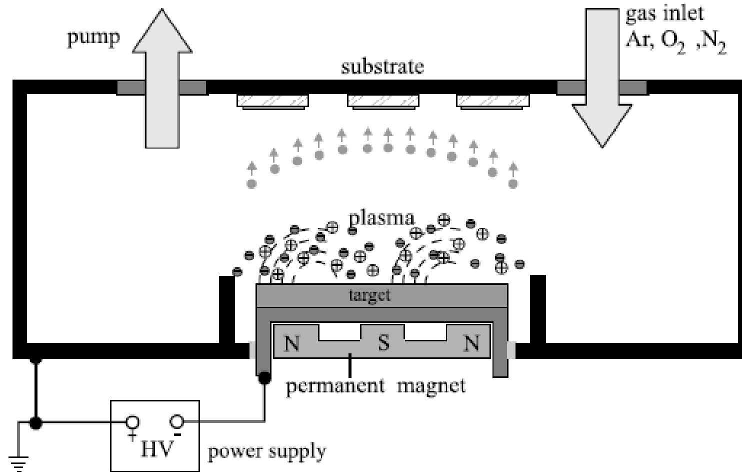

Figure 2.7: Basic principle of sputter deposition. Ions are generated in a plasma and are accelerated towards the target, impinging ions remove material from the target which subsequently condenses at the substrates [59].

The resulting sputter yield is defined as the mean number of atoms released from the target per incident ion:

$$S = \frac{\textit{number of atoms removed}}{\textit{incident ions}} \tag{2.15}$$

Or, as described by Laegreid and Wehner [60]:

$$S = 10^5 \frac{W}{AIt} \tag{2.16}$$

Where W is the weight loss of the target during sputtering time t, A is the atomic number of the target and I is the ion current.

Both Ohring [61] and Ellmer [62] described the sputter yield in a different manner, relating it to the energy of the incident ion E_{ion}, a threshold energy E_{thres}, the plasma potential V_p, the discharge voltage (dc voltage on the target) V_{dc}, the surface potential barrier U_s and the mass number of the ion (M_1) and the target (M_2):

$$S = const(E_{ion} - E_{thres}) = const \cdot e(V_p - V_{dc} - Vthres) \tag{2.17}$$

$$E_{thres} = 8U_s \cdot \left(\frac{M_1}{M_2}\right)^{\frac{2}{5}} \tag{2.18}$$

The sputter yield S, can be measured by a number of methods [56]:

- weight loss of the target
- decrease of target thickness
- collection of the sputtered material
- detection of sputtered particles in flight

Ellmer [62] showed that the resulting deposition rate R is proportional to the sputter yield S and $I(1-\gamma)$, where I is the discharge current and γ the secondary electron emission coefficient:

$$R = const \cdot SI(1-\gamma) \tag{2.19}$$

Direct current (DC) sputtering

The first systems used for sputter deposition were of the direct current (dc) type. These systems, as described by Wasa et al. [46], are composed of a pair of planar electrodes, a cathode and an anode. The top surface of the cathode is covered with a target material which faces the plasma; the substrate is placed on top of the anode. The sputter process commences when the sputtering chamber is kept in an argon gas under a pressure of around 0.1 Torr and several kilovolts of dc voltage with a series resistance of 1 to 10 $k\Omega$ are applied between the electrodes. The function of the electric field is to accelerate electrons which in turn collide with argon atoms, breaking these

argon atoms up into argon ions and more electrons to produce the glow discharge. The charged particles in the plasma are accelerated by the electric field, the electrons will move to the anode and the ions towards the cathode, allowing a current I to flow. When the argon atoms have sufficiently high energy levels sputtering of the target will occur. On the other hand, the argon ions will liberate secondary electrons from the target which are responsible for maintaining the electron supply and thereby sustaining the glow discharge. The amount of sputtered material is given by the following relation:

$$W = \frac{k_1 W_0}{pl} \tag{2.20}$$

and the deposition rate R for the dc sputter system as:

$$R = \frac{W}{t} \tag{2.21}$$

where k_1 is a constant, W_0 the amount of sputtered particles from the unit cathode area, p the discharge gass pressure, l the spacing between the cathode and anode and t the sputtering time.

Another relation is introduced below to describe the amount of sputtered particles from the unit cathode area W_0:

$$W_0 = \left(\frac{j_+}{e}\right) St \left(\frac{A}{N}\right) \tag{2.22}$$

where j_+ is the ion current density at the cathode, e the elementary electron charge, S the sputter yield, A the atomic weight of the sputtered material and N is Avogadro's number. Assuming that the ion current is almost equal to the discharge current I_s and the sputter yield is proportional to the discharge voltage V_{dc}, the total number of sputtered particles equals:

$$\frac{V_s I_s t}{pl} \tag{2.23}$$

This results in the sputtered deposit begin equal to:

$$V_s I_s t \tag{2.24}$$

Radio frequency (RF) sputtering

Insulator targets are not suitable for application in dc sputter systems. The immediate buildup of a surface charge of positive ions on the front of the insulating target material causes the glow discharge to be non sustaining. Using radio frequent (RF) sputtering the problem of charge built up at the targets' surface can be prevented. The first observation of a sputter process in a RF discharge was done by Robertson and Clapp [63] when they found that the glass surface of a discharge tube was sputtered during RF discharge.

RF sputter systems are capable of depositing conducting, semiconducting and insulating coatings and offers a number of specific benefits when compared with chemical vapor deposition (CVD) and plasma vapor deposition (PDV). Carl et al. [64] summed these advantages up as: the possibility to predict the layer structure and thickness, capability of roughly sputtering compound materials without losing target stoichiometry, deposition of good adhering and highly dense films due to the high kinetic energy of incident target atoms and a high uniformity of depositions.

A typical RF sputtering system requires an impedance-matching network between the power supply and the discharge chamber. An archetypal impedance of the RF power supply is 50 Ω whereas the impedance of the glow discharge is typically between 1 to 10 $k\omega$. The cathode current density is therefore given by:

$$i_s = C\frac{dV}{dt} \tag{2.25}$$

where C denotes the capacitance between the glow discharge and the target and dV/dt represents the time variation of the potential at the targets' surface. This relation implicates that an increase in frequency directly increases the cathode ion current. RF sputtering uses a RF frequency of 13.56 MHz, causing the target to alternatively be bombarded by ions and electrons to avoid charge built up at the targets' surface. The glow discharge is largely driven by ionization due to electrons which perform an oscillating motion within the plasma body. Whilst the electrons are able to follow the RF frequency, the ions are not because of their large inertia. Compared to dc sputtering (non-oscillating secondary electrons ionization) this type of excitation is much more effective. Chapman [4] described this benefit and found that the background pressure in the sputter chamber could therefore practically be as low as 1 mTorr. Ellmer [62] showed in his work that this type of excitation leads to lower target voltages.

Within RF sputtering systems a blocking capacitor is connected between the matching network and the target. The target area is thereby much smaller than the grounded anode and sputter chamber wall combined. Due to this asymmetric electrode configuration a negative bias is induced on the

target. this dc bias is typically on the order of one half of the peak-to-peak of the RF power supply [46].

Magnetron sputtering

In 1935, Penning carried out the first steps towards magnetron sputtering [65]. It took however until the 1970's when the planar magnetron was introduced by Chapin [66]. Decisive work on planar magnetron sputtering was done by Thornton [67]; by the end of the 70's the potential application of magnetron sputtering for Si integrated circuits made the use of it more widespread. Today planar magnetron sputtering is used on a broad scale in a wide variety of industries, ranging from architectural glass to microelectronics

Although both cylindrical and planar magnetron sputtering systems are in use, only the planar type will be described within this report since this is the most widely used type as well as the system used within this research.

Planar sputtering systems without magnetic enhancement suffer from high loss of electrons and therefore have deprived ionization efficiency. The resulting effect is that the power supply needed to drive the source needs to deliver the required current at around 2 kV. By adding magnets underneath the cathode surface, trapping of electrons close to the sputtering target is enabled. Since the residence time of the electrons in the plasma is enhanced considerably, the chance of making ionizing collisions is also much greater. It is this increased ionization efficiency, resulting in a denser plasma, which makes is possible for the plasma to carry a much higher current at a significantly lower voltage.

The general layout of a magnetron sputtering system is displayed below (Figure 2.8); within the cathode, permanent magnets are embedded creating a magnetic field of several hundred gauss. The magnetic field lines cause the electrons to be trapped near the target surface. Since the target is also a cathode, there is a crossed electric and magnetic field resulting in a drift motion of electrons along the target. Since a finite target will result in the loss of electrons, circular magnetrons are used to overcome this loss and enhance the efficiency. Arranging the magnets such that the electron drift paths return back to their starting points produces the characteristic plasma over the cathode and results in the so-called "racetrack" erosion of the target material [49].

Traditional planar magnetron systems use a balanced magnetron setup; the magnetic flux on the cathode surface is terminated to the magnetic core. Adding an additional magnetic flux superposed to the balanced magnetron creates an unbalanced magnetron. Balanced magnetron suffer from the loss of energetic electrons from the primary magnetic trap near the cathode surface, these electrons will travel to the anode. Unbalanced magnetrons trap these escaping energetic electrons by means of the excess magnetic field,

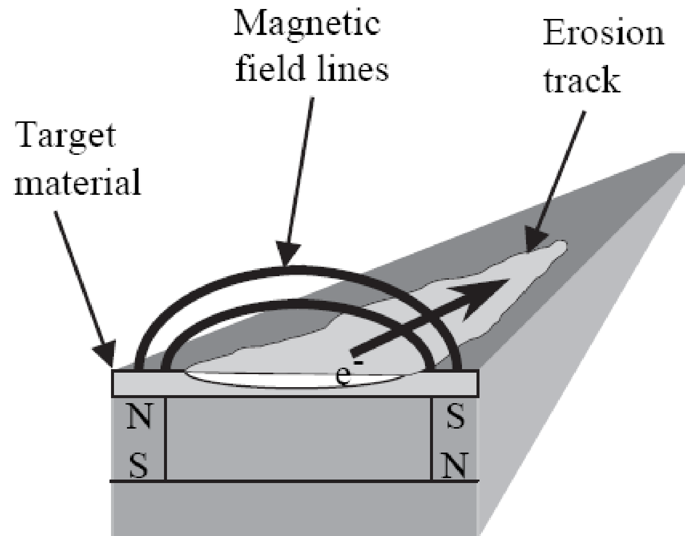

Figure 2.8: Schematic drawing showing the magnetic field lines [49]

thereby enhancing the ionizing collisions by these electrons. The unbalanced magnetrons generate a secondary plasma near the anode and the incident flux of ionized particles is increased [16].

Maximum erosion of the target material, the "racetrack", is located at positions where the magnetic field lines are parallel to the target surface. This causes the surface of the cathode to become non-uniform over time and shortens the actual life of the target. Several types of improved magnetron targets have been proposed in order to overcome this problem [68].

Deposition parameters

The quality of RF sputtered ITO is highly dependent on the process parameters such as substrate temperature (T_{sub}), oxygen partial pressure Q_{o2}, target-to-substrate distance, total pressure and sputter power. The effect of variations in these parameters will be described shortly below, additional details can also be found in the chapter 4 where experiments concerning the actual variation of deposition parameters is described.

Sputter power Research on the effects of sputtering power on the properties of ITO showed that the structure of the ITO could be changed from amorphous to polycrystalline with increasing sputter power [69]. In another study, Terzini et al. [70] observed that the carrier density of ITO films increased with increasing RF power, which was ascribed to the change in glow discharge density resulting in the formation of more oxygen vacancies.

As described in section 2.3.5, a change in plasma density results in a

change in thermalization distance of the sputtered particles thereby modifying the thin films stoichiometry and properties. Panicke and Essinger found that when the thermalization distance is larger than the target-to-substrate distance, oxygen can be removed from the growing thin-films' surface by energetic impingement of O^- ions, resulting in a <100>orientation [71]. Placing the substrate however near or far away from the thermalization distance recovers the films' stoichiometry and the crystalline structure will be <111>oriented [72].

Substrate temperature Whereas deposition methods such as e-beam (EB) evaporation need moderate substrate temperatures (150 - 160 ° C) to deposit thin-films of ITO [73], polycrystalline deposition of ITO by means of dc magnetron sputtering is possible even at room temperature (RT) [74]. El Akkad et al. [75] showed in their work that thin films of ITO deposited at RT are composed of two layers; an amorphous layer on top of the substrate covered by a polycrystalline top layer.

The substrate temperature is known to influence both microstructure and orientation of ITO films. The predominant orientation changes from (222) to (400) with increasing substrate temperature [74, 76, 77], caused by the fact that the enhanced mobility of adatoms[2] and clusters on the substrate surface favors the growth of the films along simple crystal planes such as <100>and <001>.

An increased substrate temperature also results in an increased lattice distortion, more dense depositions and increased grain size along the sample's surface. Meng and Dos Santos [74] showed furthermore that increasing the substrate temperature results in more tin atoms being diffused from the grain boundaries and interstitial lattice locations to regular In_2O_3:Sn lattice locations, resulting in higher electron concentrations. In contrast, El Akkad et al. [75] found that the lattice distortion increases with T_s, but they also observed both grain size and carrier density increase with substrate temperature.

Heating of the substrate results in heating of the plasma and target material; small increases in target temperature will significant ly increase the active energy of low melting point atoms on the target surface thereby increasing the sputtering yield [74].

Total pressure The lower and upper limit of the total pressure are determined by the requirements of both the glow discharge and thin-film deposition rate. When the total pressure is too low, the current (and hence the ion flux at the target) may become too small to sustain the plasma. Increasing the total pressure too much will, on the other hand, increase the number

[2] An adatom is an "adsorbed" atom, usually described as a single atom sitting on a crystal surface

of collisions sputtered particles undergo on their way to the substrate and thereby decrease the deposition rate.

A very low total pressure was found to contribute to a degradation of deposition crystallinity due to damage caused by the bombardment of high-energetic particles. It was observed that with an increase in total pressure the orientation of RF sputtered ITO changed from (222) to (400), whereas when the total pressure was decreased the density of the thin-film increased [78].

Target-to-substrate distance Sputtered atoms undergo collisions with the sputtering gas thereby losing part of their energy during the journey from the target to the substrate [79]. With each collision the sputtered atom looses some of its energy and after a finite number of collisions the energy of the atom will be reduced to the thermal energy of the sputter gas kT at a distance h from the target and the atom is said to be termalized [80]. The relation between the number of collisions required to thermalize an atom and the thermalization distance d_h is given by:

$$d_h = n_c \Lambda \tag{2.26}$$

where Λ is the mean free path of the sputtered atom given by $\Lambda p = 6.3 \times 10^{-3}$ mbar·cm and p is the total pressure. The thermalization distance h is thus dependent on the sputter power and pressure.

That the target-to-substrate distance is closely related to other deposition parameters is illustrated by the effect of an increase in RF power which increases the density of the sputtered neutrals and their average initial energy, consequently enhancing the number of collisions n_c and leading to a higher d_h. The total pressure changes the mean free path of the sputtered particles.

Oxygen partial pressure The oxygen partial pressure is defined as the ratio of the oxygen flux over the inert gas flux. Oxygen turns out to be quite important for the sputtering of metallic targets since low O_2 concentrations tend to result in films with quite low sheet resistance but also a somewhat metallic appearance. Increasing the oxygen concentration improves the transparency of the films, the sheet resistance is however increased as well [81].

Many authors showed that for ITO there exist a minimum of resistivity as the q_{o2} is increased [82, 83, 64], caused by two contradicting phenomena. On the one hand growth of the crystalline phase is enhanced by an increase in q_{o2}, resulting in a higher mobility of charge carriers. Controversy, the carrier density is decreased [82] due to a decrease in oxygen vacancies [84].

With increasing q_{o2} the transmittance of ITO in NIR region is significantly enhanced. This phenomena can be explained by relating it to the

reflection of electromagnetic waves due to the plasma oscillation of free carriers. The increase in transmittance is therefore very likely to be directly related to the decrease in carrier density [85].

Donut-shield In order to improve the homogeneity of the deposition a donut-shaped shield can be placed above the cathode. The plasma takes on a toroidal shape due to the magnets underneath the target, which causes a non-uniform erosion of the target. From this so-called race track more sputtered particles will consequently move towards the substrate, resulting in a non-uniform deposition. The trajectories of the sputtered particles leaving the race track can be visualized as a cone; installing the donut shield at certain height above the target will prevent the particles from continuing on their trajectories. Franken [86] showed in his work that, with the donut-shield installed at a height of 3 cm above the target, the thickness profile of deposition changed with increasing target-to-substrate height from concave to convex.

Depositions with the donut-shield were unfortunately not performed so the work of Franken could not be repeated.

Tilted angle sputtering By changing the angle of incidence of the sputtered particles a different columnar growth of the deposition can be obtained. Chen et al. reported that as the substrate is tilted at an angle, a shadowing effect results in the growth of an columnar structure film. This columnar structure exhibited high surface roughness and had intrinsically anisotropic physical properties. Anisotropic ITO films were found to have a smaller lattice content and a larger bandgap, but also a higher resistivity and a degradation of crystallization [87]. The figure below (Figure 2.9) schematically displays the principle of oblique-angle sputtering;

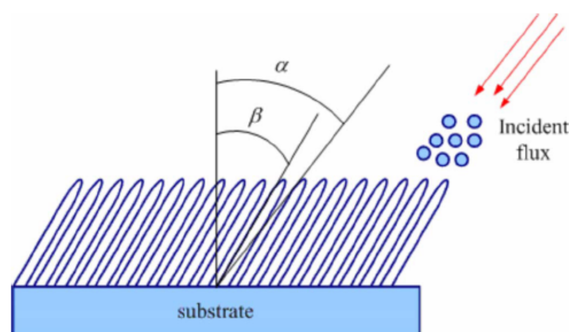

Figure 2.9: Schematic diagram of oblique-angle sputtering [87].

From the above figure it can be seen that the incident vapor flux (consisting of sputtered particles) arrives at the substrate at an oblique angle α.

In the early stages of the deposition process, randomly deposited particles cast result in shaded areas on the substrate which prevent them from contact with the incident flux. Due to the shadowing effect and limited adatom mobility, incoming sputtered particles are not able to reach the shaded areas. Instead they are deposited on the existing nucleus, resulting in inclined columnar growth. In general this angle, β, is smaller than α [88]. A SEM image of a ITO thin film deposited at α=80° and resulting β=41° is depicted below:

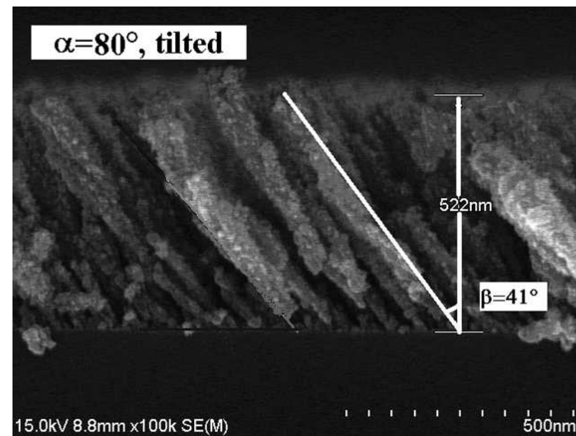

Figure 2.10: ITO deposited at α=80° and resulting β=41° [89]

Bensmaine et al. showed in their work that inclined growth of ZnO:Al could be achieved by simply installing the substrate under an angle with respect to the incoming sputtered particles. It was found that the columnar growth is highly dependent on the process parameters. Besides the use of a so-called seed layer was researched; a roughened diamond substrate was found to be able to have incident angle α and the angle resulting columnar growth β match [90].

Folkert Moll designed and produced a tilted angle substrate holder (TASH) to reproduce the work of Besmaine et al. at the PVMD group. Unfortunately tilted crystalline growth of ZnO:Al was not obtained. Application of a rough nucleation layer did also not result in an inclined growth of ZnO:Al [91].

Chapter 3

Deposition and measurement equipment

The deposition method used for ITO TCO depositions within the PVMD group, RF magnetron sputtering, as well as the deposition sequence are described in section 3.1. Post deposition material, optical and morphological characterization (sections 3.2, 3.3) was performed to determine the thin-film quality in the form of a Figure of Merit (section 3.4). Solar cells deposited with the optimized ITO TCO were measured using a J-V measurement setup (section 3.5).

3.1 RF magnetron sputtering system

The sputter deposition system used within the PVMD group is a RF magnetron sputtering system (3.1.1). The standard deposition sequence is described in section 3.1.2.

3.1.1 General layout of the deposition system

The RF magnetron sputtering system used in this work is a manually operated multi-target system by Kurt J. Lesker Company. The system is schematically displayed in Figure 3.1. The system consists of a load lock which is connected to the actual deposition chamber by means of a gate valve. Inside the process chamber torus positions are available for four 7 inch diameter targets, but only three of them are actually occupied; the ITO target on the right torus (3 o'clock), an aluminum-doped zinc oxide (AZO) target is positioned on the left torus (9 o'clock) and an old AZO target is positioned at the back (12 o'clock), the front position is vacant. The targets are separated from each other by means of vertical shields positioned in between them and a circular contamination sheet with 4 holes placed directly above the targets. A rotating shutter is positioned slightly above the

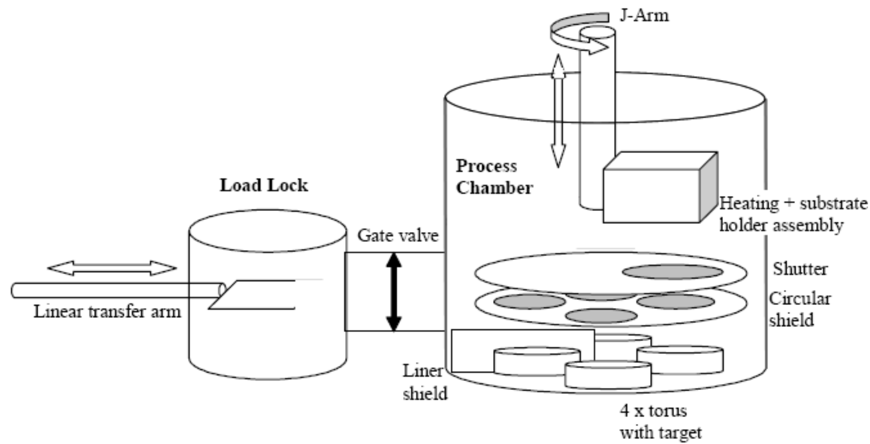

Figure 3.1: Schematic of the RF magnetron sputtering system

circular shield. The shutter is used during pre-sputtering to protect the substrate, substrate holder assembly and process chamber walls from unwanted deposition.

The substrate holder assembly is equipped with three halogen lamps for heating purposes, positioned in a closed box. The actual substrate holder is clamped against the edges of the box by means of heat resistant Nimonic springs. The temperature of the substrate holder is controlled by a 2408 Eurotherm which has a thermocouple positioned inside a metal housing which is pressed at the back of the substrate holder. A maximum controller temperature of 750 °C is allowed. It needs to be emphasized that the temperature displayed by the Eurotherm is the temperature at the back of the substrate holder, not the temperature of the substrate (holder) itself. In the past an experiment was performed to relate the substrate holder temperature to the actual substrate temperature. This has resulted in a table which is used to pick the right substrate holder temperature to achieve a desired substrate temperature.

3.1.2 Deposition sequence

A deposition sequence starts with positioning the substrate holder on the linear transfer arm and subsequent pumping down of the pressure inside the load lock. When the pressure is below 1×10^{-4} the system allows the manual opening of the gate valve. Using the linear transport arm the substrate holder is transported into the process chamber where it is transferred to the substrate holder assembly by means of a small vertical lift. The substrate holder assembly is connected to a “J” arm which is used to position the substrate holder assembly above the target. The vertical distance between the target and the substrate holder can be manually adjusted by turning a

wheel on top of the “J” arm.

When the transfer valve is closed the pressure inside the process chamber can be monitored until it stabilizes. The process flow is switched on and can be adjusted to the required value. The background pressure is controlled by means of an half automated butterfly valve; the required pressure is entered manually which is then automatically translated into the right set point for the butterfly valve. When the process gas flow and background pressure are stabilized and the operator is sure that the shutter is positioned correctly, the power, supplied by a manually operated 1.6 kW RF Hüttinger power generator, can be switched on. The default power is 150 W, increasing the power is done with steps of 30 W per minute to prevent the target from getting damaged by a sudden strong increase in power.

Although during ramping up of the power already some sputtering has been performed, so-called pre-sputtering of the target commences when the RF power has reached the desired value. Pre-sputtering of a target immediately before the deposition has three principle benefits:

- It improves the plasma stability
- It removes the top layer of the target, thereby removing possible contaminants. Especially when the process is reactive (using oxygen as sputtering gas), the target surface can oxidize. This oxide can be removed by pre-sputtering.
- It ‘passivates’ some of the chamber walls by coating them with source material

It is widely known that conditioning the target by means of pre-sputtering can improve the repeatability of depositions. A well defined duration is however not available; values ranging from 10 to 30 minutes are suggested.

The actual deposition starts with rotating the shutter shield such that the hole is located above the target. During deposition the stability of the plasma can be monitored either by looking through the porthole or by reading the values of reflected power and bias voltage from the RF generator’s display. An unstable plasma or arcing indicate accumulation of oxides on the target surface, presence of flakes of material which have fallen from the shutter, substrate holder or process chamber walls or other more process related issues such as loss of cooling water pressure or flow.

When the deposition time has elapsed the shutter shield is positioned over the target again and the power is ramped down with 80 W per 3 minutes. The “J” arm has to be returned to its upper position and should be positioned with the substrate holder facing the gate valve (9 o’clock). If the RF power has reached its default value of 150 W the RF generator can be switched off and the background pressure controller as well as the process gas controller can be switched off. The gate valve van be opened and

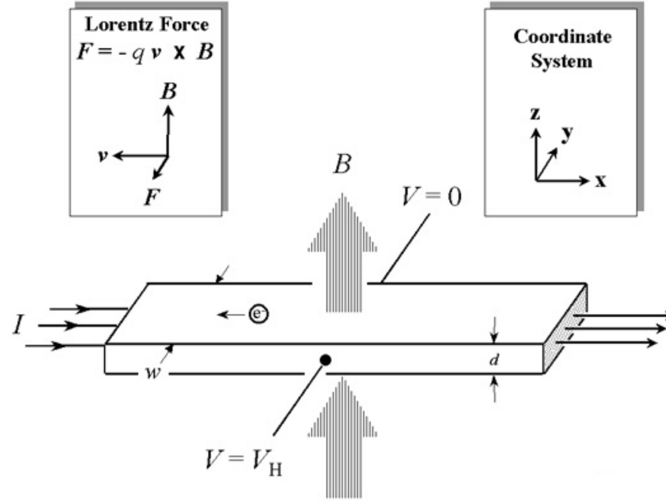

Figure 3.2: Schematic of the Hall effect [92]

the substrate is removed using the linear transfer arm, after which the gate valve can be closed again and the load lock turbo pump can be switched off as well. The substrate holder can be pressed against a water cooled plate to speed up to cooling process.

3.2 Material characterization

3.2.1 Hall effect measurement

Carrier concentration and mobility of the ITO thin films were measured using the Ecopia HMS-5000 Hall Effect setup. The principle of Hall effect measurements lies in the Lorentz force, a combination of both electric and magnetic force. Upon moving through an electric field perpendicular to an applied magnetic field, an electron will experience a magnetic force **-qV** $\times$ **B** acting normal to both directions deflecting its regular path. Due to the Lorentz force electrons are forced to move to one side of the sample, thereby creating a potential difference in the sample called the Hall voltage (V_H), see Figure 3.2. The Hall setup counterbalances the resulting Hall voltage by inducing an electric field $\mathbf{E}_H$:

$$\mathbf{E}_H = R_H \mathbf{B} \times I \tag{3.1}$$

where R_H is the Hall coefficient and I the current which is passed through the sample. The Hall coefficient is inversely related to the carrier concentration n and relates conductivity σ_H and mobility μ to each other through:

$$\mu = |R_H| \, \sigma_H = \frac{1}{n_e e} \sigma \tag{3.2}$$

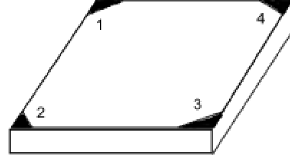

Figure 3.3: Sample with contact layout for van der Pauw measurement

A widely adopted method for obtaining both mobility μ and resistivity (sheet resistance) is the van der Pauw method [93]. In his work van der Pauw demonstrated that there are actually two characteristic resistances in a thin film, R_A and R_B, which are related to the sheet resistance R_s through the van der Pauw equation:

$$exp\left[\frac{-\pi \cdot R_A}{R_s}\right] + exp\left[\frac{-\pi \cdot R_B}{R_s}\right] = 1 \tag{3.3}$$

Considering a sample with contacts as depicted in Figure 3.3, applying a dc current I on contact 1 and 2 and measuring the consequent voltage V_{34} followed by repeating the same procedure but then by applying a current on 2 and 3, R_A and R_B can be calculated using:

$$R_A = \frac{V_{34}}{I_{12}}, R_B = \frac{V_{14}}{I_{23}} \tag{3.4}$$

Using the van der Pauw method V_H is determined by performing a series of measurements with constant current I and magnetic field **B** applied perpendicular to the plane of the sample. By forcing a current I through contacts 1 and 3, V_H can be measured across contacts 2 and 4. With the Hall voltage known, the carrier density can readily be calculated using:

$$n = \frac{IB}{q\,|V_H|} \tag{3.5}$$

3.2.2 Four point probe

Sheet resistance measurements were performed by means of an in-line four-point probe setup. The setup consists of four equally spaced metal tips connected to supporting springs to minimize sample damage during measurements. Upon contact with the sample a high impedance current source supplies a current through the outer two probes. A voltmeter is subsequently used for measuring the resulting voltage over the two inner tips. The sheet resistance is then calculated by means of the following formula:

$$R_s = \frac{\pi}{ln2} \cdot \frac{V}{I} \tag{3.6}$$

where the $\pi/ln2$ factor is on the account of the current extending [17]. When the thickness of the film is known, the resistivity (ρ) follows from:

$$\rho = R_s \cdot d \tag{3.7}$$

where d is the film thickness.

3.2.3 MiniRT setup

The Mini-RT setup is used for quick transmittance and reflectance spectra measurements at exactly the same location. White light from a halogen source is directed through optical fibers and focused on the sample which is positioned with the TCO layer facing the light source. Transmission and reflection of the light is measured with two spectrometers over a wavelength range of 375 to 1060 nm [86]. Figure 3.4 displays the schematic layout of the MiniRT setup.

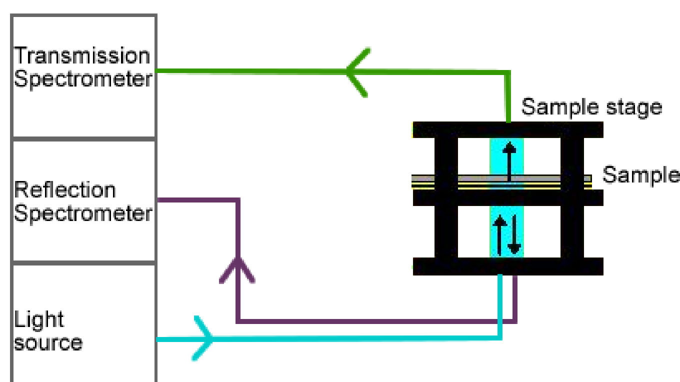

Figure 3.4: Schematic of MiniRT setup

The Mini-RT setup can also be used for thickness determination of TCO layers. Because the thickness has a strong effect on the transmittance and reflectance spectra, due to the interference pattern, model fitting of the measured values can be used to determine the thickness of a specific layer. The SCOUT software interface developed by J.A. Sap was used to determine the thickness of the ZnO:Al and ITO depositions. The SCOUT software is able to simulate transmittance and reflectance spectra according to predefined material specific parameters [94].

3.2.4 Dektak surface profiler

The ITO film thickness was measured using the Veeco Dektak 150 stylus profiler system. This system uses a stylus (12.5 μm diameter) which is

softly landed on the surface and consequently moved over a certain predetermined distance thereby measuring the variations is height. The variations in height are converted into electrical signals and used to produce a graphical representation of the surface as well as data such as average step height and surface roughness. To determine the actual deposition thickness a sharp step was created by using a 0.5 by 10 cm mask placed on top of the glass substrate during deposition. The masking was always placed at the left side of the substrate, 2.5 cm from the side. To reduce the measurement error, a mean value of 20 measurements at different locations was always taken. During the research it was found that the resolution of the surface profiler, combined with the minimal thickness of deposition, resulted in non-acurate thickness measurements after which only MiniRT (section 3.2.3) combined with the Scout model developed by J. Sap [94] was used to determine the film thickness.

3.2.5 XRD

Using X-ray diffraction (XRD) individual crystalline phases of films thicker than a few hundred Å can be identified by their characteristic diffraction patterns. Besides, the diffraction patterns provide information on orientation and size distribution of the crystallites. On the basis of XRD lies the Bragg equation which describes the condition for constructive interference for X-rays scattering from the atomic planes of a crystal. The condition for constructive interference is described by:

$$2d_s \sin(\theta) = n_d \lambda \tag{3.8}$$

where θ is the scattering angle, λ the wavelength of the incoming radiation, n_d the diffraction order and d_s the spacing between the individual planes of the crystal, as illustrated below in Figure 3.5:

The Bragg law requires that θ and λ are matched for diffraction, which may be satisfied by either varying λ or by varying the orientation of a single crystal. Polycrystalline films show a nearly continuous distribution of crystallite orientations. Diffraction will arise from those crystallites which are oriented at the right angle to satisfy the Bragg condition [95].

3.3 Optical and morphological characterization

3.3.1 Spectrophotometer

The Perkin Elmer Lambda 950 is a spectrophotometer capable of measuring Transmittance and Reflectance (T/R) spectra with high accuracy and reproducibility over a wide range of wavelengths (175 - 3300 nm). Using deuterium lamp as well as a tungsten-halogen lamp the system is capable of spanning the UV, visible and NIR region of the spectrum. This makes the

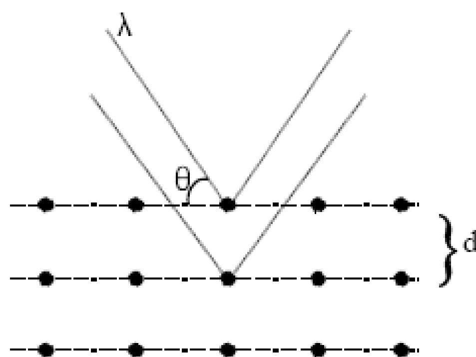

Figure 3.5: Schematic of Bragg reflection [95]

Lambda 950 especially interesting for analyzing TCOs, since not only the T/R in the UV and visible region are of interest but also the NIR region were free carrier absorption arises. Two accessories are available for the Lambda 950, the Total Integrating Sphere (TIS) and the Automated R/T Analyzer (ARTA).

Total Integrating Sphere (TIS)

The Total Intergrating Sphere (TIS) accessory is used for measuring both total and diffused transmittance and reflectance. The system consists of a 150 mm diameter integrating sphere meaning that the detector forms only a small portion of the total surface area, thereby ensuring that the light is homogeneous along the surface of the sphere before reaching the detector which increases the measurements accuracy.

The sphere is equipped with three ports; one enabling the light to enter the sphere, one directly opposite to the previous for installation of the sample for reflection measurements and one which is used during reflectance measurements to let the specular part of the light escape. For transmittance measurements the sample is placed in front of the sphere with the film deposited facing the sphere; the total transmittance is obtained by closing the remaining ports. For the diffuse transmittance the port opposite to the port from which the light enters needs to be closed. Total reflectance measurements are performed with the sample positioned at the back of the sphere, with the deposition facing the sphere and thus the incoming light. The diffuse reflectance is subsequently measured by removing the specular part port. To prevent interference during reflectance measurements an inclination of 8° is applied. Figure 3.6 schematically displays the setup of the TIS accessory when measuring T_T.

Using the total and diffuse component of transmittance and reflectance the Haze parameter can be calculated, which is a measure for the ability of

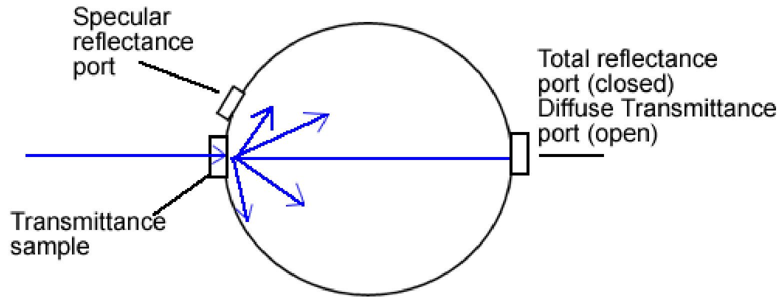

Figure 3.6: Schematic of TIS accessory

a TCO to scatter light:

$$H_T = \frac{T_{diff}}{T_{tot}} \tag{3.9}$$

$$H_R = \frac{R_{diff}}{R_{tot}} \tag{3.10}$$

Automated R/T Analyser (ARTA)

Variable Angle Spectroscopy (VAS) is a valuable technique for thin film spectral analysis since it reduces the systematic errors for spectral measurements [96]. The Automated R/T Analyzer (ARTA) accessory, developed by TNO, is used for VAS. It consists of a drum in which a detector and sample holder are both placed on separate rotation stages, allowing automatic adjustment of the angles during measurement. Whilst the sample holder can be positioned at any angle manually, the freedom of movement of the detector is limited to 15-345 degrees which prevents the blocking of incoming light. A small integrating sphere equipped with a photomultiplier (UV/Visible spectrum) and a PbS cell (NIR region) is used in the detector to enhance measurement accuracy.

For specular transmittance measurements the sample is fixed behind the detector at 180 degrees. This is necessary since Snell's law dictates that, when traveling from a layer with refractive index n through a layer stack to another layer with similar refractive index as before, the angle of transmitted light is equal to the angle of incident light. A small displacement, x_d, dependent on the thickness d of the stack is however inevitable (Figure 3.7).

Specular reflectance measurements are performed with the detector positioned at twice the angle of incident. This is done because the angle of specular reflection equals the angle of incident on the sample.

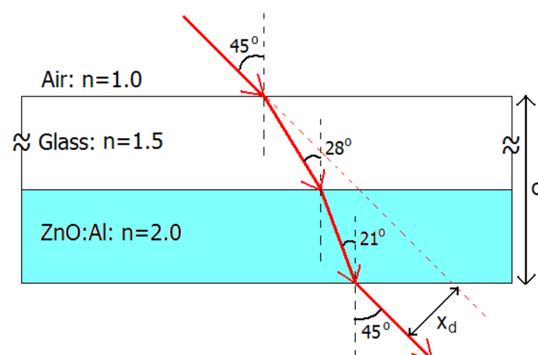

Figure 3.7: Specular transmittance through a stack of layers [94]

3.3.2 Scanning Electron Microscopy (SEM)

Scanning Electron Microscopy (SEM) is one of the methods used to optically investigate thin films when light microscopy does not provide enough detail. SEM utilizes electrons focused into a beam with very fine spot size (around 5 Å). At the objective lens pairs of scanning coils are located to deflect the beam either linearly or in raster fashion over a rectangular area of specimen surface. The electron beams have energies in the order of a few thousand eV to 50 keV. Upon impinging on the substrate, the primary electrons decelerate and loose energy to other electrons or to the lattice; resulting in electrons leaving the substrate again. These electrons can either be secondary electrons with an energy of around 5 eV, Auger electrons and elastically backscattered electrons. The most widely used method for imaging relies on the detection of secondary electrons as a function of the position of the electron beam. The observed electrons will, at low energies, only originate from a subsurface depth not larger than several $\AA$ since the average escape depth is quite small. These electrons are collected by a detector consisting of a scintillator-photomultiplier combination [61].

3.3.3 Atomic Force Microscopy (AFM)

Atomic Force Microscopy (AFM) is used whenever the resolution of SEM is insufficient and/or when the surface morphology of a sample needs to be numerically determined. The principle of AFM is based on the interatomic force of a sharp tip and the substrate surface atoms. The sharp tip is located on the end of a long cantilever with low spring constant. The tip is moved over the surface and any vertical displacement of the tip is monitored due to a displacement of the laser which is reflected by the cantilever and measured by a photodiode (Figure 3.8).

During scanning the force of the tip is kept constant by means of a piezoelectric feedback system which controls the vertical position of the sample.

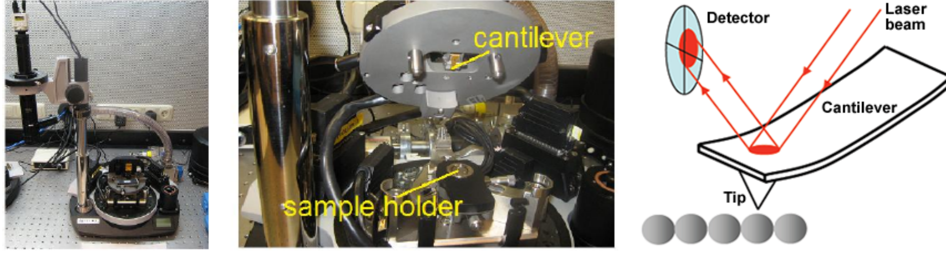

Figure 3.8: AFM setup and operating principle [97, 94]

The vertical displacement, together with the relative x- and y-coordinates, provides the information to create a three dimensional map of the surface.

Within the scope of this report only so-called semi-contact AFM scanning was used; in this operation the cantilever is driven to oscillate near its resonance frequency. The van der Waals forces will influence the amplitude of oscillation when the tip gets closer or further away from the surface, which is noticed by the system and consequently the position of the sample is corrected in vertical direction to restore the amplitude to its original value [98]

In this research an *NT-MDT NTEGRA* AFM was used for various scans with varying area and resolution. The data was analyzed using the *NT-MDT NOVA* software for obtaining both three dimensional images and root mean square surface roughness σ_{rms} of the samples, the latter being defined as:

$$\sigma_{rms} = \sqrt{\frac{1}{N}\sum_{i=1}^{N}(z_i - \tilde{z})^2} \tag{3.11}$$

with z_i equal to the ith position and $\tilde{z}$ representing the average surface level.

3.4 Figure of Merit

The optical and electrical properties of a TCO are characterized best by the electrical sheet resistance R_s and the optical transmittance T. Since these two properties are directly related, thicker films generally have a lower sheet resistance as well as a lower transmittance hence the overall performance of a TCO can be determined by means of these two properties.

A so-called Figure of Merit proposed by Fraser and Cook [99] was used from the beginning of the 1970's to qualify the overall quality of a transparent conductor (TC):

$$F_{TC} = \frac{T}{R_s} \tag{3.12}$$

Haacke [100] showed in his work that this Figure of Merit was however not very suitable. Using the relation for the sheet resistance:

$$R_s = \frac{1}{\sigma t} \tag{3.13}$$

where σ is the electrical conductivity (Ω^{-1}cm^{-1}) and t the thin film thickness in cm. The optical transmission can be expressed as a function of radiation entering (I_0) and leaving (I) a TCO:

$$T = \frac{I}{I_0} = exp(-\alpha t) \tag{3.14}$$

Combining 3.13 and 3.14 gives the following expression for the Figure of Merit:

$$F_{TC} = \sigma t exp(-\alpha t) \tag{3.15}$$

According to the above equation, a maximum thickness t_{max} can be calculated with given σ and α:

$$\frac{\partial F_{TC}}{\partial t} = \frac{\sigma exp(\alpha t) - \sigma t \alpha exp(\alpha t)}{exp(2\alpha t)} = 0 \tag{3.16}$$

$$t_{max} = \frac{1}{\alpha} \tag{3.17}$$

Substituting this result into equation 3.13 yields the maximum transmission at maximum F_{TC}:

$$T = \frac{1}{e} = 0.37 \tag{3.18}$$

The above equation clearly illustrates the inefficiency of the Figure of Merit as proposed by Fraser and Cook since the maximum F_{TC} occurs at a film thickness which reduces the optical transmission to 37% which is absolutely too low for a good TCO.

Haacke therefore searched for a better balance between transmission and sheet resistance, starting by redefining the Figure of Merit:

$$\Phi_{TC} = \frac{T^x}{R_s} \tag{3.19}$$

where x >1. In line with the sequence followed above, the maximum film thickness now follows from:

$$t_{max} = \frac{1}{x\alpha} \tag{3.20}$$

Several values for x were researched, but $x = 10$ turned out to provide the most favorable choice, resulting in a new Figure of Merit:

$$\Phi_{TC} = \frac{T^{10}}{R_s} = \sigma\ t\ exp(-10\alpha t) \tag{3.21}$$

This Figure of Merit is used in this work to discriminate between the different depositions. However, bearing in mind the different wavelength ranges the aSi:H, μSi:H and HIT solar cells operate, this Figure of Merit cannot be applied to the transmission data retrieved from TIS measurements. The Φ_{TC} as proposed by Haacke was therefore, within the scope of this work, divided into three separate versions, each dedicated to a specific type of solar cell:

- Φ^{a}_{TC} for aSi:H solar cells where the average transmittance T_{avg} is calculated between 300 and 750 nm
- $\Phi^{\mu c}_{TC}$ for μcSi:H solar cells where the average transmittance T_{avg} is calculated between 600 and 1100 nm
- Φ^{HIT}_{TC} for HIT solar cells where the average transmittance T_{avg} is calculated between 400 and 1100 nm

3.5 Solar cell characterization

The main parameters characterizing the performance of a solar cell are the short-circuit current density, J_{sc}, open-circuit voltage, V_{oc} and the fill factor FF. The short-current density is the current that runs through the external circuit when the electrodes are short circuited. Ideally, the short-circuit density is equal to the photo-generated current density J_{ph}. The open-circuit voltage is the voltage at which no current is running through the external circuit, as a consequence the dark current compensates the photo-current. The open-circuit voltage is described by the following relation:

$$V_{oc} = \frac{kT}{q} \ln\left(\frac{J_{ph}}{J_0} + 1\right) \tag{3.22}$$

where k is the Boltzmann constant, T is the temperature, q is the elementary charge, J_{ph} the photo-generated current and J_0 the saturation current density.

The fill factor is the ratio between the maximum power that can be delivered by a solar cell ($P_m = V_{mp} \times J_{mp}$) and the product of J_{sc} and V_{oc}:

$$FF = \frac{J_{mp}V_{mp}}{J_{sc}V_{oc}} \tag{3.23}$$

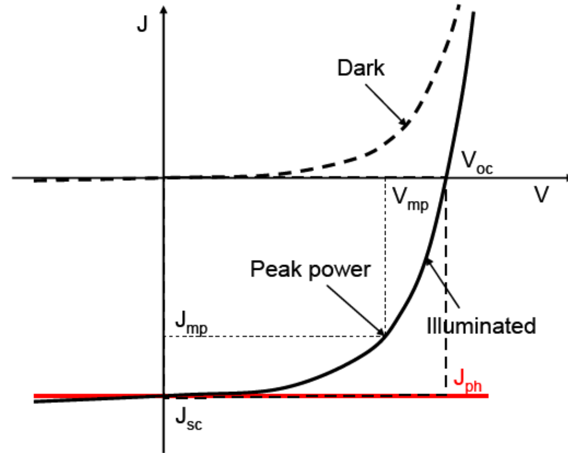

Figure 3.9: J-V characteristics of a p-n junction in the dark and under illumination [10]

The above mentioned characteristic solar cell parameters are visualized in the figure below:

The conversion efficiency, η, of the solar cell is subsequently calculated by dividing the generated maximum power by the incident power, P_{in}:

$$\eta = \frac{P_m}{P_{in}} = \frac{J_{mp}V_{mp}}{P_{in}} = \frac{J_{sc}V_{oc}FF}{P_{in}} \tag{3.24}$$

These parameters were measured with a semi-automated illuminated J-V setup which mimics the AM1.5 spectrum, providing a P_{in} of 1000 W/m^2 on a 4 $\times$ 4 cm^2 area.

Chapter 4

RF magnetron sputtered ITO

4.1 Introduction

In this chapter six deposition parameters are varied to obtain the optimal value for the deposition process in general and the different types of thin-film solar cells in particular. In an first attempt to optimize the deposition process the substrate temperature was varied (section 4.3.1), followed by a RF power series (section 4.3.2), background pressure series (section 4.3.3), oxygen partial pressure series (section 4.3.4), target-to-substrate series (4.3.5) and finally a deposition time (thickness) series (section 4.3.6).

During the optimization process a repeatability and recovery study was performed on the ITO target, aimed at optimizing the pre-sputter time prior to deposition and post-ventilation conditioning sputtering. The results of this study are given in section 4.3.8 and 4.3.8.

The improvement of optical and electrical properties by means of post-deposition annealing was studied (section 4.3.9), as well as texturing of ITO by means of etching (section 4.3.10). Inclined growth of ITO by means of the tilted angle substrate holder is described in section 4.3.11.

4.2 Experimental

All depositions were done on 10×10 cm^2 Corning Eagle 2000 glass. Before deposition the glass substrate was ultrasonically cleaned for 10 minutes in an acetone bath followed by 10 minutes in an isopropyl alcohol (IPA) bath, after which the substrates were blown dry with a nitrogen gun.

Each series of depositions commenced with 30 minutes pre-sputtering of the target in the deposition conditions used for the subsequent deposition. After the initial deposition a pre-sputtering time of 15 minutes was used.

During pre-sputtering the substrates were heated to the desired substrate temperature.

After each series of depositions the structural, optical and electrical properties of the ITO TCOs was determined. The main equipment which was used was the four-point probe, Total Integrating Sphere, MiniRT setup and Hall setup. The optical and electrical measurements were used to determine the Figure's of Merit for each of the depositions. Each series was subsequently evaluated on basis of it's Figure of Merit, the deposition parameters of the following deposition runs was eventually adjusted in order to increase the overall quality with time. Occasionally other measurement equipment, such as AFM, SEM or XRD, was used to gain more insight in certain structural or morphological properties.

For each of the 6 deposition parameter runs the as-deposited thickness (bins) and consequent deposition rate (symbols) are plotted, as well as the transmittance spectra. The thickness is provided with error bars. Standard deviation for the deposition rates are calculated by using the relation for error propagation, they are however not displayed in the figure since they coincide with the error bars of the thickness series.

Sheet resistance measurement are used in combination with the thickness measurement to calculate the resistivity. Standard deviations are calculated, error bars are however not displayed for both sheet resistance and resistivity since they would coincide due to the different scaled y-axis.

Carrier concentration and mobility resulting from Hall measurement are also displayed for each series. Error bars were not calculated since only one sample per any deposition run was used for Hall measurement.

4.3 Results and discussion

4.3.1 Temperature series

The substrate temperature was varied from room temperature (RT) to a maximum of 180 °C, with equal steps of 30°C starting from 90°C. The difference between RT and the following deposition at 90°C is due to the temperature controller; between RT and 90°C the temperature cannot be controlled. The maximum temperature is limited for device reasons; a temperature higher than 180 °C could inflict damage to substrate solar cells (n-i-p devices) where the TCO is deposited onto the already grown solar cell.

The remaining deposition parameters, such as target-to-substrate distance and sputter pressure, were chosen on basis of the experience of both technical and scientific staff with AZO depositions. A complete overview of deposition parameters is given in Table A.1 in Appendix A.

Structural

Thickness measurements show a steadily increasing thickness with increasing temperature (Figure 4.1 [A]), error bars show the standard deviation. The thickness for the RT deposition is 150.1 ± 10.2 nm whereas the thickness of the deposition done at 180 °C is 178.8 ± 9.9. The deposition rate is increased from 8.3 to 9.9 nm/min.

As suggested by Meng and Dos Santos it appears that heating of the substrate results in heating of the plasma and the target material as well. The elevated temperature increases the active energy of the low melting point atoms on the target surface which increases the sputtering yield and subsequently the deposition rate [74].

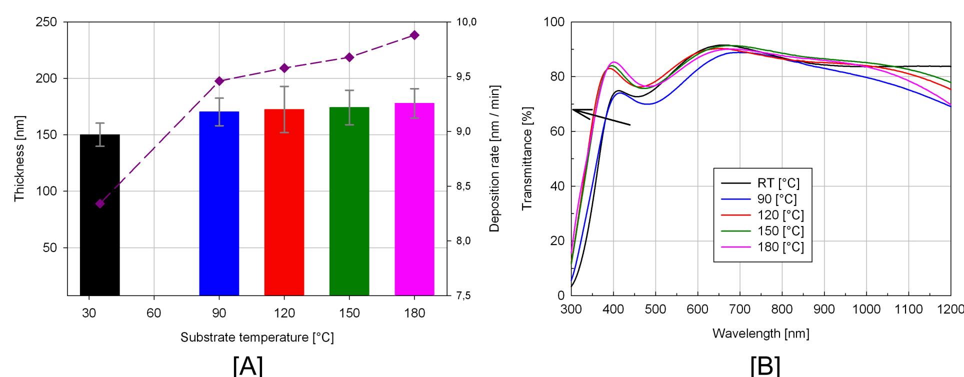

Figure 4.1: Temperature series thickness (bins) and deposition rate (symbols) [A], transmittance spectra [B]

Optical

Transmittance curves of the as-deposited temperature series show a clear blue-shift in the ultraviolet region (Burstein-Moss shift) as well as decrease in NIR transmittance with temperature (Figure 4.1 [B]). The RT deposition shows however a divergent behavior, especially in the NIR region the transmittance in the 'tail' is higher than all others. It also appears that the RT deposition is spectrally the same as the 90°C deposition, it only shows more extremes. It needs to be noted that the 90 °C deposition has the lowest transmittance in the NIR region, this is quite remarkable and could indicate either a system or user error during deposition or an user error during measurement.

Within the transmittance spectra, particularly in the wavelength range <450 nm, two groups can be identified: one group consisting of the RT and 90 °C depositions and another group consisting of the 120, 150 and 180 °C depositions. The latter group shows a distinct shift of the fundamental absorption region towards lower wavelength (higher energy). A possible

explanation for this Burstein-Moss shift could be an improved crystallinity, XRD measurements could possibly provide more information in this case. The reduced transmittance in the NIR region suggest an increase in carrier concentration since the reduced transmittance in this region is a consequence of free carrier absorption. The carrier concentration resulting from the Hall measurement is however indecisive in this matter.

Electrical

The sheet resistance at RT and 90 °C is comparable, but due to the increased thickness of the 90 °C the resulting resistivity is higher. Further increasing the temperature reduces the sheet resistance and resistivity notable. The decrease in resistivity with increasing temperature is generally associated with the effect of thermally induced crystallization; it is reported that amorphous ITO films crystallize with annealing temperatures above 150 °C. However, it is also reported that the decrease of resistivity is caused by the fact that the ITO shows better crystallinity with larger gain sizes and reduced grain boundary scattering [101]. In the latter case the ITO would already be crystallized, independent of annealing. In section 4.3.9 this assumption is confirmed. It would however be interesting to have a temperature series of depositions measured by X-ray diffraction.

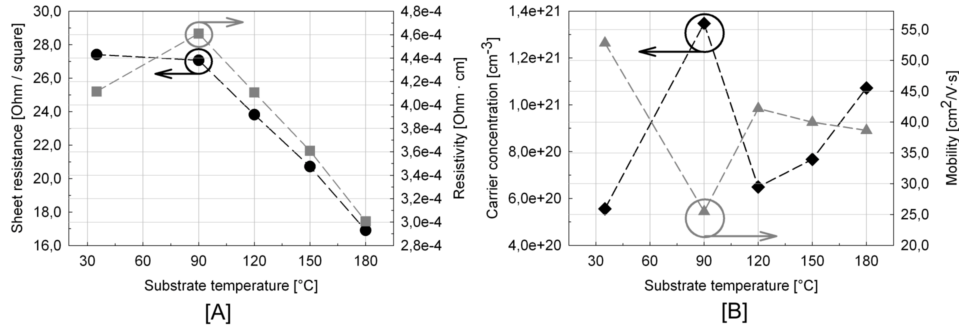

Figure 4.2: Temperature series thickness (bins) and deposition rate (symbols) [A], carrier concentration and mobility [B]

The carrier concentration and mobility, resulting from the Hall measurement, do not show a clear trend which is mainly caused by the 90 °C deposition. Removing this deposition from the figure results in a more parabolic character of both carrier concentration and mobility, showing an increase in mobility and a small decrease in carrier concentration. This is quite remarkable since an increase in carrier concentration with increasing temperature would be expected. Meng et al. [74] related this increase in carrier concentration with substrate temperature not only to an increase in oxygen vacancies, but also to the fact that more tin atoms diffuse from the grain

boundaries and interstitial lattice locations to regular In_2O_3 lattice locations. An increase in carrier mobility could be related to an increased grain growth at higher substrate temperatures resulting in less grain boundary scattering [101]. The deviations in measured carrier concentration and mobility could be due to the size and location of the samples used for the Hall measurement.

Figure of Merit

The Φ_{TC} for the temperature series are displayed in Figure 4.3. Not surprisingly the highest Φ_{TC} for all three types of solar cells is achieved at a deposition temperature of 180 °C. In line with was observed above, the optical and electrical behavior of the 90 °C deposition result in the lowest Φ_{TC}. The maximum Φ_{TC} was obtained for the deposition done at 180 °C and with an averaged transmittance taken over the 600 - 1100 nm wavelength range thereby resulting in $\Phi_{TC}^{\mu c}$ of 13.4 × 10^{-3}. This value is comparable to values found in literature [87, 102, 75].

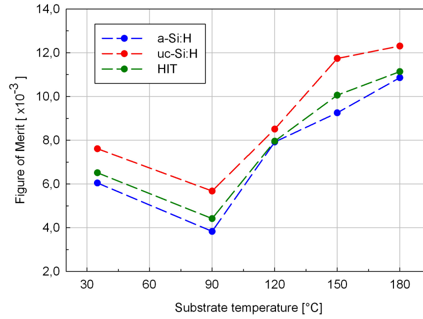

Figure 4.3: Temperature series Figure of Merit

4.3.2 Power series

Although the highest Φ_{TC} for all three types of solar cells was the highest for a substrate temperature of 180 °C, it was decided to use a substrate temperature of 150 °C for all following deposition runs. This substrate temperature was chosen to ensure that no damage would be inflicted by an ITO deposition on top of an already deposited solar cell (i.e. n-i-p or HIT solar cells).

Four depositions with sputtering power varying from 200 to 350 Watt were done to verify the effects of increasing sputtering power. The deposition time used for the temperature series is elongated to 30 minutes. The remaining deposition parameters were kept constant during deposition, see Table A.2 in Appendix A.

Structural

As the RF power is increased, the energy acquired by the sputtering inert Ar+ ions which are colliding on the target increases as well, resulting in an increase of energy of the sputtered atoms [103]. Besides, an increase in RF power increases the self-bias of the target, causing an increase in the density of sputtered neutrals and their average energy which results in a higher deposition rate [79].

The increase in deposition rate with RF power is also clearly visible for the power series done within the scope of this project (Figure 4.4 [A]). The error bars for the thickness show a minimum for the depositions done at 250 and 300 Watt, indicating that these depositions are more uniform than the other. The deposition rate appeared to increase linearly with increasing RF power. Linear fitting of the deposition rate shows that the deposition rate increases with 0.4 Å/min per Watt.

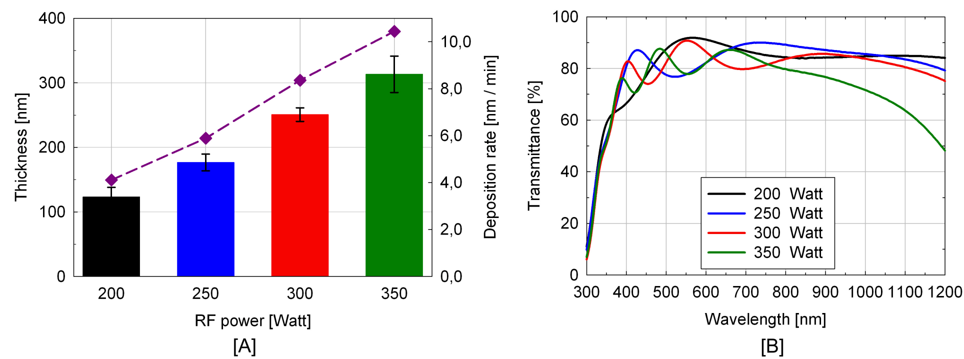

Figure 4.4: Power series thickness (bins) and deposition rate (symbols) [A], transmittance spectra [B]

Optical

The power series optical transmittance is displayed in Figure 4.4 [B]. A clear increase in the number of interference fringes with increasing sputtering power is visible, indicating an increase in film thickness. The 350 Watt deposition shows a significantly lower transmittance for wavelengths >750 nm. A possible explanation for this decrease in transmittance can be an increase in carrier concentration, as described by Terzini et al. [69]. This assumption is confirmed by Hall measurements (Figure 4.5), although it needs to be mentioned that additional depositions with a power of 325 or 375 Watt could possibly be more decisive in this matter. In contrast to what is observed in literature [69, 103], there is no shift to higher wavelengths (lower power) in ultraviolet transmittance visible with increasing RF power.

Electrical

The increased energy of the sputtered particles due to the increased RF power makes it for the sputtered particles possible to knock out oxygen atoms from the deposition, thereby reducing the oxygen content and strongly increasing the carrier concentration. On the other hand, an increase in oxygen vacancies also enhances the scattering of the charge carriers thereby reducing the mobility with increasing sputtering power [80].

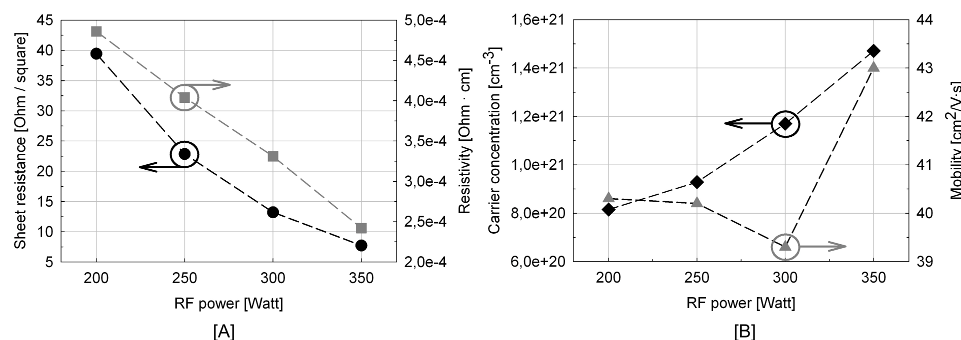

Figure 4.5: Power series sheet resistance and resistivity [A], carrier concentration and mobility [B]

Sheet resistance decreases significantly (factor 5) with increasing sputter power, mainly caused by a steady increase in both carrier concentration and mobility. The resistivity of the depositions is halved when the 200 Watt deposition is compared to the 350 Watt deposition (Figure 4.5). Leaving the somewhat deviating mobility of the 300 Watt deposition out of consideration reveals a similar, almost parabolic, behavior of the carrier concentration and mobility. In contrast to the observation of Wu and Chiou [80] a steep increase in mobility is visible with increasing the RF power from 300 to 350 Watt. It is not clear how this is possible.

The achieved values for resistivity are comparable to what is mentioned in literature [69, 103, 104, 80]. This makes the optical behavior of the depositions even more interesting since it was observed by Panicker and Essinger [71] that a high RF power produces strongly oxygen deficient films with low resistivity as well as a reduced optical transmittance.

Figure of Merit

The Figures of Merit are calculated for the different types of solar cells are displayed in Figure 4.6. It is interesting to observe that where the 350 Watt deposition offers the highest quality for the a-SI:H solar cells, where this is the 300 Watt deposition for both μc-Si:H and Hit solar cell. This outcome illustrates the negative effect of the increased carrier concentration; although the conductivity is increased by a factor two, the transmittance is lowered

such that the overall quality of the thin-film with the highest conductivity does not have the optimal combination of optoelectronic characteristics for μc-Si:H and Hit solar cells.

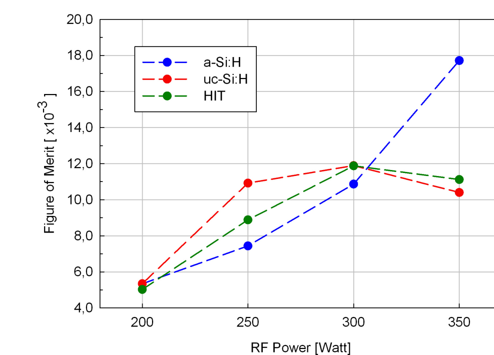

Figure 4.6: Power series Figure of Merit

4.3.3 Pressure series

Based on the outcome of the power series depositions a RF power of 300 Watt was decided to be the standard for the following deposition runs. As explained in the previous section, the substrate temperature was decided to be maintained at 150 °C. Within the pressure series the sputter pressure was varied from 2.6 to 20 μbar, with equal steps of 5 μbar from 5 μbar. The deposition parameters for this pressure series are presented in Table A.3 in Appendix A.

Structural

The deposition rate decreases with increasing background pressure due to sputtered particles which undergo more collisions on their path to the substrate. It appears however that the change in deposition rate levels from a pressure of 15 μbar, another deposition at a pressure of, for example, 25 μbar could give a decisive answer. It has been observed by both Mohammadi Gheidari et al. and Kavei et al. [105, 106] that, at relative high pressure levels, the deposition rate actually increased up to a certain level after which it sharply decreased again. The used pressures were all above the maximum pressure used in this work, but it could be interesting to verify the work of Mohammadi Gheidari by depositing another pressure series at higher pressure. Figure 4.7 [A] displays the thickness (bins) and deposition rate (symbols) of the various depositions.

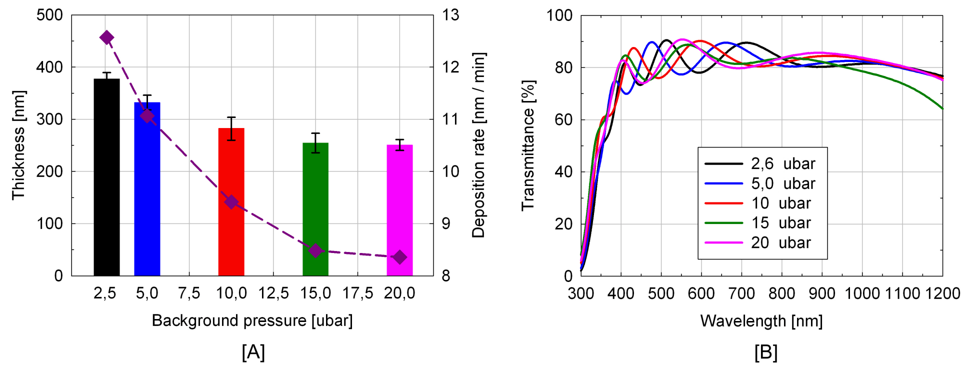

Figure 4.7: Pressure series thickness (bins) and deposition rate (symbols) [A], transmittance [B]

Optical

Total transmittance spectra for the five pressure series samples are depicted in Figure 4.4 [B]. There is a clear increase in interference spectra visible, indicating an increase in thickness with decreasing pressure. This is an obvious result following the fact that an increase in pressure will increase the number of collisions sputtered particles undergo on their way to the substrate and thereby decreasing the deposition rate. The deposition done at 15 μbar displays a remarkably lower transmittance in the NIR region. It is not quite clear what the reason is for this deviating behavior. It needs to be mentioned that the respective deposition was done on a different day than the other 4 depositions. It could be that there was a minor problem with the deposition system which was not noticed, or the user could mistakenly have done the deposition with slightly different parameters.

Zebaze Kana et al. [107] reported low transmittance and a dark or brownish appearance, related to the common expectation that a better vacuum level results in a higher transmittance of the deposited ITO films. This was not observed for the pressure series of depositions done within this research; the average transmittance over the complete spectrum as well as the transmittance over the specific wavelength ranges for the different types of solar cells was quite constant.

Electrical

The electrical parameters, Figure 4.8 [A,B], show that the sheet resistance of the depositions is at first concentrated around a value of 8.5 $\Omega/\Box$. The 20 μbar deposition shows however a strong increase in sheet resistance. The resistivity, as calculated from the sheet resistance and MiniRT thickness measurement, is quite varying; at low pressure the resistivity is high, but approaching a deposition pressure of 15 μbar the resistivity decreases. From

15 μbar the resistivity increases however again to reach almost the initial value of the 2.6 μbar deposition.

Different observations concerning the variation of resistivity with increasing background pressure have been encountered in literature. Whereas Lee et al. [101] report a decreasing resistivity with increasing sputter pressure, the observations of Zebaze Kana et al. [107] are more in line with the behavior of the resistivity observed in this work.

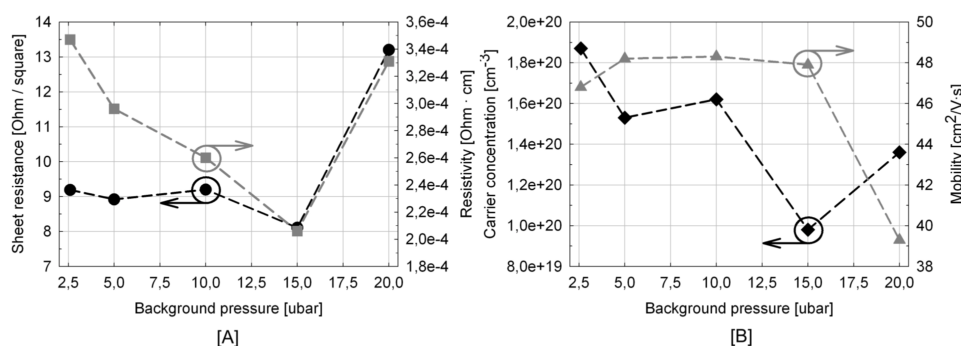

Figure 4.8: Pressure series sheet resistance and resistivity [A], carrier concentration and mobility [B]

The Hall measurements show a competing behavior of carrier concentration and mobility. The mobility seems to be more consistent until a deposition pressure of 15 μbar, after which it shows a sharp decrease. The carrier concentration is more fluctuating, this behavior was also observed by Zebaze Kana et al. although it needs to be mentioned that the pressure in their work was varied on a much larger scale.

Figure of Merit

Interpretation of the above mentioned optical and electrical measurements by means of the Figure of Merit shows that, mainly for a-SiH solar cells, the 15 μbar deposition is indeed behaving interestingly; it is clearly deviating from the 'expected' path. The most obvious reason for the high Figure of Merit is of course the low resistivity, but looking more carefully at the transmittance spectrum reveals that it seems to be slightly more blue-shifted than the other spectra. The low resistivity, high transmittance in ultraviolet and visible region, combined with the remarkably lower transmittance in the NIR region do suggest that the 15 μbar must have a significantly higher carrier concentration. For all three types of solar cells the Φ_{TC} was comparable or higher than the values encountered in literature [107].

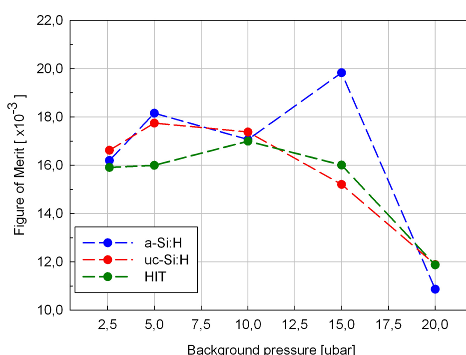

Figure 4.9: Pressure series Figure of Merit

4.3.4 Oxygen partial pressure series

From the pressure series it became clear that for a-Si:H, μc-Si:H and HIT solar cells the optimal Φ_{TC} was achieved for a background pressure of 15, 5 and 10 μbar respectively. Since this outcome does not provide a clear indication for which background pressure to use, it was decided to use the background pressure with the highest Φ_{TC}, calculated with the transmittance averaged over the complete wavelength range of 300 to 1200 nm, for future deposition runs.

The effects of oxygen pressure in the sputtering ambient on the optical and electrical properties of the RF magnetron sputtered ITO were studied by depositing a series of 5 thin films with varying oxygen content. The oxygen content was varied between 0 and 1% by using both the Argon gas feed line and the Ar + 1%O_2 gas feed line. After an initial series of test depositions the deposition time was varied such that the resulting thicknesses of the depositions would be the same. The remaining deposition parameters can be found in the Appendices (Apendix A.4).

Structural

In contrast to what was observed in literature [84], introducing oxygen in the process chamber during deposition reduced the deposition rate, although the variations are within a range of 1 nm / min (Figure 4.10 [A]).

Optical

A significant increase in optical transmittance in the NIR region is visible (Figure 4.10 [B]), which is in line with observations in literature [80, 84, 85]. In general this increase in NIR region transmittance is subscribed to a decrease in carrier concentration with increasing oxygen content due to a sharp reduction in oxygen vacancies [82, 84]. The overall spectral behavior of the transmittance curves is quite constant, indicating that the thicknesses

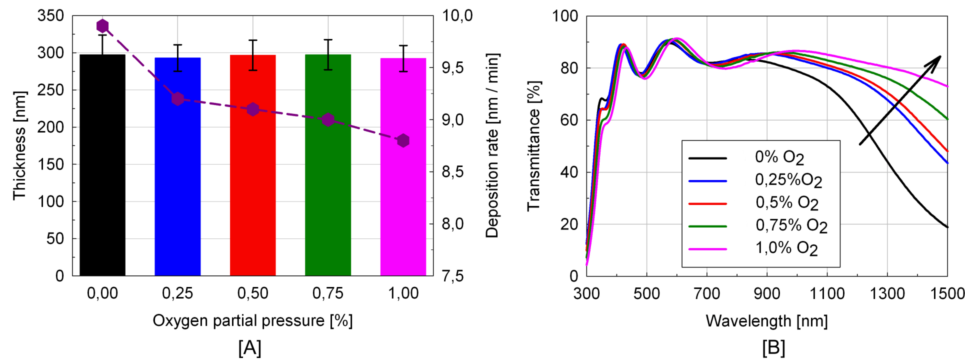

Figure 4.10: Oxygen partial pressure series thickness (bins) and deposition rate (symbols) [A], transmittance [B]

are indeed comparable. There seems to be a slight shift of the band edge to longer wavelengths with increasing oxygen pressure. This shift can be explained by using the Burstein-Moss shift, where a shift of the band edge to higher wavelengths is related to a decrease in carrier concentration (section 2.2.3).

Electrical

The effect of oxygen incorporation on the electrical properties of the ITO is very clear: both carrier concentration and mobility are decreased significantly resulting in a higher resistivity and sheet resistance. A clear drop in both carrier concentration and mobility confirms this observation (Figure 4.11 [A] and [B]).

In literature an initial increase in mobility, attributed to reduced grain boundary scattering resulting from larger grain sizes, and consequent drop in resistivity is reported by multiple authors [84, 85]. The subsequent increase of resistivity was attributed to a decrease in mobility caused by a trapping effect of neutral $(SnO_2)_2$ with increasing oxygen content [80].

Figure of Merit

Since it was shown that adding oxygen to the sputtering gas improves the NIR region transmittance, sputtering with oxygen might be beneficial for μc-Si:H and HIT solar cells. The steep increase in resistivity results however in decreasing Figures of Merit with increasing oxygen partial pressure 4.12. In contrast to what is generally found in literature, the highest quality ITO is achieved without the addition of oxygen during sputtering.

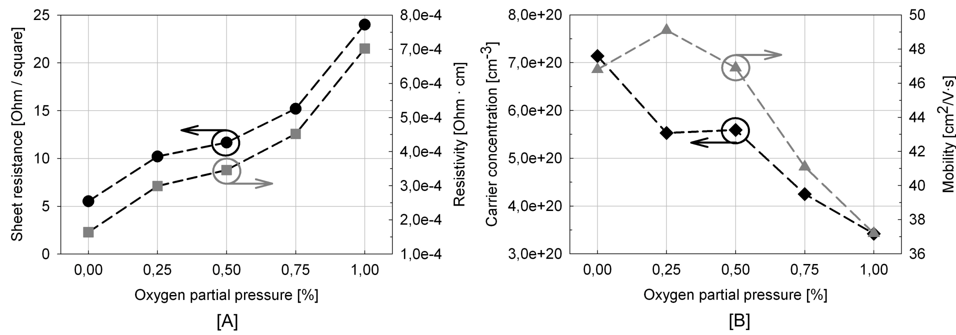

Figure 4.11: Oxgyen partial pressure series sheet resistance and resistivity [A], carrier concentration and mobility [B]

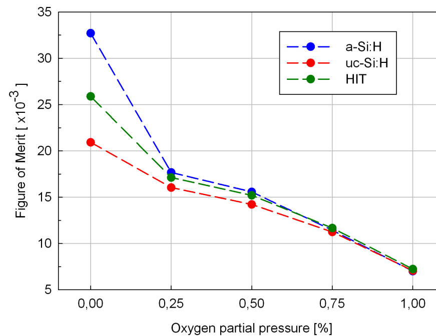

Figure 4.12: Oxygen partial pressure Figure of Merit

4.3.5 Target-to-substrate series

The oxygen partial pressure series clearly showed that, for all three types of solar cells made within the PVMD group, it is not beneficial to sputter with a certain percentage of oxygen; subsequent depositions were therefore done without the addition of oxygen.

The target-to-substrate distance was varied from its absolute maximum (165 mm) to its absolute minimum (65 mm), with equal steps of 25 millimeter. The remaining process parameters were kept constant during the deposition series. For reference purpose a sample made at the standard target-to-substrate distance of 110 mm is included as well. The deposition parameters can be found in Table A.5 in Appendix A.

Structural

The deposition rate decreases with increasing target-to-substrate distance; there seems to be an almost linear relation between the deposition rate and target-to-substrate distance (Figure 4.13 [A]). This is quite remarkable

since other authors have observed a bi-partial development of the deposition rate [80, 79]. Nyaiesh described the existence of a 'virtual source' at a distance the thermalization distance h (see section 2.3.5) from the target, between the target and the virtual source the deposition rate was found to be constant whilst the deposition rate decreased almost linearly between the virtual source to the substrate [108]. This suggests that, for this series of deposition, the virtual source is located somewhere between the target and the smallest possible target-to-substrate distance of 65 mm.

The deposition rate appears to decrease linearly with increasing target-to-substrate distance; linear fitting revealed a decrease in deposition rate of 0.9 Å/min with every millimeter.

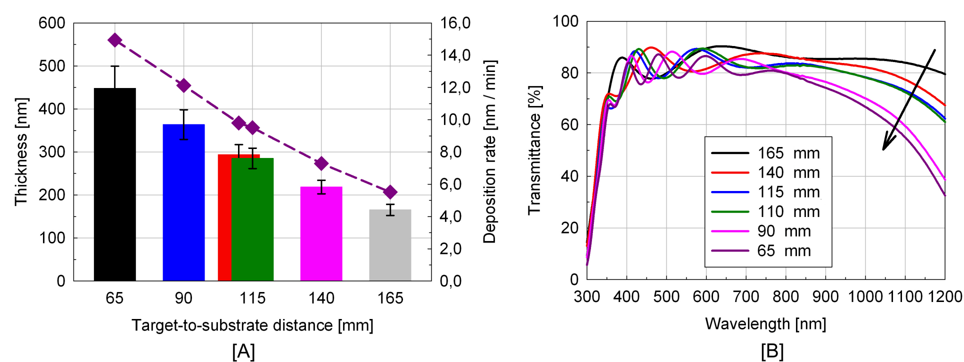

Figure 4.13: Target-to-substrate series thickness (bins) and deposition rate (symbols) [A], transmittance [B]

The thickness distribution of the 165, 115 and 65 millimeter target-to-substrate distance is plotted in both top-view and three-dimensional to allow comparison of uniformity (Figure 4.16, page 63). It appears that there is no real change in uniformity with changing target-to-substrate distance, all samples show a large variation in center and end thickness although it appears that the area with the thickest layer in the center of the deposition is somewhat smaller for the deposition done at 65 [mm] than for the ones done at 115 and 165 [mm]. It would be interesting to do a similar series of depositions but then with the donut-shield (section 2.3.5) installed to allow comparison with the work of Franken who described a change of thickness profile of with increasing target-to-substrate height from concave to convex [86].

Optical

The optical spectra (Figure 4.13 [B])show more interference fringes and lower NIR transmittance with decreasing target-to-substrate distance, which is the typical behavior for films with increasing thickness (see also section 4.3.6). There are no strikingly different spectra.

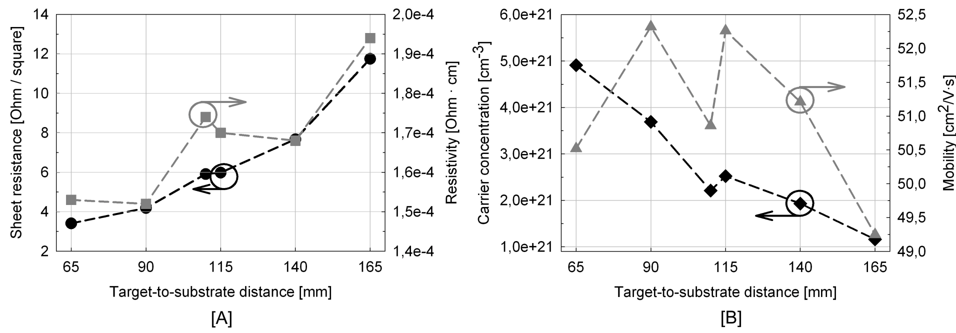

Figure 4.14: Target-to-subtrate series sheet resistance and resistivity [A], carrier concentration and mobility [B]

Electrical

The effect of decreasing the target-to-substrate distance is quite substantial: the sheet resistance drops with more than 70% from 11.75 Ω/□ at 165 mm to 3.41 Ω/□ at 65 mm (Figure 4.14). The Hall measurements indicate that this decrease is related to a strong increase in carrier concentration. The mobility does not seem to vary much with target-to-substrate distance, this appears to indicate that there is no structural change in the ITO. The deposition done at a target-to-substrate distance of 110 millimeter is from a sheet resistance point of view not deviating, but looking at the resistivity as calculated from the sheet resistance and thickness the sample is interesting since it does not follow the general trend. This is confirmed by the Hall measurements where the values of the 110 mm deposition are also deviating. The behavior of this sample could be due to the fact that this deposition was not part of the actual target-to-substrate series, it was deposited at a different time; the deposition circumstances and system condition could be such that the resulting resistivy deviates from the others.

In the work of Antony et al. [109] a similar trend in increasing resistivity with increasing target-to-substrate distance was observed. The mobility however displayed a very distinct decrease, a similar sharp decrease in mobility cannot be seen in Figure 4.14 [B]. It was concluded by Antony et al. that at greater target-to-substrate distance the crystallinity of the films was reduced, resulting in smaller grain sizes. Grain boundary scattering of carriers is consequently increased thereby reducing the mobility of the films, hence the resistivity is increased.

Figure of Merit

The interesting electrical behavior of the 110 mm deposition is not translated into an obvious deviating Figure of Merit. When comparing the Figure of Merit of the smallest and largest target-to-substrate distance it is worth

nothing that whereas for the a-Si:H and μc-Si:H solar cells the Figure of Merit is decreasing with increasing target-to-substrate distance. the Figure of Merit for HIT solar cells is increased.

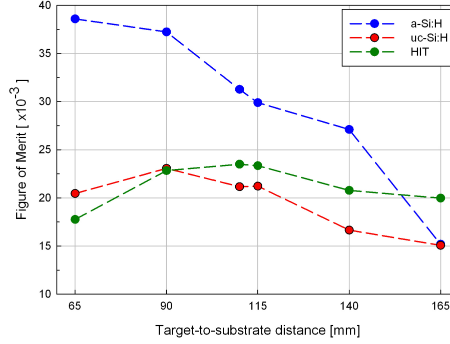

Figure 4.15: Target-to-substrate series Figure of Merit

4.3.6 Deposition time series

A target-to-substrate distance of 110 millimeter was kept since the Figure of Merit, with transmittance averaged over the complete spectrum (300 - 1200 nm), obtained it's highest value at this distance. Besides, the other Figures of Merit, Φ^{a}_{TC}, $\Phi^{\mu c}_{TC}$ and Φ^{HIT}_{TC}, did not show a shared maximum Φ_{TC} at a single target-to-substrate distance.

The deposition duration was varied from 10 to 50 minutes with equal steps of 10 minutes. To further investigate the structural effect of increasing film thickness the depositions were send to the University of West Bohemia in Plzeň, Czech Republic, for XRD analysis. The deposition parameters are summarized in Table A.6.

Structural

The thickness increases linearly with increasing deposition time although the deposition rate is found to vary slightly (Figure 4.17 [A]). The slight variations in deposition rate could be due to user error during measurement or small variations is deposition parameters. Repeatability of depositions is described in more detail in section 4.21.

The crystallographic structure of the deposition time series was analyzed by X-ray diffraction, the resulting XRD spectra are shown in Figure 4.18. The thinnest deposition shows low intensity diffraction peaks corresponding to early stage crystallization of the ITO in the (211), (222) and (440) orientation. With increasing thickness the (440), (211), (400), (431) and (622) peaks become considerably more intense, other minor peaks also increase in intensity with increasing thickness. The (222) peak seems to differ with

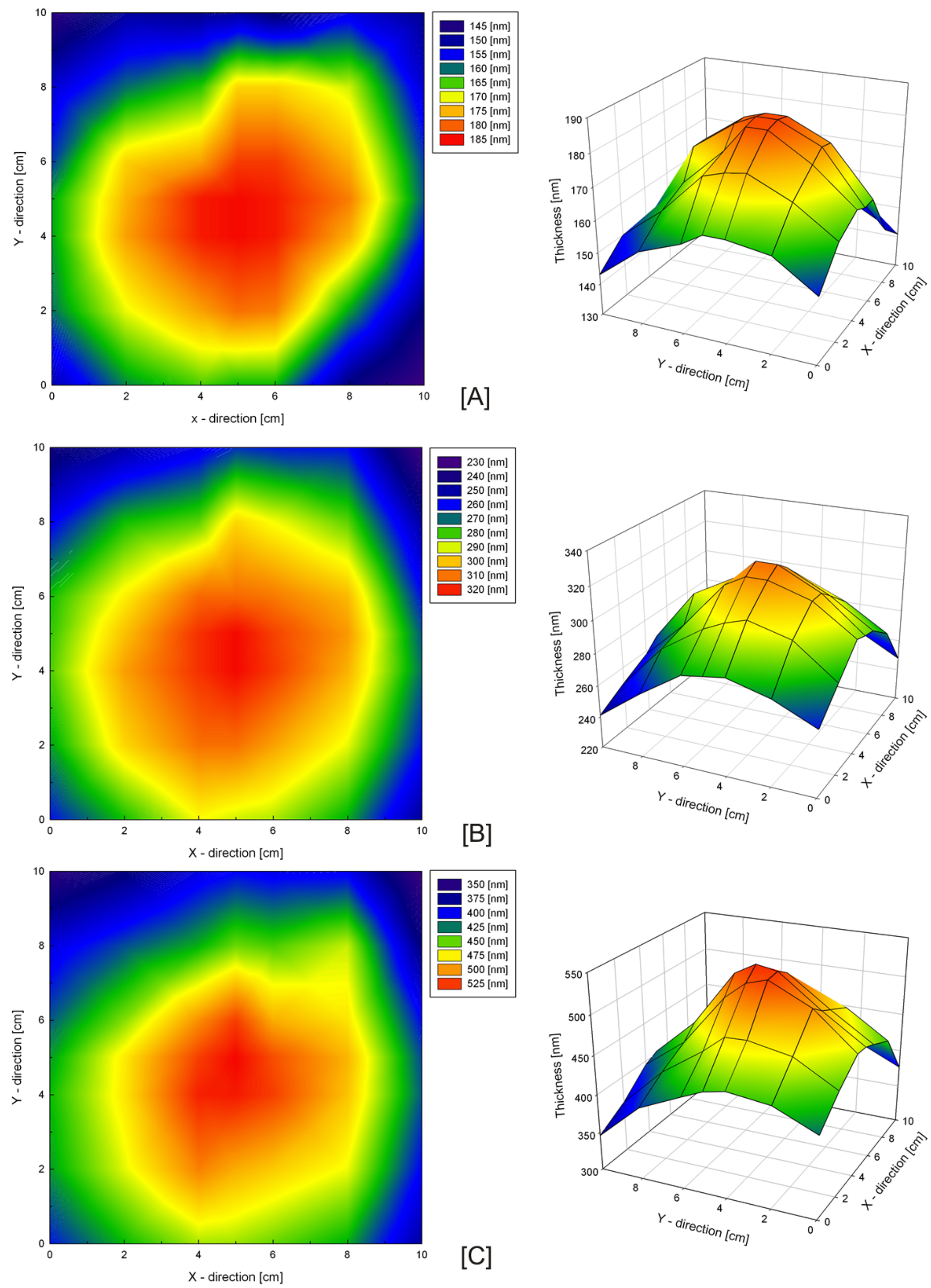

Figure 4.16: Top and 3-dimensional view of depositions done at 165 mm [A], 115 mm [B] and 65 mm [C]

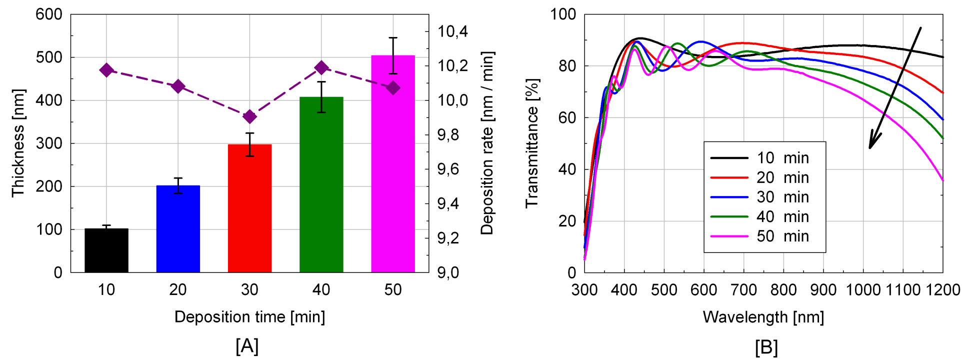

Figure 4.17: Deposition time series thickness and deposition rate [A] and transmittance [B]

deposition time slightly and certainly does not display the same behavior as the other peaks. All films seem to have a (440) dominated growth, but especially the (211) peak is quite comparable in intensity. The presence of multiple peaks clearly indicates a polycrystalline structure of all depositions.

Kumar and Mansing observed in their work that the preferred orientation of RF magnetron sputtered was dependent on the energy of the sputtered particles arriving at the substrate surface. It was suggested that the the thermalized, low power sputtered atoms prefer the (222) direction, whereas high energy sputtered particles prefer the (400) and (440) orientation depending on their energies [79]. However, it needs to be noted that in literature mainly (222) and (400) dominated XRD-spectra are reported [110, 31, 101]. Remarkably, in the work of Kulkarni et al. (440) orientations with high intensity were reported but they were subscribed to the PET substrate, whilst other authors related the (440) peak to the addition of oxygen to the sputter gas [111].

Optical

A clear decrease in NIR transmittance is visible in the deposition time series transmittance curves (Figure 4.17 [B]). Also the increase in the number of interference fringes with increasing deposition time is very clear, both phenomena are a direct result of the increased thickness of the film. The NIR transmittance could also be decreased by the sharp increase in carrier concentration, as displayed in Figure 4.19, since it is widely known that an increase in carrier concentration drastically decreases the NIR transmittance due to free carrier absorption [112].

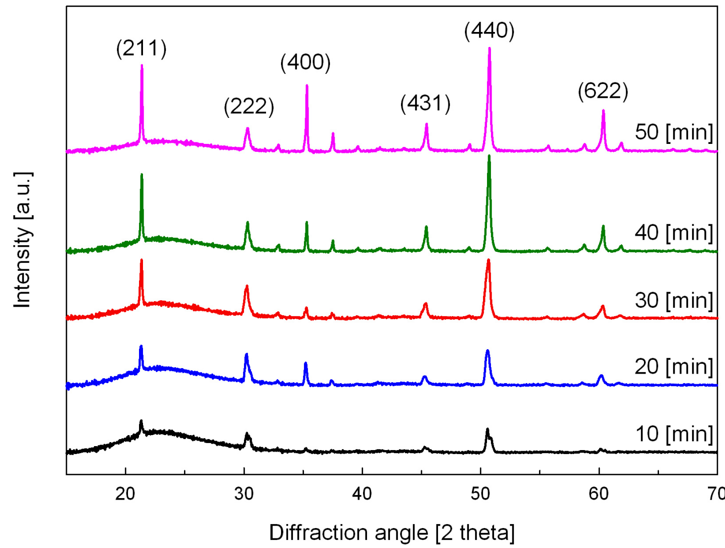

Figure 4.18: Deposition time series X-ray diffraction spectra

Electrical

The largest decrease in sheet resistance occurs with increasing the deposition time from 10 to 20 minutes, from then the decrease in sheet resistance continues but with smaller steps. The resistivity calculated from the sheet resistance and thickness measurements decreases with increasing deposition time as well, following the same trend as the sheet resistance except for the somewhat outlying 40 minute deposition.

Hall effect measurements show a clear increase in carrier concentration, whilst the behavior of the mobility is not very clear. Lee and Park [113] observed for highly crystallized ITO films an increase in carrier concentration combined with a sharp decrease in carrier mobility. They subscribed the decrease in mobility to the fact that, in highly crystallized microstructures, ionized impurity scattering becomes an important factor and decreases the carrier mobility with the carrier density.

In contrast to the observations of Lee and Park, El Akkad et al. described an increase in both carrier concentration and mobility. It was reported that the carrier concentration depends on both substrate temperature and deposition time; since thicker films are kept at the deposition temperature for longer times, higher carrier concentrations are likely. But also the increased grain sizes, and the resulting reduction of grain boundary defects, was reported to be responsible for the increase in carrier concentration. Decreased grain boundaries also reduce the grain boundary scattering and hence enhance the mobility [112].

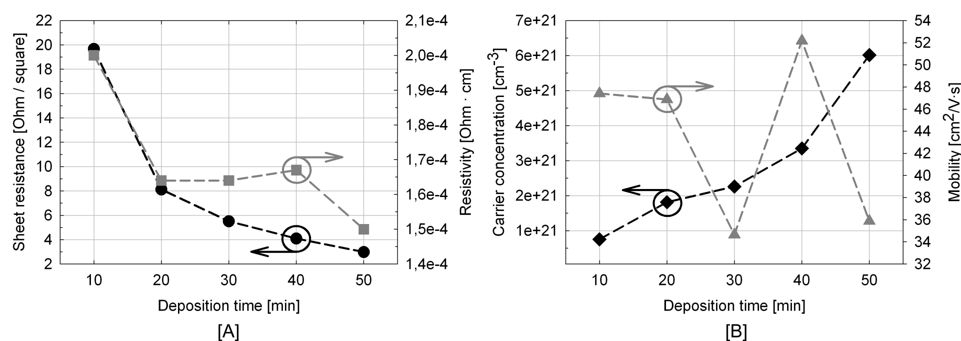

Figure 4.19: Deposition time series sheet resistance and resistivity [A], carrier concentration and mobility [B]

Figure of Merit

Especially the Φ_{TC} for the a-Si:H solar cells achieves high values, it seems that even longer deposition times could increase the Φ_{TC}^{a} further. The reason is rather clear: whilst the transmittance over almost the complete wavelength range of interest (400 - 750 nm) is comparable to that of the thinner films, the resistivity is very low. Only from around 700 nm the transmittance of the 50 minutes deposition really starts to distinct from the other depositions, but this does not influence the figure of merit anymore.

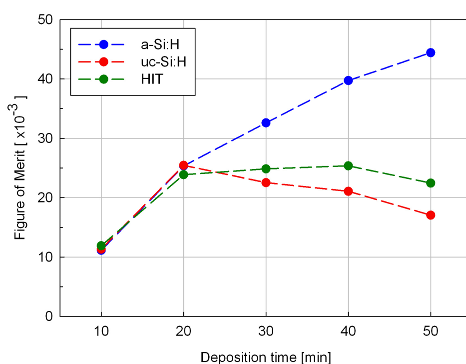

Figure 4.20: Deposition time series Figure of Merit

Since the transmittance in the 700 - 1100 nm wavelength range is quite acceptable whilst the resistivity is already quite close to the lowest value in this series (1.64 versus 1.50 $\times 10^{-4}\Omega\cdot$cm), the 20 minutes deposition achieved the highest $\Phi_{TC}^{\mu c}$. The 30, 40 and 50 minutes depositions experience a decrease in the wavelength range of interest that cannot be compensated by a further decrease in resistivity.

It is interesting to observe that the Φ_{TC}^{HIT} does not seem to change with depositions longer than 10 minutes. The strong decrease in NIR trans-

mittance is quite adequately counteracted by an increase in conductivity. Besides, since the wavelength range of interest for the HIT solar cells is wide (400 - 1100 nm) it benefits from the high transmittance in the 400 to 700 nm wavelength range equally to the a-Si:H solar cells. The highest Φ_{TC}^{HIT} is achieved by the 40 minute deposition, resulting in a ITO deposition of 408 nm with an average transmittance of 79.7% (400 - 1100 nm) and a resistivity of 1.50 $\times 10^{-4}\Omega\cdot$cm.

4.3.7 Standard recipe

Based on the results of the depositions series mentioned in the previous sections a standard recipe was prepared for use with following deposition series. The deposition parameters of the standard recipe are mentioned in the Table below (Table 4.1):

Parameter	**ITO**	**Unit**
RF power	300	W
p_{depo}	10	ubar
Ar flow	15	sccm
T_{heat}	275	°C
T_{sub}	150	°C
d	110	mm
Ramp up time	6 (30W/min from 150 W)	min
Pre-sputter time	15	min
Heating time	15 (during pre-sputtering)	min
Deposition time	30	min
Ramp down time	6 (80W/3 min to 150 W)	min

Table 4.1: ITO standard recipe deposition parameters

4.3.8 Repeatability and recovery series

During a period of 14 weeks, weekly depositions and daily pre-sputtering of the ITO target were scheduled to check the repeatability of the ITO depositions. Besides this repeatability study a recovery series of depositions was done directly after the vacuum chamber vent of May 16th. The recovery depositions were started with a deposition directly after the chamber vent and continued with a series of depositions which were preceded by an additional 60 minutes of pre-sputtering against the shutter. Table 4.2 sums the ITO depositions parameters used for the repeatability series up:

All depositions are done on 10 $\times$ 10 cm^2 Corning XG glass substrates which are prior to the deposition ultrasonically cleaned. The depositions were done at room temperature (RT) to simplify and shorten the deposition

Parameter	ITO	Unit
Ar flow	15	sccm
P_{depo}	10	ubar
T_{heat}	Room temperature	°C
d	110	mm
PRF	300	W
Ramp up time	5 (30W/min from 150 W)	min
Pre-sputter time	12	min
Deposition time	18	min
Ramp down time	6 (80W/3 min)	min
Deposition rate	10.1	nm/min

Table 4.2: ITO repeatability series deposition parameters

process. The repeatability is assumed not to be affected by the heating element, although this could be tested at a later date if required.

A total number of 12 persons were involved in doing the weekly depositions and consequent measurements; most depositions and measurements are therefore done by different persons. Due to multiple reasons only 7 of the 14 depositions were actually done; some samples were accidentally not made whilst others suffered from errors during deposition.

Repeatability series

The transmission spectra of the ITO repeatability depositions are displayed in figure 4.21 on the next page. At first sight sample W9 clearly shows a different spectral behavior. The most probable cause is that the deposition parameters used for this sample were different from the standard recipe. The spectral behavior seems to resample that of a much thinner deposition since there is only one 'hump'. These 'humps' are better known as interference fringes and are a result of interference of light caused by multiple reflections within a film. Typically a thicker deposition shows more interference fringes therefore sample W9 is assumed to be thinner than the other samples.

It is however remarkable that the sheet resistance of this sample (Figure 4.22, page 70) is quite comparable to the other samples in this series. Since it would be obvious for a thinner deposition to have a higher sheet resistance, the cause for sample's W9 different behavior cannot be (only) due to a shorter deposition. A possible explanation could be that the deposition time of the AZO experiments was used (10 minutes instead of 18) and that the substrate was heated during deposition thereby resulting in a thinner deposition with low sheet resistance (see section 2.3.5).

An alternative but obvious explanation for the optical and electrical behavior of W9 could be that the transmittance measurement was not performed at the center of the sample but on one of its sides. As may become

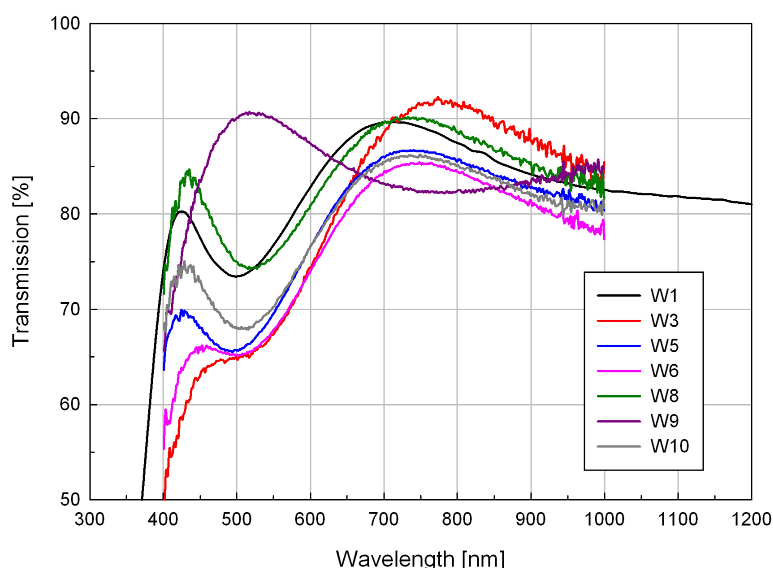

Figure 4.21: ITO repeatability series transmittance

clear from the typical thickness distribution of an ITO deposition, as displayed in Figure, an error of 30% in thickness and thus optical spectrum is easily made when changing the orientation of the spot of the MiniRT from the center of the sample to one of its sides.

However, it needs to be noted that sample W9 was the first sample after the May 16th process chamber ventilation and AZO and ITO recovery series. Since the W9 sample in the AZO repeatability was also different from the others it might also be that there was some sort of problem with the deposition apparatus that week. However, the quality of the both W9 deposition was quite good, despite the deviating optical spectra.

The remaining 6 samples differ most from each other below 550 nm. It is quite remarkable that, looking at the transmittance at around 450 nm, sample W3 has a poor transmittance of 65% whereas the 'best' sample W8 shows a transmittance of 85%. Although the spectral behavior in this region appears to be the same for all samples, the interference fringe appears around the same wavelength, the intensity of the hump is different for all samples. There does not seem to be a trend in the increase of the fringe intensity. It is also not clear why this behavior is shown. Probably it would be interesting to perform optical fitting using the Scout software; this would give some idea of the actual thickness of the deposition.

Above 550 nm two groups appear to be present, one consisting of W1 and W8 and one consisting of W5, W6 and W10. Sample W3 shows a deviating behavior in this wavelength region; the transmittance around 750 is significantly higher than the other's. Looking at the averaged transmittances and sheet resistance (Figure 4.22) of this sample it becomes clear that this is de-

position is quite different from the others. The spectral behavior does hint that the thickness of the sample is comparable to that of the other samples, this would indicate that there must be a difference in carrier concentration or mobility. Hall measurements could possibly give some indication.

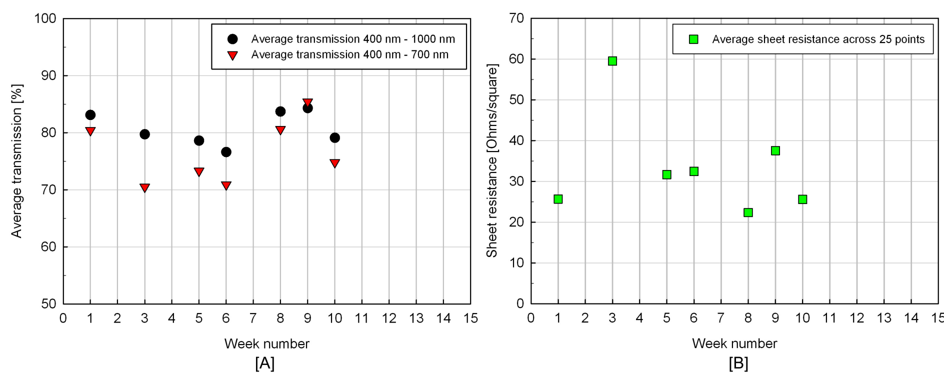

Figure 4.22: ITO repeatability series average transmittance [A] and sheet resistance [B]

Looking closer at the averaged transmittances, Figure 4.22 [A], there is a large variety in difference between the two average transmittances. Again, the W3 and W9 samples clearly stand out. For W9 the position of both transmittances confirms the hypothesis that this sample is much thinner than the others. The difference for W3 arises obviously due to the large difference in transmittance at low and high wavelengths. The average sheet resistances, Figure 4.22 [B], seems to be quite varying with time with values 'normally' between around 20 and 40 Ohms/square; they only appear to be positioned close to each other due to the extreme value of the sample of week 3.

The Figures of Merit for the ITO repeatability series, displayed in Figure 4.23 on page 71, show a wide spread. Three groups of depositions can be distinguished, one group with W1 and W8, one consisting of W3,W5 and W6 and one consisting of W9 and W10. Although there are some similarities with groups distinguished earlier, there does not seem to be a clear trend in the quality of the depositions. It can therefore be concluded that there is no real consistency of ITO quality with time.

Supplementary experiments and, in particular, more and different measurements such as Hall effect could give a better explanation for the changing ITO quality.

Recovery series

A pre-ventilation reference sample was unfortunately not made which complicates the comparison of the post-ventilation depositions; this is compli-

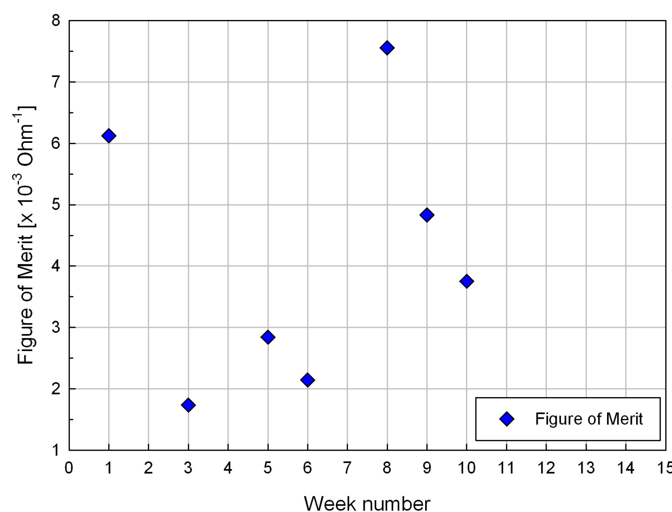

Figure 4.23: ITO repeatability series Figure of Merit

cated even more by the fact that the average transmission data shows a large spread. In general it's clear that the transmission increases with sputtering time (Figure 4.24). It is however quite surprising that the optical spectra of the +110 and +200 minutes samples are, especially in the 550 - 950 nm wavelength range, worse than that of the deposition done directly after the process chamber ventilation.

In the transmittance spectra 2 obvious groups can be distinguished, the 0 to + 200 minutes depositions and the depositions done from +290 minutes of pre-sputtering. For all depositions the optical spectra show however exactly the same behavior, although the intensity of the interference fringe around 450 nm increases with pre-sputtering and also the NIR tail of the +470 and +560 minutes depositions seem to be somewhat more horizontal. The increased intensity of the interference fringe could possibly be explained by an increasing 'brightness' of the depositions with time. It can be that the post-ventilation oxidization of the target results in a more metallic like deposition, as described in section 2.3.5; this would indirectly proof that the oxidized surface of the target is removed with pre-sputtering since the intensity of the peaks increases with sputtering time.

Figure 4.25 confirms the observation that the transmittance of the deposition done directly after the process chamber ventilation is comparable to the transmittance of the +110 and +200 minutes depositions. It is however also clear that the difference between the average transmittance over the two wavelength ranges decreases with sputtering time. As was the case with the AZO recovery series, a change in difference between these two wavelength ranges indicates a change in overall transmittance. But also here, please bear in mind that the difference is also caused by a change in deposition

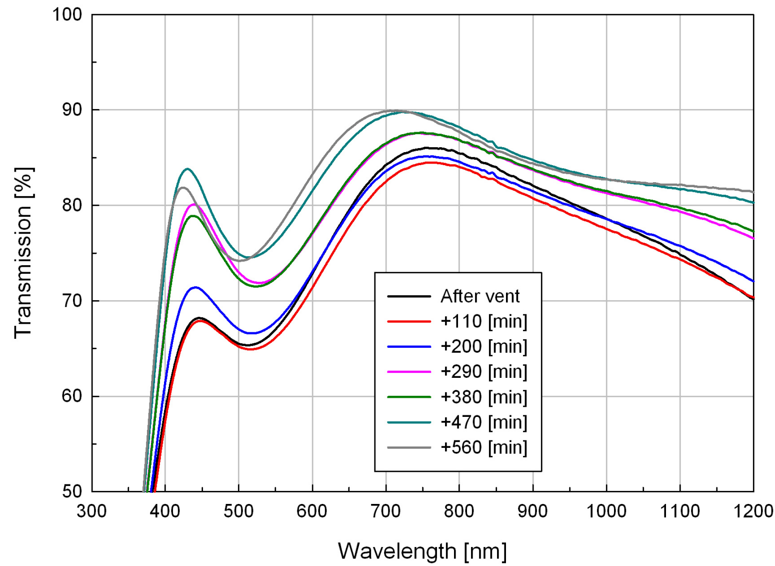

Figure 4.24: ITO recovery series transmittance

thickness.

From both averaged transmittance and sheet resistance, as displayed in Figure 4.25 on page 72, it is obvious that pre-sputtering the ITO target is beneficial. Also the sheet resistance of the 2nd and 3rd deposition have a worse or comparable sheet resistance to that of the first deposition after the process chamber ventilation. After 290 minutes of pre-sputtering both average transmittance and sheet resistance seem to be at a quite constant level.

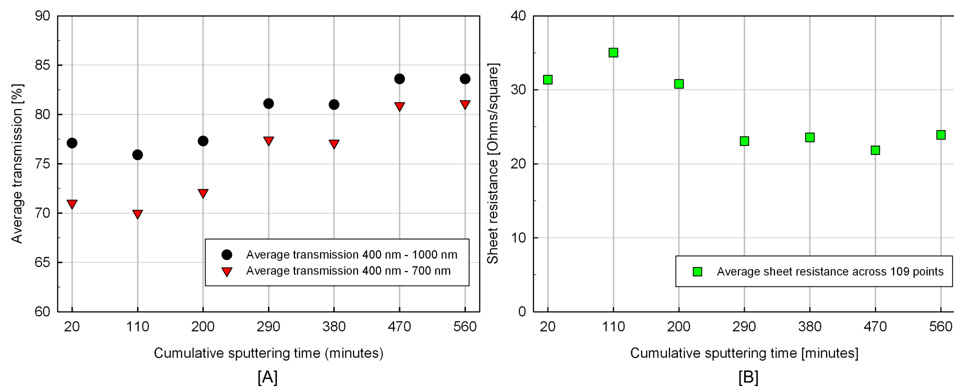

Figure 4.25: ITO recovery average transmittance [A] and sheet resistance [B]

As expected from the figures above, the Figures of Merit increase with sputtering time. But also here the behavior of the +110 and +200 minutes

depositions is remarkable. The Figure of Merit however does not seem to settle at a constant level, it would be interesting if there was another sample deposited at +650 minutes. The quality of the +290 minutes deposition is however quite good and it is therefore advised to adopt a pre-sputtering time of 290 minutes.

The chance of error during deposition and measurement of the ITO recovery series was significantly decreased since only one person was involved. For further research on both AZO and ITO repeatability and recovery series it is advised to limit the total number of persons involved since this will most probably result in more consistent procedures.

4.3.9 Effect of annealing

In a first attempt to verify the usability of annealing three samples have been annealed for 1 hour at atmospheric pressure and under vacuum, both with a temperature of 180°C. Although a higher temperature generally results in an increased annealing effect, a maximum temperature of 180°C was adopted from device point of view; higher temperatures will cause damage to substrate solar cells (n-i-p configuration and HIT) which are deposited before, after which the TCO is deposited on top. This initial test showed that whereas annealing under atmospheric pressure did not result in any improvement of the electrical properties, annealing under vacuum almost halved the sheet resistance.

Hu et al. [114] found that when annealed in air, the free oxygen in the air will react with the ITO. The reaction decreases the number of oxygen vacancies and carrier concentration which results in an increase of resistivity. In the case of vacuum annealing there is no such reaction, the crystalline structure of the ITO only becomes more perfect. However, some oxygen atoms absorbed at the ITO surface may escape, causing the carrier concentration to increase.

A second series of depositions, with varying substrate temperatures, was used to research the difference between regular vacuum annealing and nitrogen annealing (vacuum with small flow of nitrogen). The annealing effect was quite evident; whereas nitrogen annealing increased the resistivity for the majority of depositions, vacuum annealing decreased the resistivity for all depositions. The figure below (Figure 4.26 [A]) displays the as deposited, vacuum annealed and nitrogen annealed resistivity for a series of depositions done at different substrate temperature. The figure on the right (Figure 4.26 [B]) shows the as deposited, vacuum annealed and nitrogen annealed transmittance spectra for the number II deposition from the left figure.

A clear shift of band edge to lower wavelength (Burstein-Moss shift, section 2.2.3) is visible, as well as a lower transmittance in the NIR region. These two observations are confirmed by Hall measurements performed on the as-deposited and vacuum annealed samples which show a decrease of

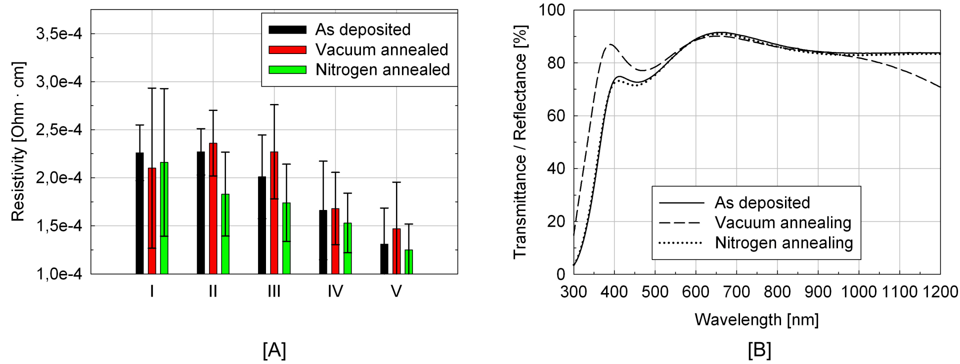

Figure 4.26: Effect of annealing: variation in resistivity [A] and changes in transmittance spectra [B]

resistivity of around 20%. It needs to be mentioned that, in contrast to literature, the carrier mobility was decreased thereby reducing the enhancement of the electrical properties. It is not clear why the mobility decreased. It can be due to the sample size of the Hall measurement sample and the different locations used to obtain these samples.

Based on the observed decrease in resistivity, combined with what was found in literature [114, 35, 34], it was decided that all other depositions were annealed for 1 hour at 180°C under vacuum conditions without the addition of nitrogen gas. Sheet resistance measurements on annealed slabs from the power, pressure and deposition time series series showed an average decrease in sheet resistance of 25.1%, 7.6% and 16.2% respectively.

XRD patterns of an as-deposited and vacuum annealed ITO deposition are displayed in Figure 4.27. Both as-deposited and vacuum annealed samples show a cubic structure with diffraction peaks corresponding to (211), (222), (400), (431), (440) and (622) reflections. Annealing does not seem to structurally change the ITO, the intensity of the (211) and (440) peaks are however increased with annealing. This indicates a change in atomic distribution in the unit cell which could be due to the release of oxygen atoms absorbed at the ITO surface.

However, it needs to be noted that the ITO deposition used for XRD analysis is not the same sample depicted in Figure 4.26. Yet it does visualize that the as-deposited ITO is already crystalline. A possible reason for the as-deposited samples being crystalline could be that the power density used for the depositions is rather high. XRD analysis of depositions with varying sputter power could offer more insight in this matter.

4.3.10 Effect of etching

The possibility of ITO etching was examined using multiple recipes retrieved from literature. Standard depositions (Appendix B) on 10×10 cm^2 Corning

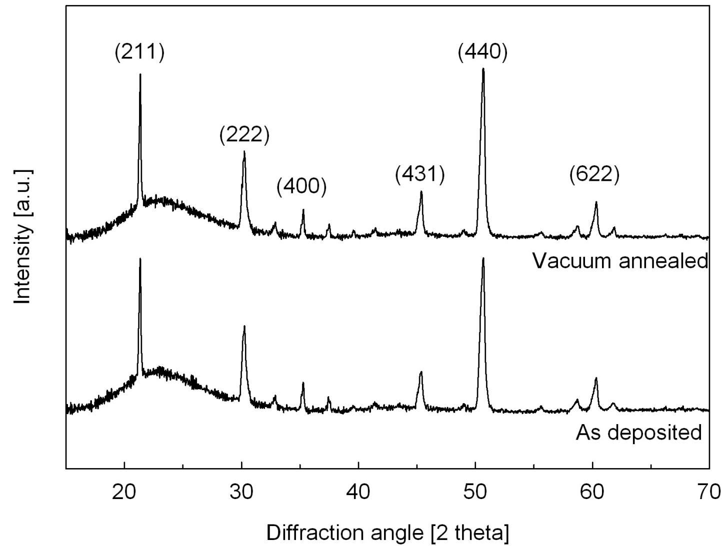

Figure 4.27: XRD patterns of as-deposited and vacuum annealed ITO deposition

Eagle 2000 glass were cut into small pieces and subsequently wet chemically etched using the following etching solutions:

- HCl(37%):H_2O = 1:70
- HCl(37%):H_2O = 1:2
- HCl(37%):H_2O = 1:1
- HF(35%):H_2O_2(40%):H_2O = 1:1:10
- HF(35%):H_2O_2(40%):H_2O = 2:2:10

The HCl(37%):H_2O = 1:70 etching solution is normally used to succesfully etch ZnO:Al depositions. ITO was kept in this solution for 20 minutes without any noticable or measurable change in optical, electrical or structural change. Ethcing behavior of this recipe was not expected as this recipe is not related to ITO etching in literature.

Etching solutions with higher concentrations of hydrochloric acid, as the second and third in the list above, are mentioned frequently in articles on ITO wet chemical etching [115, 116, 117, 118, 119]. Standard ITO depositions were immersed in both HCl(37%):H_2O = 1:2 and HCl(37%):H_2O = 1:1 etching solutions for periods varying from 5 to 25 minutes. Again no change in optical, electrical or structural properties of the ITO deposition was noticed.

In contrast to observations from literature, the HCl(37%):H_2O = 1:2 and HCl(37%):H_2O = 1:1 etching solutions did not result in any optical, electrical or structural change of the ITO. An obvious explanation for this can be found in the fact that the depositions are quite dense and crystalline.

A HF(35%):H_2O_2(40%):H_2O = 1:1:10 which had been standing unused in a wet bench for 3 days was used to check the etching effect since it was found that this solution could be used for ITO etching. After being immersed for 25 minutes only some small etched 'pits' were visible, but it was clear that this solution did succesfully etch. However, it was believed that by the time the solution was used the H_2O_2 had dissipated from the solution thereby resulting in a less effective etching behavior. Therefore another experiment was performed with the same chemical composition. The result was similar to that of the solution which had been standing for 3 days.

Since the HF(35%):H_2O_2(40%):H_2O = 1:1:10 recipe did etch but not in a satisfactory way the HF and H_2O_2 content was doubled leading to a HF(35%):H_2O_2(40%):H_2O = 2:2:10 solution. The sample was immersed for consequent periods of 5 minutes; after 25 minutes the ITO was completely etched away. From 0 to 15 minutes no change was visible, from 20 minutes the ITO started to become 'milky'. Most remarkably, at the location where the ITO deposition was the glas showed a strong 'milky' effect whilst the locations where no ITO was deposited seemed to be unharmed. The etching of the ITO clearly resulted in a nonuniform etching of the glass substrate.

The etched glass was used as a substrate for a standard 300 nm ITO deposition to verify if the rough surface of the glass was taken over by the ITO. Optical measurement of the total transmittance T_t and diffuse transmittance T_d was used to determine the Haze parameter, i.e. the portion of light that is diffusely scattered due to the rough interface. The Haze of the etched glass was nearly constant at a value of just above 0.9 over the wavelength range of 300 to 1200 nm. This is quite remarkable because, for example, an optimally etched ZnO:Al deposition experiences a maximum Haze of around 0.7 at short wavelengths (400 nm) which decreases rapidly to a value of around 0.1 at 1000 nm.

AFM analysis of the etched glass showed a tremendous increase in average surface roughness for the etched glass; whereas regular Corning XG glass has a root mean square surface roughness (σ_{rms}) less than 5 nm, the etched glass showed a σ_{rms} of 750 nm. Deposition of a 800 nm thick ZnO:Al layer on top of the etched glass decreased the σ_{rms} to a value of 548 nm. More interesting, subsequent etching of the ZnO:Al deposition with a diluted 0.5% HCl solution resulted in so-called double-textured surface with a σ_{rms} of 527 nm. The as-deposited, etched glass with ZnO:Al deposition and etched glass with etched ZnO:Al AFM scans are displayed in Figure 4.29.

The etched glass with ZnO:Al deposition shows large craters of up to 10 μm in diameter. ZnO:Al is widely known to readily etched by a diluted 0.5% HCl solution thereby creating a textured surface. From Figure 4.29 it

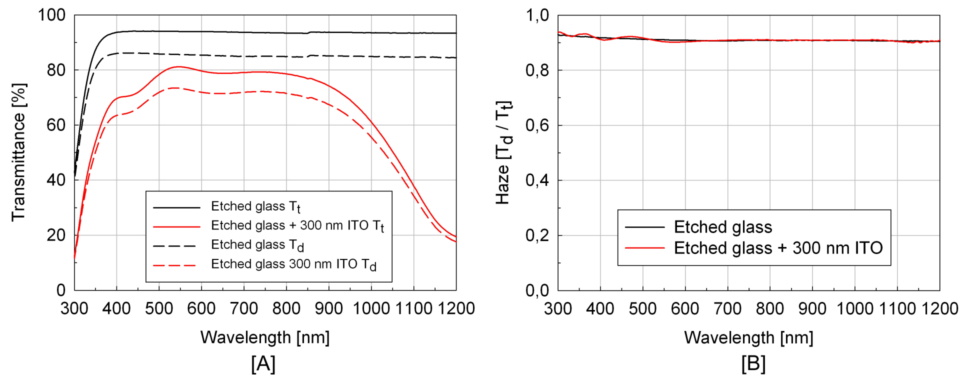

Figure 4.28: Transmittance spectra of the etched glass and the etched glass with 300 nm of ITO [A] and the resulting Haze parameter [B]

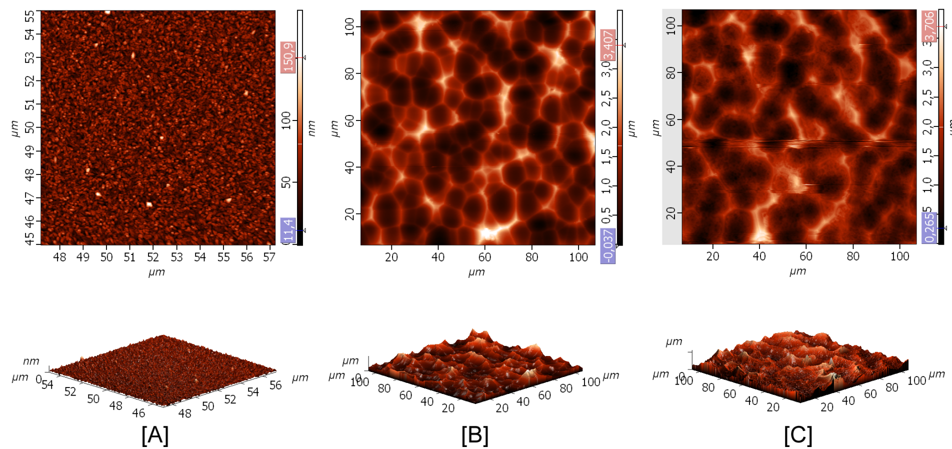

Figure 4.29: As-deposited ITO [A], etched glass with ZnO:Al deposition [B] and etched glass with etched ZnO:Al [C]

appears that the ZnO:Al deposition follows the large craters of the etched glass, the subsequent etching of ZnO:Al results in even more texturization of the surface; the surface of the large craters is now covered by small craters as well. Further optical measurements (TIS and Variable Angle Spectroscopy (VAS)) are needed to fully characterize such substrates.

4.3.11 Tilted angle sputtering

Experiments on tilted angle sputtering of ITO were done using regular 10×10 cm^2 Corning Eagle 2000 glass substrates as well as so-called seed layers deposited on glass substrates.

Regular depositions

A standard ITO deposition (Appendix B) was done at an inclination of 0° and 45° using the tilted angle substrate holder (TASH). Optical and electrical properties of the depositions were found to be quite bad, most probably caused by an oxidized TASH which had been stored for a prolonged period of time. Since this deposition run was intended as tilted angle deposition experiment, optical and electrical properties will not be discussed. The diffraction patterns for the 0° and 45° deposition are displayed in the figure below (Figure 4.30).

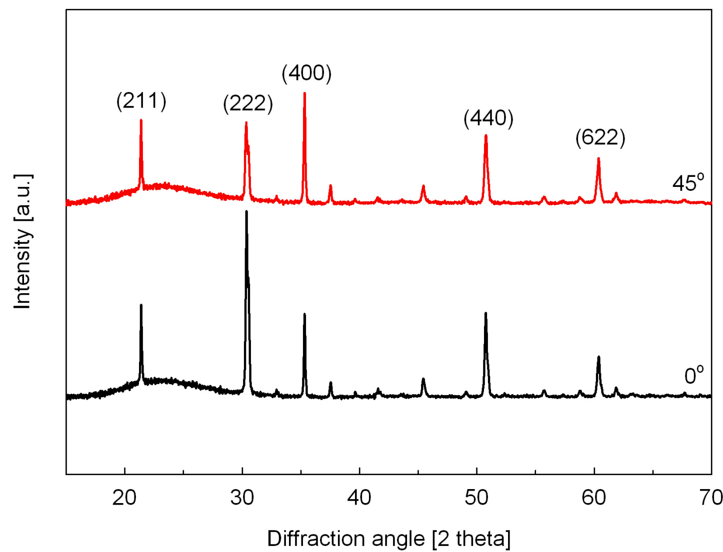

Figure 4.30: Diffraction patterns for standard ITO deposited at 0° and 45°

The diffraction patterns show that the ITO films correspond to the cubic bixbyite In_2O_3 structure. Multiple diffraction peaks are visible, thereby clearly indicating a existence of multiple crystal orientations. A sharp decrease in (222) intensity for the 45° deposition is visible. However, the (400) peak of the 45° is increased when compared with the non-inclined deposition. The (222) peak for the 0° deposition shows the highest intensity, three other peaks ((211), (400) and (440)) share comparable intensities. The deposition seems therefore to have a ⟨111⟩ governing orientation although other orientations such as ⟨100⟩, ⟨110⟩ and ⟨211⟩ orientations coexist. The 45° deposition seems to have a slightly higher ⟨100⟩ orientation, but it needs to be noted that all 4 obvious peaks are quite equal in intensity. There are no changes in peak position visible, which indicates that the unit cell symmetry and size remain constant. There are also no changes in particle size and defects since only the peak intensities change and not the actual peak shapes (width).

A 200 minutes deposition[1] was done with inclinations of 0°, 60° and 80° to further investigate the possibility of inclined ITO growth. The diffraction patterns are displayed in Figure 4.31:

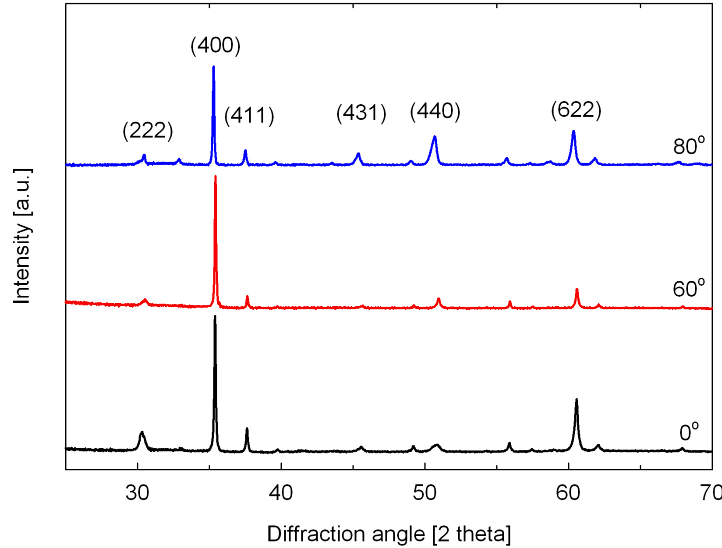

Figure 4.31: Diffraction patterns for 200 minutes ITO deposited at 0°, 60° and 80°

All depositions show a very high (400) peak intensity, although the intensity of the (400) peak for the 80° is substantially lower. It is interesting to compare the 0° deposition in the above figure with the 0° of Figure 4.30; it seems that with increasing the deposition time the intensity of the (400) peak increases at the expense of the intensity of the (222), (440) and (622) peaks. This indicates that for long deposition runs the preferred orientation of the ITO is along the ⟨100⟩ direction.

All diffraction peaks of the 80° angle deposition are slightly shifted to lower diffraction angles when compared to the 0 and 60° substrate angle depositions. A shift of a diffraction peak is the result of a change in unit cell symmetry and size. In this case, the shift to lower diffraction angles possibly results from a small increase in lattice constant [87].

The (622) peak is initially decreased with sputter angle, but from 60 to 80° the intensity is again comparable to the initial value. The (431), (411) and (222) peaks show a similar behavior, but it needs to be noted that the initial values for the (222) and (411) at 0° sputter angle is somewhat higher. An obvious explanation for the decrease in intensity with substrate inclination could be that the resulting film thickness at higher substrate angles is lower. Due to bad transmittance of these depositions the thickness

[1]Apart from the deposition time the standard ITO recipe was used (Appendix B)

could unfortunately not be verified by means of MiniRT measurement and Scout software fitting.

Seed layers

Besmaine et al. successfully deposited inclined ZnO:Al by using silicon and diamond substrates [90]. To reproduce this experiment four samples were prepared with a so-called seed layer were provided by the Delft Institute of Microsystems and Nanoelectronics (DIMES). The seed layers were intended to be amorphous and rough which could enhance the shadowing effect and consequent inclined growth of the deposition [91, 90].

Three different materials were used as seed layer: SiO_2, Al_2O_3 and AlN. The silicon oxide was deposited with a thickness of 50 and 100 nm, the Al_2O_3 and AlN were both 100 nm thick. A standard 300 nm deposition of ITO was done on top of the seed layers with the substrate tilted at an angle of 45°, all samples were post-annealed for 1 hour at 180 °C under vacuum conditions.

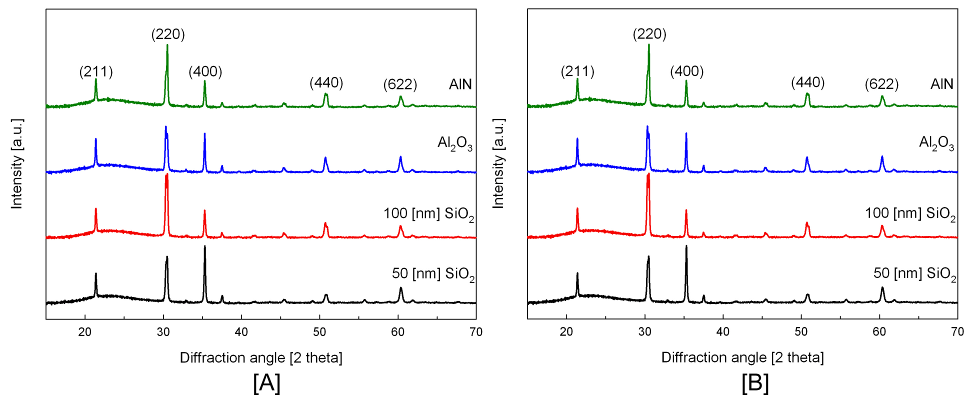

Figure 4.32: Seed layers as-deposited [A] and post-annealed [B] transmittance

The as-deposited and post-annealed samples were analyzed by means of XRD as well. The diffraction patterns for the samples are displayed in Figure 4.32. The distribution of peaks shows great similarity to that of the diffraction pattern shown in Figure 4.30, thereby indicating that the seed layers do not differ structurally from layers deposited without seed layers. There are however some minor differences. The deposition done at 50 nm SiO_2 experiences the highest intensity for the (400) deposition, both as-deposited and annealed. The other three seed layers have the largest intensity for the (220) orientation.

As for the regular ITO deposition done at 0° and 45°, the depositions done on top of the seed layers do not change structurally by annealing.

4.4 Conclusions

Variation of the deposition parameters has resulted in an optimized recipe for ITO TCOs. By using the dedicated Figures of Merit the theoretical best set of deposition parameters for each of the three different types of solar cells made within the PVMD group is established.

The deposition rate increased with substrate temperature as expected, a similar trend was visible for the films conductivity. Good optical transmittance combined with the decreasing resistivity with substrate temperature resulted high Figures of Merit for all types of thin-films solar cells. It is however advised to maintain a maximum substrate temperature of 150 $^\circ$ to prevent damage to devices.

An almost linear dependence of the deposition rate with the RF power was visible; increasing the RF power increase the deposition thickness. With increasing RF power an increase in interference fringes was visible, there was however no indication of reduced spectral behavior. The electrical properties, both from four-point probe and Hall setup, show a substantial improvement with increasing RF power; the resistivity of the 350 Watt deposition is almost halved when compared to the deposition done at 200 Watt. The decrease in resistivity could be attributed to a sharp combined increase in carrier concentration and mobility. Whereas Φ_{TC}^{a} reaches it's maximum value at a RF power of 350 Watt, the $\Phi_{TC}^{\mu c}$ and Φ_{TC}^{HIT} reach their maximum value at 300 Watt.

Increasing the sputter pressure resulted in a parabolic behavior of the deposition rate which seemed to level at 20 μbar. The large variation in thickness was also visible in the transmittance spectra. The sheet resistance varied little with sputter pressures of 2.6, 5 and 10 μbar, but with increasing the sputter pressure more the sheet resistance first showed a slight drop followed by a significant increase. At the same time the resistivity showed more a V-shape behavior with a minimum resistivity at 15 μbar. The Φ_{TC}^{a} was maximal at a sputter pressure of 15 μbar, $\Phi_{TC}^{\mu c}$ and Φ_{TC}^{HIT} showed a maximum at 5 μbar.

The effect of oxygen addition to the sputter gas was researched by varying its concentration from 0 to 1%. The deposition rate decreased slightly with increasing oxygen content. More impressive was the increase in NIR wavelength transmittance due to the decreased carrier concentration. Sheet resistance and resistivity increased with increasing oxygen content, whilst the carrier concentration and mobility decreased significantly. In contrast to what is reported by many authors, oxygen was not necessary to improve the ITO quality; all highest Figures of Merit were achieved for the deposition without oxygen.

The target-to-substrate distance was varied from 65 to 165 mm. Installing the substrate further away from the target results in a thinner deposition with higher NIR wavelength transmittance. The resistivity increases

however as well with target-to-substrate distance. The $\Phi_{TC}^{\mu c}$ and Φ_{TC}^{HIT} displayed a quite constant behavior with increasing target-to-substrate distance, whilst the Φ_{TC}^{a} was more than halved. Three-dimensional plots of the target-to-substrate series revealed that the depositions are quite non-uniform.

From XRD-analysis on the thickness series a clear cubic crystalline structure with strong (211), (400) and (440) peaks is identified for the standard ITO depositions. Sheet resistance and resistivity showed a steady decrease with increasing deposition time, the mobility was quite fluctuating with deposition time but the carrier concentration showed a very acceptable increase,

The optical properties of ITO were found to be quite variable over time. It was not clear why the depositions were that variable, it could be attributed to too short pre-sputtering time. After a deposition chamber ventilation the ITO targets needs more than 5 hours of continuous sputtering at high pressure to remove any contaminants from the surface of the target.

Although the first experiments concerning post-deposition annealing were not decisive, it was decided to adopt a 1 hour at 180 ° vacuum anneal recipe for future depositions. Annealing of these samples did indeed show that post-annealing is quite beneficial for both transmittance and sheet resistance.

Etching of ITO was reported to be uncontrollable. Etching of an ITO deposition in an HF:H_2O_2:H_2O solution resulted however in a highly etched glass substrate. Total and diffuse transmittance measurement showed an almost constant Haze of 0.9 over the 300 - 1200 nm wavelength range.

Inclined growth of ITO using the tilted angle substrate holder was attempted by depositing ITO directly on a inclined glass substrate and by using so-called seed-layers. No structural change was however observed for the depositions on SiO_2, Al_2O_3 and AlN. An ITO deposition with a 80 ° showed however a slight shift in diffraction peaks, indicating a change in unit cell symmetry and size.

Chapter 5

a-Si:H optimization

5.1 Introduction

High quality optimized ITO for application as front TCO for a-Si:H solar cells was described in the previous chapter. This chapter focuses on the actual application of ITO TCOs in both n-i-p and p-i-n a-Si:H solar cells. The objective is to test if application of the ITO TCO in the PVMDs a-Si:H devices produces functioning solar cells. Multiple p-i-n solar cells with various front and back TCO were deposited (section 5.2.1), as well as a n-i-p device (section 5.2.2). In the following sections the performance of the p-i-n and n-i-p devices will be evaluated and compared to the performance of the same devices with ZnO:Al (AZO) or SnO_2:F (Asahi U-type) from Asahi Glass Company TCOs.

5.2 Experimental

Hydrogenated amorphous silicon solar cells both in n-i-p and p-i-n configuration were deposited with and without ITO as front and/or back TCO. In section 5.2.1 the performance of several a-Si:H p-i-n devices will be described, section 5.2.2 describes the performance of a n-i-p device.

5.2.1 p-i-n devices

A total number of 5 a-Si:H p-i-n deposition runs with ITO as front and/or back TCO were done. These solar cells were compared with similar devices using either Asahi as front TCO or AZO as front and/or back TCO. The composition of the complete series of a-Si:H solar cells is mentioned in Table 5.1.

The production of the solar cells started with ultrasonically cleaning of $10 \times 10\ cm^2$ Corning Eagle 2000 glass substrates and subsequent deposition of either ZnO:Al of ITO on the substrate. The standard recipe (Appendix

Device number	Front TCO	Back TCO
1	Flat AZO	-
2	Flat AZO	AZO
3	Flat ITO	-
4	Flat ITO	ITO
5	Rough AZO	-
6	Rough AZO	ITO
7	Rough AZO	AZO
8	Asahi	-
9	Asahi	ITO
10	Asahi	AZO

Table 5.1: a-Si:H p-i-n devices front and back TCO

B) for ITO front TCOs was used for the ITO front TCO, resulting in a 300 nm thin film. The ZnO:Al was post-deposition etched in a diluted 0.5% HCl solution to introduce surface roughness, etching was not performed on the ITO. A thin layer of ZnO:Al was deposited on top of the Asahi and ITO TCOs to allow simultaneous deposition of the amorphous silicon on the Asahi, ZnO:Al and ITO TCOs in one run.

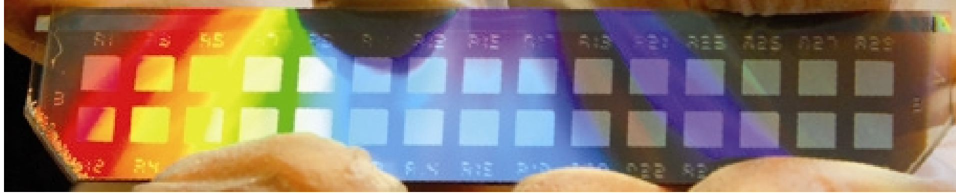

Figure 5.1: Individual solar cells on 3×10 cm^2 glass substrate

Plasma Enhanced Chemical Vapor Deposition (PECVD) was used to deposit the amorphous silicon layers on top of the TCOs. The PECVD sequence started with a 5 minute hydrogen treatment, followed by a 5 nm boron doped μc-Si:H thin layer. On top of this μc-Si:H thin layer 10 nm of boron doped a-Si:H was deposited, followed by a 300 nm thick intrinsic a-Si:H and a 20 nm thick phosphor doped a-Si:H n-layer. All the above mentioned depositions were done on relatively large substrates, normally stripes of 3×10 cm^2 cut from the initial 10×10 cm^2 glass substrate. On these glass stripes a number of individual solar cells is created by using a mask and subsequently applying a 100 nm thick silver back contact by means of thermal evaporation (Figure 5.1) . Some of the depositions were provided with a back TCO deposition prior to the thermal evaporation. The individual solar cells were characterized by means of the illuminated I-V solar simulator.

Results and discussion

The 10 deposition runs will be divided into four groups to facilitate easy comparison. The groups are defined on basis of the type of front TCO, resulting in the following groups: front flat AZO, front flat ITO, front rough AZO TCO and Asahi front TCO. From the total number of solar cells for each of these deposition runs the 'best' (low R_s (<10 $\Omega \cdot cm^2$), high R_p (>1000 $\Omega \cdot cm^2$) resulting in $FF > 0.6$) individual solar cells (dots) were selected. From these dots the average value and standard deviation are displayed in Figure 5.2. The green bins represent the flat AZO front TCO, the blue bins the flat ITO front TCO, the red bins the rough AZO front TCO and the pink bins the Asahi front TCO. The groups are subdivided by the back TCO used: no pattern represents no back TCO, diagonal pattern represents ITO back TCO and crossed pattern represents the back AZO TCO.

The bar chart for the open circuit voltage, bottom Figure 5.2 [A], displays a distinct difference between the p-i-n devices with solely ITO front TCO (blue bins) and those with flat AZO front TCO (green bins). Remarkably the flat AZO front TCO solar cells V_{oc} seems to improve very little with application of the AZO back TCO, whereas the ITO front TCO shows a distinct increase in V_{oc} with the application of the ITO back TCO. The error bars for the flat ITO front TCO solar cells indicate however a substantial standard deviation caused by the limited amount of useful solar cells from both ITO front TCO deposition runs. Especially the front ITO without back TCO deposition run suffered from a very low number of usable solar cells.

Compared to the rough AZO and Asahi front TCO (the current optimized front TCOs within the PVMD group), the flat ITO has a much lower V_{oc}, although again the error bars should be taken into account. Besides this obvious deviation, a significant improvement of the V_{oc} for the front ITO device with and without back TCO is visible, indicating the importance of a back TCO between the n-layer and the back side contact for these particular solar cells.

The J_{sc}, Figure 5.2 middle-bottom, of the flat AZO and ITO front TCO are comparable. The effect of surface texturing is nicely illustrated by the increased J_{sc} of the rough AZO and Asahi front TCO. For the rough AZO front TCO the J_{sc} for the cells with the AZO back TCO is noticeably higher than the J_{sc} of the cells with ITO back TCO and without back TCO. It is interesting to observe that for the Asahi front TCO the apparent increase in J_{sc} by the ITO back TCO is larger than that of the AZO back TCO, although the error bars for the ITO back TCO are quite large. It could be that the roughness of the Asahi results in a textured ITO which scatters the light more efficient than the eventually textured AZO thereby increasing the J_{sc}. On the other side, for the AZO front TCO the ITO back TCO performs

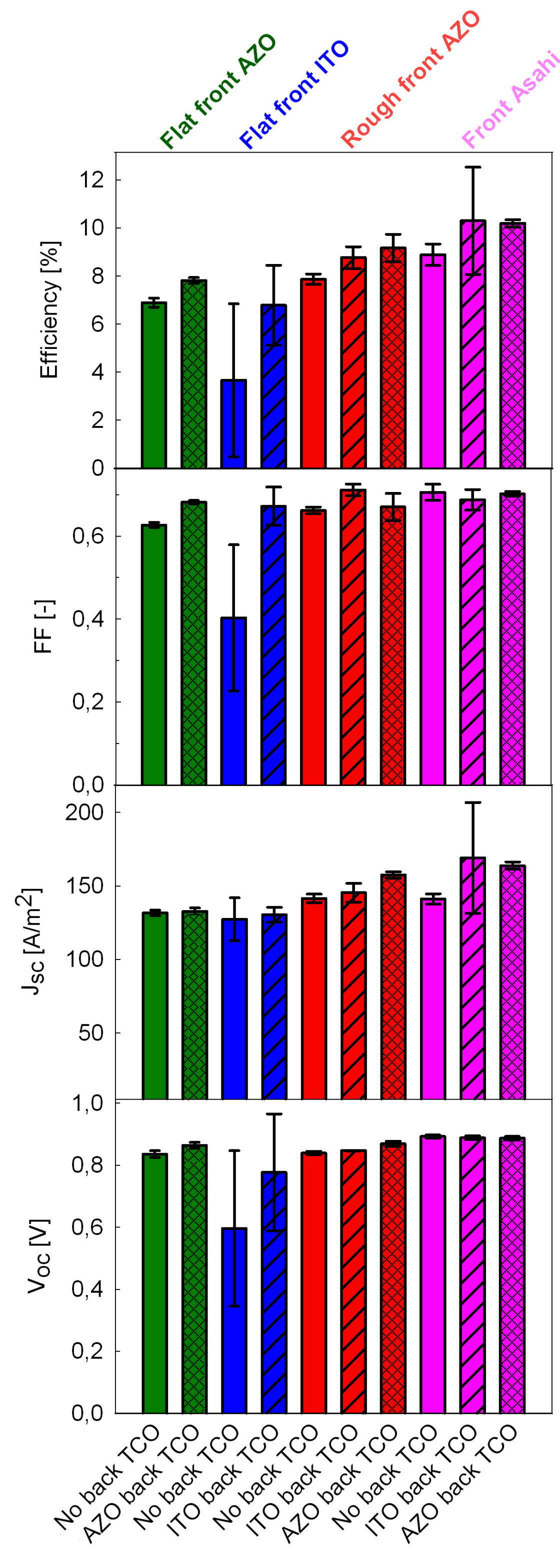

Figure 5.2: a-Si:H p-i-n external parameters

worse than the AZO back TCO (red bars). It would therefore be interesting to repeat the Asahi front TCO depositions to verify if the same result is obtained.

The flat ITO TCO without back TCO shows a minimum in FF, indicating a bad ratio between the maximum power deliverable by the cells and the product of J_{sc} and V_{oc}. Application of the ITO back TCO improves the FF however remarkably (almost doubled), even though error bars for flat front ITO without back ITO indicate a probable malfunctioning of the entire stripe of such cells. The FF of these solar cells with solely ITO TCOs is comparable to the FF of the cells with flat/rough AZO or Asahi front TCO with/without back TCO.

The non-stabilized efficiencies resulting from the V_{oc}, J_{sc} and FF are displayed in at the top of Figure 5.2 [B], the table below (Table 5.2) displays the efficiency of the best cell from each deposition run. Although the average efficiency of the flat ITO TCO without back TCO is quite low and large error margins are present, the efficiency of the best cell is more than 0.5% higher than that of a comparable solar cell with an flat AZO front TCO. This is a promising result for eventual application of an etched / textures ITO front TCO, which could possibly achieve the same or better performance as the rough AZO front TCO. It needs to be noted that the Asahi front TCO without back TCO has a significant higher efficieny (1.6%) than the rough AZO fron TCO without back TCO.

	No back TCO	AZO back TCO	ITO back TCO
Front flat AZO	7.29	8.05	-
Front flat ITO	7.84	-	8
Front rough AZO	8.14	9.73	9.69
Front Asahi	9.7	10.4	10.7

Table 5.2: a-Si:H single junction n-i-p solar cell initial efficiencies of best solar cells

The efficiency of the best cell with rough AZO front TCO with AZO back TCO is comparable to the efficiency of the best rough front AZO TCO with ITO back TCO. More interestingly, both the averaged value as well as the highest value for solar cells deposited on the Asahi front TCO with ITO back TCO is higher than those values for the Asahi front TCO with AZO back TCO. It needs to be noted however that the standard deviation for the Asahi front TCO with ITO back TCO is quite substantial.

5.2.2 n-i-p devices

An Asahi U-type TCO was used as substrate for a n-i-p deposition run with ITO front TCO. The ITO was deposited using the standard recipe

(Appendix B) but with a deposition time of around 8.5 minutes resulting in a 85 nm thick deposition.

A silver back reflector was thermally evaporated on the glass side of the Asahi U-type TCO, followed by the PECVD deposition of the n-i-p structure and finally the ITO was deposited on the p-layer to form the top contact. This n-i-p deposition run will be compared with a n-i-p deposition run on regular Corning Eagle 2000 glass with both back and front AZO TCO.

Results and discussion

The external parameters of the solar cells of both n-i-p deposition runs are mentioned in the table below (Table 5.3). In the table the external parameter of the best solar cell as well as the averaged value over a selected number of around 10 cells are presented.

Sample	V_{oc} [V]	J_{sc} [A/m^2]	FF [-]	η [%]
ITO	0.843	118	0.633	6.31
average	0.829	107	0.612	5.43
AZO	0.807	130	0.609	6.39
average	0.810	120	0.568	5.52

Table 5.3: a-Si:H n-i-p solar cell performance

The V_{oc} for the best cell as well as the averaged value for the n-i-p device with front ITO is higher than the V_{oc} for the complete AZO device. Since there is no device made with Asahi substrate and AZO front TCO the origin of this higher V_{oc} cannot be ascribed to the use of the ITO front TCO or Asahi substrate unreservedly.

In contrast to the higher V_{oc}, the J_{sc} for the ITO front TCO devices is somewhat lower. The FF of the ITO front TCO devices is higher than the FF of the AZO devices, but the overall conversion efficiency is higher for the AZO devices. Again it would be very interesting to deposit a more comparable series of n-i-p devices to allow reliable comparison.

5.3 Conclusions

Thin-film a-Si:H solar cells with ITO TCOs were successfully prepared. Although the averaged external parameters of the p-i-n devices with ITO front TCO are worse than those of devices made with AZO or Asahi front TCO, individual ITO front TCO solar cells without back TCO showed higher initial efficiency than the AZO front TCO solar cells without back TCO. Application of ITO back TCO was quite successful; averaged values for the solar cells with ITO back TCO were comparable to the ones without or with AZO back TCO. The Asahi front TCO with ITO back TCO even showed the

highest initial efficiency. Further optimization, based on the actual application and performance of the ITO in the p-i-n device, is advised to achieve better performance.

A n-i-p deposition run was also done successfully using ITO as a front TCO. The performance of the solar cells, with an Asahi substrate, was slightly less than that of a complete AZO n-i-p device. Deposition of a series of n-i-p solar cells with similar substrates (such as Asahi or etched AZO) with different front TCO (AZO or ITO) would allow better comparison. Improvement of the ITO TCO for the n-i-p could possibly achieved by this comparison.

Chapter 6

ucSi:H optimization

6.1 Introduction

Tin-doped indium oxide is generally excluded as TCO for μc-Si:H solar cells. The ITO is not stable when it is exposed to a silane plasma since the deposition of silicon based layers on top of ITO lead to serious problems with indium diffusion and lifetime reduction in the silicon layers [5]. In contrast to this general thought a deposition run of μc-Si:H using an ITO front TCO was performed.

6.2 Experimental

An ITO TCO deposited using the below mentioned parameters (Table 6.1) was provided for the μc-Si:H. These parameters followed from the optimization as described in chapter 4. Based on the outcome of earlier experiments and from what is known from literature, it was decided to deposited a thin layer of AZO on top of the ITO to protect the ITO from the silane plasma. This method is also used for other TCOs which suffer from the PECVD deposition conditions such as SnO_2:F. The AZO was subsequently dipped in a diluted 0.5% HCl solution for a period of 5 seconds to improve the surface roughness of the AZO and thereby the adhesion of the microcrystalline layer on the TCO. The p-i-n layers were deposited on the rough AZO, followed by the deposition of back ITO TCO and back reflector.

6.3 Results and discussion

The external parameters for the μc-Si:H deposition run with ITO are mentioned in the table below (Table 6.2). In the table the external parameter of the best solar cell as well as the averaged value over a selected number of around 10 cells are presented.

Parameter	**ITO**	**Unit**
RF power	300	W
Ar flow	15	sccm
p_{depo}	10	ubar
T_{heat}	275	°C
T_{sub}	150	°C
d	90	mm
Pre-sputter time	15	min
Deposition time	20	min

Table 6.1: ITO TCO deposition parameters for μc-Si:H deposition run

Sample	V_{oc} [V]	J_{sc} [A/m^2]	FF [-]	η [%]
ITO	0.392	71.100	0.600	1.670
average	0.379	67.488	0.582	1.489

Table 6.2: μc-Si:H p-i-n solar cell performance

From the table it is clear that the μc-Si:H individual cells share a low V_{oc} and J_{sc}. The FF however is quite acceptable with an averaged value approaching 0.6.

6.4 Conclusions

A μc-Si:H deposition run with ITO TCO was successfully performed. Although a low V_{oc} and J_{sc} resulted in a low overall conversion efficiency, the FF for these individual solar cells was quite acceptable. Future optimization of ITO TCOs for μc-Si:H should focus on improving both V_{oc} and J_{sc}, whilst keeping the FF at least as high as for the current deposition run. The protective deposition of a different TCO material to protect the ITO TCO from the silane plasma needs to be optimized as well.

Chapter 7

HIT optimization

7.1 Introduction

HIT solar cells completely made with the PVMD group's equipment were equipped with ITO front and back TCO. The performance of the HIT solar cells with ITO will be evaluated in the next sections.

7.2 Experimental

A passivated n-doped crystalline silicon wafer was used used as substrate for the deposition of 5 nm thick a-Si:H layer, 15 nm p-doped a-SiC:H and a ITO TCO of 240 nm on one side. On the other side of the silicon wafer again a 5 nm a-Si:H thin film was deposited followed by a n-doped a-Si:H layer of 10 nm, 240 nm ITO TCO and an aluminum back contact (Figure 7.1 [A]). A mask was used to create individual solar cells of 1 $\times$ 1 cm^2 during thermal evaporation of the aluminum back contact.

The recipe used for the ITO depositions consisted of the deposition parameters mention in Table 7.1:

Parameter	Unit	Front ITO	Back ITO
Power	Watt	200	250
Pressure	μbar	20	20
Sputtering gas (Ar)	sccm	15	15
T_{heater}	°C	275	275
$T_{substrate}$	°C	150	150
Deposition time	min	30	30
Target-to-substrate	mm	110	110

Table 7.1: HIT ITO deposition parameters

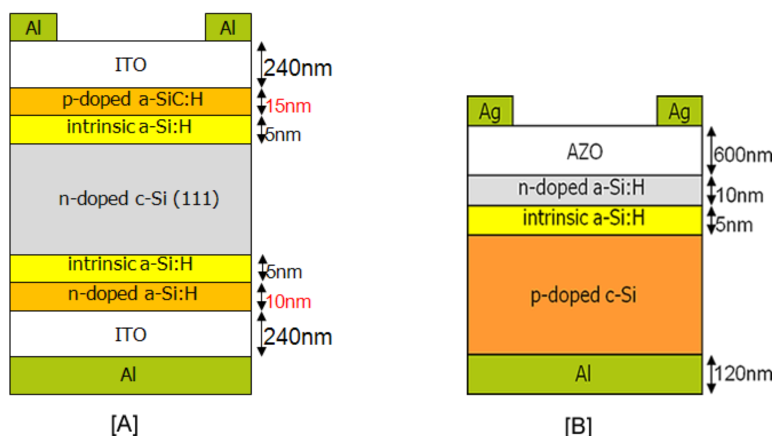

Figure 7.1: Schematic of HIT solar cell with ITO front and back TCO [A] and single junction HIT with AZO front TCO [B]

7.3 Results and discussion

The performance of the HIT deposition run was measured with the illuminated I-V solar simulator, the external parameters are displayed in Table 7.2. Comparison with a similar HIT deposition run with alternative TCO material is not straightforward since only single junction HIT deposition runs with AZO as TCO were available. However, in the table (Table 7.2) below the external parameters of 2 different single junction HIT deposition runs are depicted; one made completely within the PVMD group and one in a combined effort by the Energy Research Center of the Netherlands (ECN) and the PVMD group (see also Figure 7.1 [B]).

Sample	V_{oc} [mVolt]	J_{sc} [mA/m2]	FF [-]	η [%]
HIT ITO	560	322	0.556	10
HIT AZO (PVMD)	564	293	0.17	2.8
HIT AZO (ECN/PVMD)	563	282	0.71	11.4

Table 7.2: HIT ITO and AZO TCO performance

Comparison between the HIT with ITO and the PVMD single junction HIT with AZO TCO shows that the V_{oc} of the PVMD AZO HIT deposition runs is slightly higher. The J_{sc} of the HIT ITO, on the other hand, is quite substantially higher. The FF of the ITO HIT is more than 3 times higher than the PVMD AZO HIT deposition run. The combined external parameters result in a low efficiency for the PVMD AZO HIT deposition run (2.8 %).

The ECN/PVMD HIT deposition run also has a slightly higher V_{oc}, but the J_{sc} is even lower than that of the PVMD HIT deposition run. The

FF of the ECN/PVMD HIT deposition run is however significantly higher than the other two deposition runs, resulting in a higher overall efficiency (11.4%).

It needs to be noted that the standard recipe used resulted in a high percentage of damaged solar cells. It is believed that this is a result of the relative high power density and substrate temperatures during the ITO deposition.

7.4 Conclusions

HIT thin-film solar cells were successfully prepared. Comparison with similar HIT solar cells was not possible, compared to single junction HIT solar cells made within the PVMD group the ITO HIT deposition run performed much better. However, when compared to the single junction HIT solar cell with AZO TCO made by the ECN/PVMD combination the FF and efficiency significantly lower.

The experiments with HIT solar cells equipped with ITO TCOs showed that using the high power and elevated substrate temperature during ITO deposition resulted in damaged solar cells which did not function optimal. It is well known from literature that HIT solar cells require low temperature deposition of the TCOs [25], for optimizing the ITO TCO for HIT solar cells it is therefore advised to deposit at lower temperatures. Moreover, the power density of the Kurt J. Lesker RF magnetron sputtering systems appears to be relatively high when compared to other systems. This could also be one of the reasons for inflicted damage on the amorphous layers of the HIT device. Therefore experiments on low power depositions need to be performed.

Chapter 8

Conclusions

By varying the substrate temperature, RF power, background pressure, oxygen partial pressure and target-to-substrate distance high quality ITO deposition have been achieved. The highest general Figure of Merit achieved was 44.7 $\times 10^{-3}$ $\square/\Omega$ which is amongst the highest values reported in literature. Post-deposition annealing generally increased the optical and electrical parameters, thereby increasing the Φ_{TC} as well.

The Figure of Merit as proposed by Haacke was adjusted to the specific needs of the a-Si:H, μc-Si:H and HIT solar cells made within the PVMD groups facilities. On basis of these adjusted Φ_{TC}s depositions were provided for solar cell fabrication. Both n-i-p and p-i-n a-Si:H solar cells were successfully made. Whereas the averaged external parameters for the solar cells with ITO TCOs were somewhat lower, the individual external parameters for the best solar cells for some of the deposition with ITO showed quite high or even the highest performance. Further optimization, more specifically aimed at the individual solar cells' specifications is however very necessary.

Wet-chemical etching, tested to improve the surface roughness of the ITO, was not successful. The uncontrollable etching did however result in highly etched glass with constant high Haze over the complete wavelength range (300 - 1200 nm). Tilted angle sputtering did not result in inclined growth of ITO. Using amorphous seed layers to facilitate the inclined growth did also not result in a change of growth orientation for the ITO.

Chapter 9

Recommendations

Optimization of ITO TCO should not only focus on the specific wavelength range in which a typical solar cell operate, but also on the physical limitations these solar cells put on the deposition parameters. For the HIT solar cells it is advised to start with a destructive series of experiments which should result in a maximum temperature and power (density) that can be used without damaging the device. After this initial research the optimization process can be repeated.

ITO optimization for μc-Si:H solar cells should focus on the use of the buffer layer (thin AZO) to protect the ITO from the silane plasma whilst at the same time reducing the inevitable loss in conductivity and/or transmittance.

Furthermore it is recommended to optimize the etching process of ITO since the a-Si:H solar cells proved that flat ITO is already competitive. Deposition of ITO on randomly textured substrates is also advised for application in the different types of solar cells.

To improve the ITO deposition uniformity it is recommended to start experiments with the donut-shield installed above the target.

Appendix A

Deposition parameters

		L1172 A	L1173 B	L1174 C	L1175 D	L1176 E
Power	W	300	300	300	300	300
Pressure (Ar)	μbar	20	20	20	20	20
Sputtering gas	sccm	15	15	15	15	15
T_{heater}	**°C**	**0**	**175**	**237**	**275**	**315**
$T_{substrate}$	**°C**	**RT**	**90**	**120**	**150**	**180**
Deposition time	min	10	10	10	10	10
Target-to-substrate	mm	110	110	110	110	110
Deposition rate	nm/min	8.3	9.5	9.6	9.7	9.9

Table A.1: Temperature series deposition parameters

		L1120 A	L1121 B	L1119 C	L1122 D
Power	**W**	**200**	**250**	**300**	**350**
Pressure	μbar	20	20	20	20
Sputtering gas (Ar)	sccm	15	15	15	15
T_{heater}	°C	275	275	275	275
$T_{substrate}$	°C	150	150	150	150
Deposition time	min	30	30	30	30
Target-to-substrate	mm	110	110	110	110
Deposition rate	nm/min	4.1	5.9	8.4	10.4

Table A.2: Power series deposition parameters

		L1132 A	L1133 B	L1134 C	L1136 D	L1119 E
Power	W	300	300	300	300	300
Pressure	**μbar**	**2.6**	**5**	**10**	**15**	**20**
Sputtering gas (Ar)	sccm	15	15	15	15	15
T_{heater}	°C	275	275	275	275	275
$T_{substrate}$	°C	150	150	150	150	150
Deposition time	min	30	30	30	30	30
Target-to-substrate	mm	110	110	110	110	110
Deposition rate	nm/min	12.6	11.1	9.4	8.5	8.4

Table A.3: Pressure series deposition parameters

		L1172 A	L13 B	L14 C	L15 D	L16 E
Power	W	300	300	300	300	300
Pressure	μbar	2.6	5	10	15	20
Sputtering gas (Ar)	**sccm**	**15**	**11.2**	**7.5**	**3.8**	**0**
Sputtering gas (O_2)	**sccm**	**0**	**3.8**	**7.5**	**11.2**	**15**
Oxygen partial pressure	**%**	**0**	**0.25**	**0.5**	**0.75**	**1**
T_{heater}	°C	275	275	275	275	275
$T_{substrate}$	°C	150	150	150	150	150
Deposition time	min	30’00	31’54”	32’37”	32’58”	33’20”
Target-to-substrate	mm	110	110	110	110	110
Deposition rate	nm/min	9.9	9.2	9.1	9	8

Table A.4: Oxygen partial pressure series deposition parameters

		L1181 A	L1182 B	L1183 C	L1180 D	L1184 E	L1185 F
Power	W	300	300	300	300	300	300
Pressure	μbar	10	10	10	10	10	10
Sputtering gas (Ar)	sccm	15	15	15	15	15	15
T_{heater}	°C	275	275	275	275	275	275
$T_{substrate}$	°C	150	150	150	150	150	150
Deposition time	min	30	30	30	30	30	30
Target-to-substrate	**mm**	**165**	**140**	**115**	**110**	**90**	**65**
Deposition rate	nm/min	14.9	12.1	9.8	9.5	7.3	5.5

Table A.5: Target-to-substrate series deposition parameters

		L1173 A	L1174 B	L1172 C	L1175 D	L1176 E
Power	W	300	300	300	300	300
Pressure	μbar	10	10	10	10	10
Sputtering gas (Ar)	sccm	15	15	15	15	15
T_{heater}	°C	275	275	275	275	275
$T_{substrate}$	°C	150	150	150	150	150
Deposition time	**min**	**10**	**20**	**30**	**40**	**50**
Target-to-substrate	mm	110	110	110	110	110
Deposition rate	nm/min	10.2	10.1	9.9	10.2	10.1

Table A.6: Deposition time series deposition parameters

Appendix B

ITO standard recipe

The 'standard' recipe mentioned in the report consisted of the deposition parameters mentioned in the table below:

Parameter	**ITO**	**Unit**
RF power	300	W
p_{depo}	10	ubar
Ar flow	15	sccm
T_{heat}	275	°C
T_{sub}	150	°C
d	110	mm
Ramp up time	6 (30W/min from 150 W)	min
Pre-sputter time	15	min
Heating time	15 min (during pre-sputtering	min
Deposition time	30	min
Ramp down time	6 (80W/3 min)	min
Deposition rate	10.1	nm/min

Table B.1: ITO standard recipe deposition parameters

Bibliography

[1] U. E. I. Administration, “International energy outlook 2010.” http://www.eia.doe.gov, 2010.

[2] S. Shafiee and E. Topal, “When will fossil fuel reserves be diminished?,” *Energy Policy*, vol. 37, no. 1, pp. 181 – 189, 2009.

[3] U. N. I. P. on Climate Change, “Ipcc fourth assessment report.” http://www.ipcc.ch, 2007.

[4] P. Lorenz, D. Pinner, and T. Seitz, “The economics of solar power,” *McKinsey Quarterly*, June 2008.

[5] V. Arkhipov, *Thin Film Solar Cells Fabrication Characterization and Applications*. Wiley, 2007.

[6] Wikipedia, “Solar cell.” http://en.wikipedia.org/, October 2010.

[7] J. Perlin, “The solar cell turns 50.” http://www.nrel.gov/docs/fy04osti/33947.pdf, August 2004.

[8] M. A. Green, K. Emery, Y. Hishikawa, and W. Warta, “Solar cell efficiency tables (version 36),” *Progress in Photovoltaics: Research and Applications*, vol. 18, p. 346352, August 2010.

[9] M. A. Green, “Third generation photovoltaics: solar cells for 2020 and beyond,” *Physica E: Low-dimensional Systems and Nanostructures*, vol. 14, no. 1-2, pp. 65 – 70, 2002.

[10] M. Zeman, *Course material for Solar Cell lectures at Delft University of Technology*. Delft University of Technology, P. O. Box 5053, Delft, 2600 GB, The Netherlands, 2009.

[11] A. Gordijn, *Microcrystalline Silicon for Thin-Film Solar Cells*. PhD thesis, Utrecht University, 2005.

[12] D. Carlson and C. Wronski, “Amorphous silicon solar cell,” *Applied Physics Letters*, vol. 28, pp. 671 – 673, June 1976.

[13] S. Benagli, D. Borrello, E. Vallat-Sauvain, J. Meier, U. Kroll, J. Htzel, J. Bailat, J. Steinhauser, M. Marmelo, G. Monteduro, and L. Castens, eds., *High-Efficiency Amorphous Silicon Devices on LPCVD-ZnO TCO Prepared in Industrial KAI TM-M R&D Reactor*, EU PVSEC, September 2009.

[14] S. Veprek and V. Marecek, "The preparation of thin layers of ge and si by chemical hydrogen plasma transport," *Solid-State Electronics*, vol. 11, no. 7, pp. 683 – 684, 1968.

[15] J. Meier, R. Fluckiger, H. Keppner, and A. Shah, "Complete microcrystalline p-i-n solar cell—crystalline or amorphous cell behavior?," *Applied Physics Letters*, vol. 65, no. 7, pp. 860–862, 1994.

[16] D. L. Staebler and C. R. Wronski, "Reversible conductivity changes in discharge-produced amorphous si," *Applied Physics Letters*, vol. 31, no. 4, pp. 292–294, 1977.

[17] T. Matsuyama, K. Wakisaka, M. Kameda, M. Tanaka, T. Matsuoka, S. Tsuda, S. Nakano, Y. Kishi, and Y. Kuwano, "Preparation of high-quality n-type poly-si films by the solid phase crystallization (spc) method," *Japanese Journal of Applied Physics*, vol. 29, no. Part 1, No. 11, pp. 2327–2331, 1990.

[18] M. Taguchi, A. Terakawa, E. Maruyama, and M. Tanaka, "Obtaining a higher voc in hit cells," *PROGRESS IN PHOTOVOLTAICS: RESEARCH AND APPLICATIONS*, vol. 13, p. 481488, 2005.

[19] K. Baedeker *Ann. Phys. (Leipzig)*, vol. 22, p. 749, 1907.

[20] R. Baetens, B. P. Jelle, and A. Gustavsen, "Properties, requirements and possibilities of smart windows for dynamic daylight and solar energy control in buildings: A state-of-the-art review," *Solar Energy Materials and Solar Cells*, vol. 94, no. 2, pp. 87 – 105, 2010.

[21] H. Mbarek, M. Saadoun, and B. Bessas, "Porous screen printed indium tin oxide (ito) for nox gas sensing," *Physica Status Solidi (c)*, vol. 4, p. 19031907, 2007.

[22] T. Minami, "Present status of transparent conducting oxide thin-film development for indium-tin-oxide (ito) substitutes," *Thin Solid Films*, vol. 516, no. 17, pp. 5822 – 5828, 2008. 5th International Symposium on Transparent Oxide Thin Films for Electronics and Optics.

[23] C. G. Granqvist, "Transparent conductors as solar energy materials: A panoramic review," *Solar Energy Materials and Solar Cells*, vol. 91, no. 17, pp. 1529 – 1598, 2007.

[24] D. Ginley and C. Bright, "Transparent conducting oxides," *MRS Bulletin*, vol. 25, pp. 15 – 19, 2000.

[25] E. Fortunato, D. Ginley, H. Hosono, and D. Paine, "Transparent conducting oxides for photovoltaics," *MRS Bulletin*, vol. 32, pp. 242 – 247, 2007.

[26] J. C. C. Fan and J. B. Goodenough, "X-ray photoemission spectroscopy studies of sn-doped indium-oxide films," *Journal of Applied Physics*, vol. 48, no. 8, pp. 3524–3531, 1977.

[27] N. Nadaud, N. Lequeux, M. Nanot, J. Jov, and T. Roisnel, "Structural studies of tin-doped indium oxide (ito) and in4sn3o12," *Journal of Solid State Chemistry*, vol. 135, no. 1, pp. 140 – 148, 1998.

[28] P. Nath and R. F. Bunshah, "Preparation of in2o3 and tin-doped in2o3 films by a novel activated reactive evaporation technique," *Thin Solid Films*, vol. 69, no. 1, pp. 63 – 68, 1980.

[29] G. Frank and H. Kstlin, "Electrical properties and defect model of tin-doped indium oxide layers," *Applied Physics A*, vol. 27, no. 4, pp. 197–206, 1982.

[30] R. Bel Hadj Tahar, T. Ban, Y. Ohya, and Y. Takahashi, "Tin doped indium oxide thin films: Electrical properties," *Journal of Applied Physics*, vol. 83, pp. 2631 –2645, mar. 1998.

[31] Z. Qiao, *Fabrication and study of ITO thin films prepared by magnetron sputtering*. PhD thesis, Universitt Duisburg-Essen, 2003.

[32] H. Kstlin, R. Jost, and W. Lems, "Optical and electrical properties of doped in2o3 films," *Physica Status Solidi (a)*, vol. 29, pp. 87–93, May 1975.

[33] R. B. H. Tahar, T. Ban, Y. Ohya, and Y. Takahashi, "Tin doped indium oxide thin films: Electrical properties," *Journal of Applied Physics*, vol. 83, no. 5, pp. 2631–2645, 1998.

[34] W.-F. Wu and B.-S. Chiou, "Effect of annealing on electrical and optical properties of rf magnetron sputtered indium tin oxide films," *Applied Surface Science*, vol. 68, no. 4, pp. 497 – 504, 1993.

[35] A. Gupta, P. Gupta, and V. Srivastava, "Annealing effects in indium oxide films prepared by reactive evaporation," *Thin Solid Films*, vol. 123, no. 4, pp. 325 – 331, 1985.

[36] J. R. Bellingham, W. A. Phillips, and C. J. Adkins, "Intrinsic performance limits in transparent conducting oxides," *Journal of Materials Science Letters*, vol. 11, no. 5, pp. 263–265, 1992.

[37] W. Rees, *Physical Principles of Remote Sensing.* Cambridge University Press, 2001.

[38] J. Szczyrbowski, A. Dietrich, and H. Hoffmann, "Optical and electrical properties of rf-sputtered indiumtin oxide films," *Physica Status Solidi (a)*, vol. 78, p. 243252, July 1983.

[39] R. L. Weiher and R. P. Ley, "Optical properties of indium oxide," *Journal of Applied Physics*, vol. 37, pp. 299 –302, jan. 1966.

[40] N. Balasubramanian and A. Subrahmanyam, "Electrical and optical properties of reactively evaporated indium tin oxide (ito) films-dependence on substrate temperature and tin concentration," *J. Phys. D: Appl. Phys.*, vol. 22, p. 206, 1989.

[41] L. Gupta, A. Mansingh, and P. Srivastava, "Band gap narrowing and the band structure of tin-doped indium oxide films," *Thin Solid Films*, vol. 176, no. 1, pp. 33 – 44, 1989.

[42] E. Burstein, "Anomalous optical absorption limit in insb," *Phys. Rev.*, vol. 93, pp. 632–633, Feb 1954.

[43] T. S. Moss, "The interpretation of the properties of indium antimonide," *Proceedings of the Physical Society. Section B*, vol. 67, p. 775, October 1954.

[44] U. G. Survey, "Rare earth elementscritical resources for high technology," tech. rep., U.S. Geological Survey, 2002.

[45] U. G. Survey, "Mineral commodity summaries 2010," tech. rep., U.S. Geological Survey, 2010.

[46] K. Wasa, M. Kitabatake, and H. Adachi, *Thin Film Materials Technology - Sputtering of Compound Materials.* William Andrew Publishing/Noyes, 2004.

[47] I. Hamberg and C. G. Granqvist, "Evaporated sn-doped in[sub 2]o[sub 3] films: Basic optical properties and applications to energy-efficient windows," *Journal of Applied Physics*, vol. 60, no. 11, pp. R123–R160, 1986.

[48] N. Balasubramanian and A. Subrahmanyam, "Effect of substrate temperature on the electrical and optical properties of reactively evaporated indium tin oxide films," *Materials Science and Engineering: B*, vol. 1, no. 3-4, pp. 279 – 281, 1988.

[49] C. Bishop, *Vacuum Deposition onto Webs, Films, and Foils.* William Andrew Publishing, 2007.

[50] J. Mooney, B. Radding, and D. Shirley, "Spray pyrolysis processing," in *Spray pyrolysis processing*, vol. 12, pp. 81–101, 1982. cited By (since 1996) 41.

[51] S. Ashok, P. Sharma, and S. Fonash, "Spray-deposited ito 8212;silicon sis heterojunction solar cells," *Electron Devices, IEEE Transactions on*, vol. 27, pp. 725 – 730, apr. 1980.

[52] H. Haitjema and J. Elich, "Physical properties of pyrolytically sprayed tin-doped indium oxide coatings," *Thin Solid Films*, vol. 205, no. 1, pp. 93 – 100, 1991.

[53] B. Bessais, N. Mliki, and R. Bennaceur, "Technological, structural and morphological aspects of screen-printed ito used in ito/si type structure," *Semiconductor Science and Technology*, vol. 8, no. 1, p. 116, 1993.

[54] W. Grove, "On the electro-chemical polarity of gases," *Philosophical. Transactions of the Royal Society*, vol. 142, p. 87, 1852.

[55] A. Tracton, *Coatings Technology Handbook*. Marcel Dekker, 2005.

[56] K. Wasa and S. Hayakawa, *Handbook of sputter deposition technology*. Noyes publications, 1992.

[57] B. Chapman, *Glow Discharge Processes: Sputtering and Plasma Etching*. Wiley, 1980.

[58] Anderson and Bay, *Sputtering. by Particle Bombardment, Vol. I*. Springer Verlag, 1983.

[59] O. Kappertz, *Atomistic effects in reactive direct current sputter deposition*. PhD thesis, Rheinisch-Westfalischen Technischen Hochschule Aachen, 2003.

[60] McClanahan and Laegreid, *Sputtering by Particle Bombardment, Vol. III*. Springer, 2007.

[61] M. Ohring, *Materials Science of Thin Films*. Elsevier Inc., 2001.

[62] K. Ellmer, "Magnetron sputtering of transparent conductive zinc oxide: Relation between the sputtering parameters and the electronic properties," *Journal of Physics D: Applied Physics*, vol. 33, no. 4, pp. R17–R32, 2000. cited By (since 1996) 166.

[63] J. Robertson and C. Clapp, "Removal of metallic deposits by high-frequency currents," *Nature*, vol. 132, pp. 479–480, 1933.

[64] K. Carl, H. Schmitt, and I. Friedrich, "Optimization of sputtered ito films with respect to the oxygen partial pressure and substrate temperature," *Thin Solid Films*, vol. 295, no. 1-2, pp. 151 – 155, 1997.

[65] F. Penning, "Coating by cathode disintegration," 1939.

[66] J. S. Chapin, "The planar magnetron (sputtering source)," *Research/Development*, vol. 25, p. 37, 1974.

[67] J. A. Thornton, "Magnetron sputtering: basic physics and application to cylindrical magnetrons," *Journal of Vacuum Science and Technology*, vol. 15, no. 2, pp. 171–177, 1978.

[68] J. Sundgren, L. Hultman, G.Hkansson, J.Birch, and I.Petrov, eds., *Formation of defects during ion-assisted growth of thin films from the vapour phase*, vol. 268, Materials Research Society, 1992.

[69] E. Terzini, G. Nobile, S. Loreti, C. Minarini, T. Polichetti, and P. Thilakan, "Influences of sputtering power and substrate temperature on the properties of rf magnetron sputtered indium tin oxide thin films," *Japanese Journal of Applied Physics*, vol. 38, no. Part 1, No. 6A, pp. 3448–3452, 1999.

[70] E. Terzini, P. Thilakan, and C. Minarini, "Properties of ito thin films deposited by rf magnetron sputtering at elevated substrate temperature," *Materials Science and Engineering B*, vol. 77, no. 1, pp. 110 – 114, 2000.

[71] M. P. R. Panicker and W. F. Essinger, "Rf sputtering of yttria on indium tin oxide substrates," *Journal of The Electrochemical Society*, vol. 128, no. 9, pp. 1943–1947, 1981.

[72] V. Korobov, M. Leibovitch, and Y. Shapira, "Indium oxide schottky junctions with inp and gaas," *Journal of Applied Physics*, vol. 74, no. 5, pp. 3251–3256, 1993.

[73] P. K. Song, Y. Shigesato, I. Yasui, C. W. Ow-Yang, and D. C. Paine, "Study on crystallinity of tin-doped indium oxide films deposited by dc magnetron sputtering," *Japanese Journal of Applied Physics*, vol. 37, no. Part 1, No. 4A, pp. 1870–1876, 1998.

[74] L. Meng and M. P. dos Santos, "Properties of indium tin oxide films prepared by rf reactive magnetron sputtering at different substrate temperature," *Thin Solid Films*, vol. 322, no. 1-2, pp. 56 – 62, 1998.

[75] F. El Akkad, M. Marafi, A. Punnoose, and G. Prabu, "Effect of substrate temperature on the structural, electrical and optical properties of ito films prepared by rf magnetron sputtering," *phys. stat. sol. (a)*, vol. 177, no. 2, pp. 445–452, 2000.

[76] T. J. Vink, W. Walrave, J. L. C. Daams, P. C. Baarslag, and J. E. A. M. van den Meerakker, "On the homogeneity of sputter-deposited ito films part i. stress and microstructure," *Thin Solid Films*, vol. 266, no. 2, pp. 145 – 151, 1995.

[77] S. Uthanna, P. Reddy, B. Naidu, and P. J. Reddy, "Physical investigations of dc magnetron sputtered indium tin oxide films," *Vacuum*, vol. 47, no. 1, pp. 91 – 93, 1996.

[78] D. Mergel, D. Buschendorf, S. Eggert, R. Grammes, and B. Samset, "Density and refractive index of tio2 films prepared by reactive evaporation," *Thin Solid Films*, vol. 371, no. 1-2, pp. 218 – 224, 2000.

[79] C. V. R. V. Kumar and A. Mansingh, "Effect of target-substrate distance on the growth and properties of rf-sputtered indium tin oxide films," *Journal of Applied Physics*, vol. 65, no. 3, pp. 1270–1280, 1989.

[80] W.-F. Wu and B.-S. Chiou, "Properties of radio-frequency magnetron sputtered ito films without in-situ substrate heating and post-deposition annealing," *Thin Solid Films*, vol. 247, no. 2, pp. 201 – 207, 1994.

[81] T. Karasawa and Y. Miyata, "Electrical and optical properties of indium tin oxide thin films deposited on unheated substrates by d.c. reactive sputtering," *Thin Solid Films*, vol. 223, no. 1, pp. 135 – 139, 1993.

[82] R. N. Joshi, V. P. Singh, and J. C. McClure, "Characteristics of indium tin oxide films deposited by r.f. magnetron sputtering," *Thin Solid Films*, vol. 257, no. 1, pp. 32 – 35, 1995.

[83] M. Bender, W. Seelig, C. Daube, H. Frankenberger, B. Ocker, and J. Stollenwerk, "Dependence of oxygen flow on optical and electrical properties of dc-magnetron sputtered ito films," *Thin Solid Films*, vol. 326, no. 1-2, pp. 72 – 77, 1998.

[84] C. G. Choi, K. No, W.-J. Lee, H.-G. Kim, S. O. Jung, W. J. Lee, W. S. Kim, S. J. Kim, and C. Yoon, "Effects of oxygen partial pressure on the microstructure and electrical properties of indium tin oxide film prepared by d.c. magnetron sputtering," *Thin Solid Films*, vol. 258, no. 1-2, pp. 274 – 278, 1995.

[85] S. Cho, J. Park, S. Lee, W. Cho, J. Lee, H. Yon, and P. Song, "Effects of o2 addition on microstructure and electrical property for ito films deposited with several kinds of ito targets," *Journal of Physics and Chemistry of Solids*, vol. 69, no. 5-6, pp. 1334 – 1337, 2008. 14th International Symposium on Intercalation Compounds - ISIC 14.

[86] R. H.-J. Franken, *Transparent conducting oxide contacts and textured metal back reflectors for thin film silicon solar cells.* PhD thesis, Utrecht University, 2006.

[87] L.-C. Chen, C.-C. Chen, Y.-T. Sung, and Y.-Y. Hsu, "Oblique-angle sputtering effects on characteristics of nanocolumnar structure anisotropic indium tin oxide films," *Journal of The Electrochemical Society*, vol. 156, no. 6, pp. H471–H474, 2009.

[88] M. M. Hawkeye and M. J. Brett, "Glancing angle deposition: Fabrication, properties, and applications of micro- and nanostructured thin films," *Journal of Vacuum Science & Technology A: Vacuum, Surfaces, and Films*, vol. 25, no. 5, pp. 1317–1335, 2007.

[89] Y. Zhong, Y. Shin, C. Kim, B. Lee, E. Kim, Y. Park, K. Sobahan, C. Hwangbo, Y. Lee, and T. Kima, "Optical and electrical properties of indium tin oxide thin films with tilted and spiral microstructures prepared by oblique angle deposition," *Journal of Materials Research*, vol. 23, pp. 2500 – 2505, 2008.

[90] S. Bensmaine, L. L. Brizoual, O. Elmazria, J. J. Fundenberger, and B. Benyoucef, "Deposition of zno inclined c-axis on silicon and diamond by r.f. magnetron sputtering," *physica status solidi (a)*, vol. 204, p. 30913095, 2007.

[91] F. Moll, "Novel concepts for improved light trapping in thin-film silicon solar cells," Master's thesis, Delft University of Technology, 2009.

[92] T. N. I. of Standards and Technology, "The hall effect." http://www.nist.gov, 2010.

[93] L. J. van der Pauw, "A method of measuring specific resistivity and hall effect discs of arbitrary shape," *Phylips Res. Rep.*, vol. 13, no. 1, 1958.

[94] J. A. Sap, "Modelling optical properties of layers for thin-film silicon solar cells," Master's thesis, Delft University of Technology, 2010.

[95] C. G. Pope, "X-ray diffraction and the bragg equation," *Journal of Chemical Education*, vol. 74, no. 1, p. 129, 1997.

[96] M. G. Hutchins, A. J. Topping, C. Anderson, F. Olive, P. van Nijnatten, P. Polato, A. Roos, and M. Rubin, "Measurement and prediction of angle-dependent optical properties of coated glass products: results of an inter-laboratory comparison of spectral transmittance and reflectance," *Thin Solid Films*, vol. 392, no. 2, pp. 269 – 275, 2001.

[97] prof.dr. J.W.M. Frenken, *Course material for Scanning Probe Microscopy lectures at Leiden University.* Leiden University, 2010.

[98] G. Binnig, C. F. Quate, and C. Gerber, "Atomic force microscope," *Phys. Rev. Lett.*, vol. 56, pp. 930–933, Mar 1986.

[99] D. B. Fraser and H. D. Cook, "Highly conductive, transparent films of sputtered in[sub 2 - x]sn[sub x]o[sub 3 - y]," *Journal of The Electrochemical Society*, vol. 119, no. 10, pp. 1368–1374, 1972.

[100] G. Haacke, "New figure of merit for transparent conductors," *Journal of Applied Physics*, vol. 47, no. 9, pp. 4086–4089, 1976.

[101] J.-H. Lee, "Effects of substrate temperature on electrical and optical properties ito films deposited by r.f. magnetron sputtering," *Journal of Electroceramics*, vol. 23, pp. 554–558, 2009. 10.1007/s10832-008-9539-6.

[102] M. Nisha, S. Anusha, A. Antony, R. Manoj, and M. Jayaraj, "Effect of substrate temperature on the growth of ito thin films," *Applied Surface Science*, vol. 252, no. 5, pp. 1430 – 1435, 2005.

[103] V. Malathy, S. Sivaranjani, V. Vidhya, J. J. P. T. Balasubramanian, C. Sanjeeviraja, and M. Jayachandran, "Amorphous to crystalline transition and optoelectronic properties of nanocrystalline indium tin oxide (ito) films sputtered with high rf power at room temperature," *Journal of Non-Crystalline Solids*, vol. 355, p. 15081516, 2009.

[104] M. Martinez, J. Herrero, and M. Gutierrez, "Optimisation of indium tin oxide thin films for photovoltaic applications," *Thin Solid Films*, vol. 269, pp. 80–84, 1995.

[105] A. M. Gheidari, F. Behafarid, G. Kavei, and M. Kazemzad, "Effect of sputtering pressure and annealing temperature on the properties of indium tin oxide thin films," *Materials Science and Engineering: B*, vol. 136, no. 1, pp. 37 – 40, 2007.

[106] G. Kavei and A. M. Gheidari, "The effects of surface roughness and nanostructure on the properties of indium tin oxide (ito) designated for novel optoelectronic devices fabrication," *Journal of Materials Processing Technology*, vol. 208, p. 514519, 2008.

[107] M. Z. Kana, E. Centurioni, D. Iencinella, and C. Summonte, "Influence of the sputtering system's vacuum level on the properties of indium tin oxide films," *Thin Solid Films*, vol. 500, no. 1-2, pp. 203 – 208, 2006.

[108] A. Nyaiesh, “Target profile change during magnetron sputtering,” *Vacuum*, vol. 36, no. 6, pp. 307 – 309, 1986.

[109] A. Antony, M. Nisha, R. Manoj, and M. K. Jayaraj, “Influence of target to substrate spacing on the properties of ito thin films,” *Applied Surface Science*, vol. 225, no. 1-4, pp. 294 – 301, 2004.

[110] C. Guilln and J. Herrero, “Polycrystalline growth and recrystallization processes in sputtered ito thin films,” *Thin Solid Films*, vol. 510, no. 1-2, pp. 260 – 264, 2006.

[111] R. Das, K. Adhikary, and S. Ray, “The role of oxygen and hydrogen partial pressures on structural and optical properties of ito films deposited by reactive rf-magnetron sputtering,” *Applied Surface Science*, vol. 253, no. 14, pp. 6068 – 6073, 2007.

[112] F. El Akkad, A. Punnoose, and G. Prabu, “Properties of ito films prepared by rf magnetron sputtering,” *Applied Physics A: Materials Science & Processing*, vol. 71, pp. 157–160, 2000. 10.1007/s003390050046.

[113] H.-C. Lee and O. O. Park, “The evolution of the structural, electrical and optical properties in indium-tin-oxide thin film on glass substrate by dc reactive magnetron sputtering,” *Vacuum*, vol. 80, no. 8, pp. 880 – 887, 2006.

[114] Y. Hu, X. Diao, C. Wang, W. Hao, and T. Wang, “Effects of heat treatment on properties of ito films prepared by rf magnetron sputtering,” *Vacuum*, vol. 75, no. 2, pp. 183 – 188, 2004.

[115] S. Bashar, *Study of Indium Tin Oxide (ITO) for Novel Optoelectronic Devices*. PhD thesis, University of London, 1998.

[116] J. E. A. M. van den Meerakker, P. C. Baarslag, W. Walrave, T. J. Vink, and J. L. C. Daams, “On the homogeneity of sputter-deposited ito films part ii. etching behaviour,” *Thin Solid Films*, vol. 266, no. 2, pp. 152 – 156, 1995.

[117] T. Ratcheva and M. Nanova, “Etching of in2o3:sn and in2o3:te thin films in dilute hcl and h3po4,” *Thin Solid Films*, vol. 141, no. 2, pp. L87 – L89, 1986.

[118] B.-S. Chiou and J.-H. Lee, “Etching of r.f. magnetron-sputtered indium tin oxide films,” *Journal of Materials Science: Materials in Electronics*, vol. 7, pp. 241–246, 1996. 10.1007/BF00133122.

[119] W. Wohlmuth and I. Adesida, “Properties of r.f. magnetron sputtered cadmium-tin-oxide and indium-tin-oxide thin films,” *Thin Solid Films*, vol. 479, no. 1-2, pp. 223 – 231, 2005.

List of Figures

1.1 Three generations of solar cells [11] 3
1.2 Schematic representation of atomic structure of single crystal silicon (left) and hydrogenated amorphous silicon (right) [10] 4
1.3 Distribution of density of allowed energy states for single crystal silicon [A] and a-Si:H [B] [10] 5
1.4 General structure of a-Si:H solar cell 6
1.5 Schematic representation of microcrystalline growth mechanism [11] 7
1.6 Schematic structure of superstrate micromorph solar cell [5] . 7
1.7 Structure of HIT solar cell [18] 8
1.8 Spectral power density of sunlight. The different spectra refer to the extraterrestrial AM0 radiation and the AM1.5 radiation 9

2.1 Principle of light scattering due to TCO surface roughness . . 11
2.2 Cationic sites in the cubic In_2O_3 structure [27] 13
2.3 Transmittance and reflection 17
2.4 Assumed parabolic band structure of undoped indium oxide and the effect of tin doping [41] 18
2.5 Abundance (atom fraction) of the chemical elements in Earths upper continental crust as a function of atomic number. Indium is indicated by the red circle, zinc and tin by the blue circles [44]. 19
2.6 Possible phenomena arising from incident ion [57] 22
2.7 Basic principle of sputter deposition. Ions are generated in a plasma and are accelerated towards the target, impinging ions remove material from the target which subsequently condenses at the substrates [59]. 23
2.8 Schematic drawing showing the magnetic field lines [49] . . . 28
2.9 Schematic diagram of oblique-angle sputtering [87]. 31
2.10 ITO deposited at α=80° and resulting β=41° [89] 32

3.1 Schematic of the RF magnetron sputtering system 34
3.2 Schematic of the Hall effect [92] 36

3.3 Sample with contact layout for van der Pauw measurement . 37
3.4 Schematic of MiniRT setup 38
3.5 Schematic of Bragg reflection [95] 40
3.6 Schematic of TIS accessory 41
3.7 Specular transmittance through a stack of layers [94] 42
3.8 AFM setup and operating principle [97, 94] 43
3.9 J-V characteristics of a p-n junction in the dark and under illumination [10] 46

4.1 Temperature series thickness (bins) and deposition rate (symbols) [A], transmittance spectra [B] 49
4.2 Temperature series thickness (bins) and deposition rate (symbols) [A], carrier concentration and mobility [B] 50
4.3 Temperature series Figure of Merit 51
4.4 Power series thickness (bins) and deposition rate (symbols) [A], transmittance spectra [B] 52
4.5 Power series sheet resistance and resistivity [A], carrier concentration and mobility [B] 53
4.6 Power series Figure of Merit 54
4.7 Pressure series thickness (bins) and deposition rate (symbols) [A], transmittance [B] 55
4.8 Pressure series sheet resistance and resistivity [A], carrier concentration and mobility [B] 56
4.9 Pressure series Figure of Merit 57
4.10 Oxygen partial pressure series thickness (bins) and deposition rate (symbols) [A], transmittance [B] 58
4.11 Oxgyen partial pressure series sheet resistance and resistivity [A], carrier concentration and mobility [B] 59
4.12 Oxygen partial pressure Figure of Merit 59
4.13 Target-to-substrate series thickness (bins) and deposition rate (symbols) [A], transmittance [B] 60
4.14 Target-to-subtrate series sheet resistance and resistivity [A], carrier concentration and mobility [B] 61
4.15 Target-to-substrate series Figure of Merit 62
4.16 Top and 3-dimensional view of depositions done at 165 mm [A], 115 mm [B] and 65 mm [C] 63
4.17 Deposition time series thickness and deposition rate [A] and transmittance [B] 64
4.18 Deposition time series X-ray diffraction spectra 65
4.19 Deposition time series sheet resistance and resistivity [A], carrier concentration and mobility [B] 66
4.20 Deposition time series Figure of Merit 66
4.21 ITO repeatability series transmittance 69

4.22 ITO repeatability series average transmittance [A] and sheet resistance [B] 70
4.23 ITO repeatability series Figure of Merit 71
4.24 ITO recovery series transmittance 72
4.25 ITO recovery average transmittance [A] and sheet resistance [B] 72
4.26 Effect of annealing: variation in resistivity [A] and changes in transmittance spectra [B] 74
4.27 XRD patterns of as-deposited and vacuum annealed ITO deposition 75
4.28 Transmittance spectra of the etched glass and the etched glass with 300 nm of ITO [A] and the resulting Haze parameter [B] 77
4.29 As-deposited ITO [A], etched glass with ZnO:Al deposition [B] and etched glass with etched ZnO:Al [C] 77
4.30 Diffraction patterns for standard ITO deposited at 0° and 45° 78
4.31 Diffraction patterns for 200 minutes ITO deposited at 0°, 60° and 80° 79
4.32 Seed layers as-deposited [A] and post-annealed [B] transmittance 80

5.1 Individual solar cells on 3×10 cm^2 glass substrate 84
5.2 a-Si:H p-i-n external parameters 86

7.1 Schematic of HIT solar cell with ITO front and back TCO [A] and single junction HIT with AZO front TCO [B] 93

List of Tables

4.1 ITO standard recipe deposition parameters 67
4.2 ITO repeatability series deposition parameters 68

5.1 a-Si:H p-i-n devices front and back TCO 84
5.2 a-Si:H single junction n-i-p solar cell initial efficiencies of best solar cells 87
5.3 a-Si:H n-i-p solar cell performance 88

6.1 ITO TCO deposition parameters for μc-Si:H deposition run . 91
6.2 μc-Si:H p-i-n solar cell performance 91

7.1 HIT ITO deposition parameters 92
7.2 HIT ITO and AZO TCO performance 93

A.1 Temperature series deposition parameters 97
A.2 Power series deposition parameters 97
A.3 Pressure series deposition parameters 98
A.4 Oxygen partial pressure series deposition parameters 98
A.5 Target-to-substrate series deposition parameters 98
A.6 Deposition time series deposition parameters 99

B.1 ITO standard recipe deposition parameters 100

Nomenclature

Abbreviations

AFM	Atomic Force Microscopy
AM	Air Mass
ARTA	Angular reflectance / transmittance analyzer
AZO	Aluminum-doped zinc xxide
BM	Burstein-Moss
BSF	Back surface field
CVD	Chemical vapor deposition
FTO	Fluorine-doped tin oxide
GZO	Galium-doped zinc oxide
HIT	Heterojunction with Intrinsic Thin Layer
IR	Infrared
ITO	Tin-doped indium oxide
IZO	Indium-doped zinc oxide
LCD	Liquid crystal display
MS	Magnetron sputtering
NIR	Near Infrared
PECVD	Plasma-enhanced chemical vapor deposition
PVD	Physical vapor deposition
PVMD	Photovoltaic Materials and Devices
RF	Radio frequency
RMS	Root mean square
SP	Spray pyrolysis
TC	Transparent conductor
TCO	Transparent Conductive Oxide
TIS	Total Integrating Sphere
UV	Ultra violet
VAS	Variable angle spectroscopy
XRD	X-ray diffraction

Physical constants

Symbol	Description	Value	Units
N	Avogadro's number	6.0221415×10^{23} -	
h	Planck's constant	$6.62606896 \times 10^{-34}$	m s^{-1}
		$4.13566733 \times 10^{-15}$	eV s
q	Elementary charge	$1.602176487 \times 10^{-19}$	C

Symbols

Symbol	Description	Units
$Theta_i$	Angle of incident light	[deg]
$Theta_t$	Angle of transmitted light	[deg]
τ	Average collision time	[s]
E_{bg}	Bandgap energy	[eV]
Δ_g^{BM}	Bandgap widening due to BM shift	[eV]
N	carrier concentration	[-]
Z	Charge of ionized centers	[eV]
$\tilde{n}$	Complex refractive index	[-]
c	Concentration Indium atoms	[m^{-3}]
σ	Conductivity	[Sm^{-1}]
I	Current	[A]
J	Current density	[A/m^2]
J_{mp}	Current density (max. power)	[A/m^2]
V_{dc}	DC voltage	[V]
R	Deposition rate	[nm/min]
n_d	Diffraction order	[-]
R_{diff}	Diffuse reflectance	[-]
T_{diff}	Diffuse transmittance	[-]
I_s	Discharge current	[A]
m_v^{eff}	Effective mass conduction band	[kg]
m_{eff}	Effective mass of electron	[kg]
m^*	Effective mass of electrons	[kg]
m_c^{eff}	Effective mass valence band	[kg]
η	Efficiency	[-]
E_{ion}	Energy of incident ion	[eV]
F_{TC}	Figure of Merit	[$\Box$ / Ω]
Φ_{TC}	Figure of Merit (Haacke)	[$\Box$ / Ω]
FF	Fill Factor	[-]
d	Film thickness	[nm]
t	Film thickness	[cm]
R_H	Hall coefficient	[$m^3A^{-1}s^{-1}$]

V_H	Hall voltage	[V]
η_r	Low-frequency relative permittivity	[F/m]
M_1	Mass number of ion	[-]
M_2	Mass number of target	[-]
t_{max}	Maximum film thickness	[nm]
P_m	Maximum power	[W]
Λ	Mean free path of sputtered atoms	[nm]
μ	Mobility	$[cm^2V^{-1}s^{-1}]$
n_c	Number of collisions	[-]
V_{oc}	Open-circuit voltage	[V]
Q_{o2}	Oxygen partial pressure	[%]
η_0	Permittivity of space	[F/m]
J_{ph}	Photo-generated current density	[A/m^2]
V_p	Plasma potential	[V]
p	pressure	[μbar]
m^*_{vc}	Reduced effective mass	[kg]
R	Reflectance	[-]
ρ	Resistivity	[Ohm cm]
θ	Scattering angle	[-]
γ	Secondary electron emission coefficient	[-]
J_{sc}	Short-circuit current density	[A/m^2]
T_{sub}	Substrate temperature	[°C]
U_s	Surface potential barrier	[V]
T_{heat}	Temperature of substrate heater	[°C]
d_h	Thermalization distance	[nm]
d	Thickness	[nm]
E_{thres}	Threshold energy	[Ev]
R_{tot}	Total reflectance	[-]
T_{tot}	Total transmittance	[-]
T	Transmittance	[-]
V_{mp}	Voltage (max. power)	[V]
λ	Wavelength	[nm]